The Pennsylvania State University

The Graduate School

Department of Energy and Mineral Engineering

METHANE DISTRIBUTION AND VENTILATION OPTIMIZATION FOR A SCALED LONGWALL MINE WITH BLEEDER

A Thesis in

Energy and Mineral Engineering

by

Nathan Gendrue

Submitted in Partial Fulfillment
of the Requirements
for the Degree of

Master of Science

December 2019

The thesis of Nathan Gendrue was reviewed and approved* by the following:

Shimin Liu
Associate Professor of Energy and Mineral Engineering
Thesis Advisor

Sekhar Bhattacharyya
Associate Professor of Mining Engineering
Centennial Career Development Professor

William Groves
Associate Professor of Industrial Health and Safety
Undergraduate Program Chair of Environmental Systems Engineering

Mort Webster
Professor of Energy Engineering
Co-Director Initiative for Sustainable Electric Power Systems
Associate Department Head for Graduate Education

*Signatures are on file in the Graduate School

ABSTRACT

Coal is still one of the most important energy resources in the US. Methane gas related geohazards in underground coal mines, including excessive gas outing, gas outburst, methane concentration over limit, are still one of the major technical challenges for continual safe mining operation. Citations given for methane related issues are filed under Code of Federal Regulation (CFR) Part 75.323. By analyzing the statistics of Mine Safety and Health Administration (MSHA), a total of 587 violations were on record for underground coal mines between 2000 and June 2018 under CFR 75.323. The U.S. requires the use of bleeder systems in underground coal mines, except for rare exceptions, and from the MSHA violation data base it shows consistent violations for excessive methane in the bleeder system. Interestingly, it was noted that the actions taken by mine operators commonly failed to address the gas problem, and in other words, the mine operators may not fully understand the causing factors for excessive methane around the face or bleeder systems. This highlights the need of future study to understand the underlying mechanisms of gas emission and its transport behavior within the mine ventilation system. Therefore, the goal of this study is to define the gas emission behavior and its interaction with the active ventilation system. The outcome of this study can provide a mechanism-based modeling capability to optimize the fan settings to reduce the risk of the excessive gas in the bleeder and ventilation systems. The objective of this study is achieved through a series of experiments and computational fluid dynamic (CFD) modeling program. The experiments were conducted on our scaled physical model at Penn State Ventilation Lab and the collected experimental data were used for the model calibration and validation. A CFD model was then established and validated based on the experimental data. The validated CFD model was then used to analyze the ventilation effectiveness under various ventilation incidents. The headgate and tailgate resistances along with the bleeder fan pressure was altered to create 72 different scenarios both with no stopping leakage and with stopping leakage. The results of the 72 simulations are then discussed with a focus on airflow distribution around the headgate and tailgate splits. The model geometry was then altered to include shields and an AFC along the face. Three modified CFD models were created to understand the effect that face advancement on the ventilation effectiveness. It is shown that as the face advances an open space left by the advancing shields creates room for a streamline of air to flow, thus effectively losing its gas dilution potential along the face. The roof fall incidents were created in the tailgate entry; the multitude of simulations included differing locations and severity of incidents. It is shown that a substantial amount of methane builds up around the T-split and cannot be properly diluted when a roof incident occurs. Finally, curtains were added along the face to determine if they would add any beneficial turbulent mixing to effectively reduce the methane concentration around the T-split in a disaster scenario. It is shown that with the addition of curtains across the longwall face the severity of methane build up around the T-split and the roof incidents are lessened.

TABLE OF CONTENTS

LIST OF FIGURES

LIST OF TABLES

ACKNOWLEDGEMENTS

This thesis was supported by an Alpha Foundation Grant for the improvement of mine safety and health. Grant number AFC719-27 titled "Control of Hazardous Gas Emissions to Longwall Face and Bleeder System: Laboratory Experiments, Modeling and Field Monitoring."

I would like to thank Dr. Shimin Liu for his unwavering support throughout the project. This thesis would not have been possible without the countless hours of time you spent advising me, helping me grow as a researcher, and assisting in the technical writing. Thank you so much!

Special thanks to Dr. Long Fan for his assistance in implementing the CFD program Cradle. Many roadblocks were solved with your assistance. Thanks again!

Lastly, I would like to thank my parents who have consistently encouraged me throughout my academic career.

Chapter 1

Introduction

1.1 Coal mining history and its related disasters

Mining has had a long and integrated history with American society, with the Gold Rush in the 1700's, and the coal boom which fueled the Industrial Revolution. In these early years, the motivation of the mining extractions concentrated on the production for the economic development and the safe mining condition has been historically overlooked. With this came a long history of mine disasters, one of the more prominent early incidents was in December 1907, when mine explosions claimed the lives of 703 miners (McAteer, 2011). Coal mining is known for its technical challenge because coal is soft and gas-containing which can lead to both ground control and explosion mine hazards. The number of coal specific mine explosion disasters peaked in the early 20th century with a gradual decline until the end of the 20th century which is shown in figure 1-1. Significant efforts have been devoted to improving the mine safety conditions through scientific studies led by US Bureau of Mines (USBM) and then US National Institute of Occupational Safety and Health (US-NIOSH). Even though the coal mine safety conditions have been dramatically improved, much improvement could still be done.

Figure 1.1 shows the amount of underground coal mine explosions and the fatalities associated with them from 1839 to 2017. At the beginning of the 20th century, mining disasters skyrocketed to over 3000 deaths, followed by over 80 incidents in 1900-1910. After the creation of safety related agencies such as US Bureau of Mines (USBM) the amount of mine disasters and fatalities began to decrease. Further significant legislations were passed by the US Congress throughout the 20th century leading to a drastic decrease in underground coal mine disasters by the end of the century. However, coal mining is inherently dangerous and while these legislations greatly improved the working conditions and lives of all coal mining disasters like the No. 21 Mine disaster in 1981, Sago Mine Disaster in 2006, and Upper Big Branch in 2010 which continue to haunt the coal mining industry (MSHA).

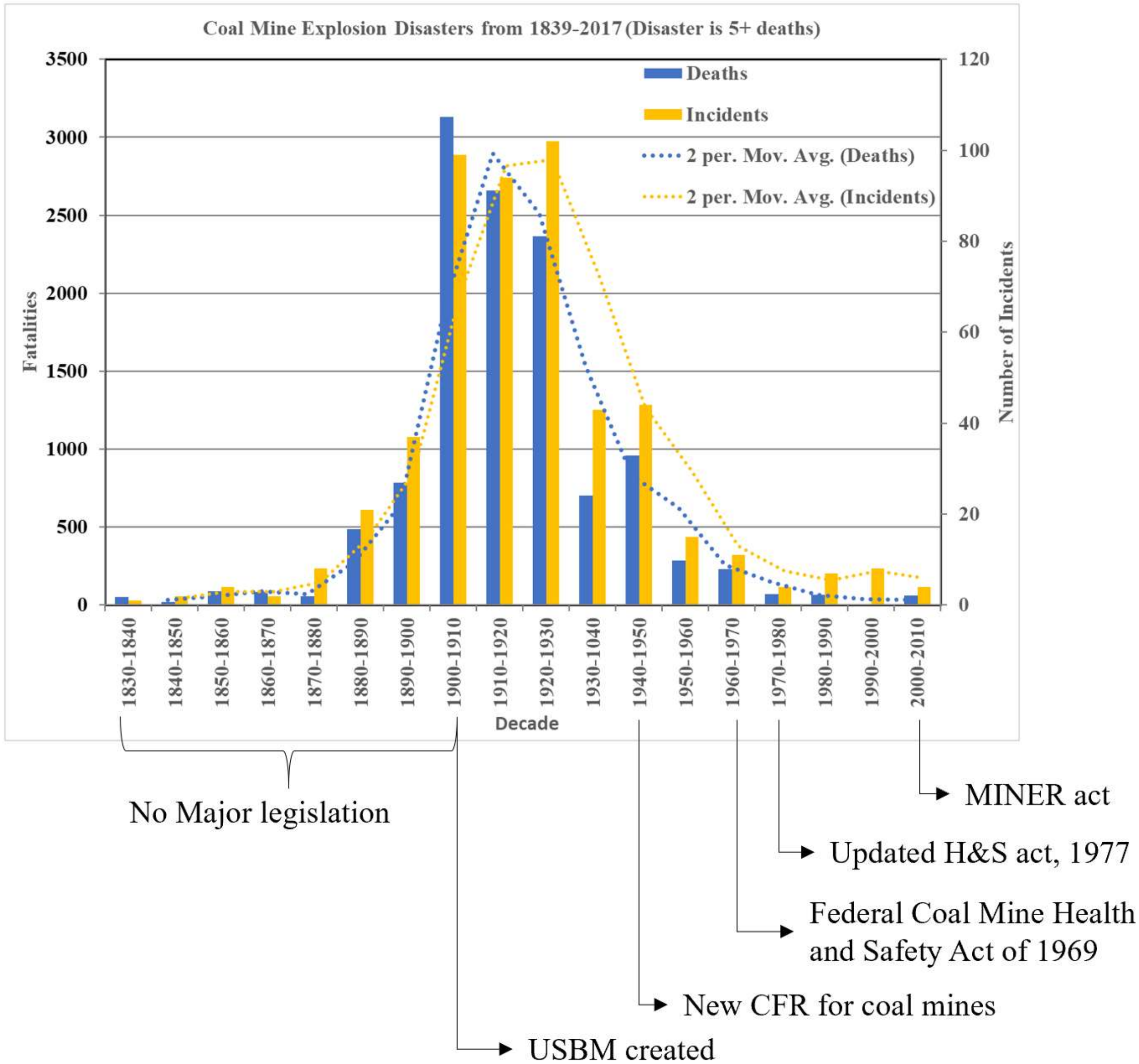

` Figure 1-1: Coal mine explosion disasters by decade from 1839 (disaster is 5+ deaths). Selected major US coal mining legislations included

1.2 Mining methods for coal mining in US

Underground coal mining has a long history in the United States. The Pittsburg coal seam is one of the most mined seams. It is mainly present in Pennsylvania, Ohio, West Virginia, Maryland and others. There are two common underground coal mining methods, namely, room-and-pillar and longwall. The room-and-pillar method is accomplished by a continuous miner (CM). The CM extracts pathways to create rooms and leaves the pillar behind for opening support. The second method, termed as longwall mining, is a rectangular block to be fully extracted by longwall shearer mines (typically called a longwall panel). Each panel starts at one end of the block and moves progressively to the other leaving the current area being mined which is called the active mining face. Hydraulic mechanical supports are used and moved along with the face to create a safe mining environment for machines and personnel. As the panel continuously retreats, the mine overlying strata will sequentially be caved behind the face which is termed as mine gob or goaf. In this thesis, I will use gob to denote the caved region of the coal mine. In the longwall mine, the room-and-pillar method is still required to develop and set up the longwall panels. However, the majority of production comes from the longwall extraction. Figure 1-2 illustrates a typical layout of a longwall panel. In US longwall coal mines, bleeder entries and fans are typically employed to provide the necessary airflow around the face and gob region to dilute methane below non-hazardous levels. Considerations must also be made to minimize the air flow through the gob region for the prevention of spontaneous combustion (SponCom) of SponCom-prone coal seams. Upon the completion of the panel, the mine tends to permanently seal off the panel (now fully a gob region) to isolate the region from the ventilation system. If further action is needed to prevent methane build up, the nitrogen gas can be pumped into the sealed region to displace the air so there is no residual oxygen builds up / accumulates for a potential fire or explosion.

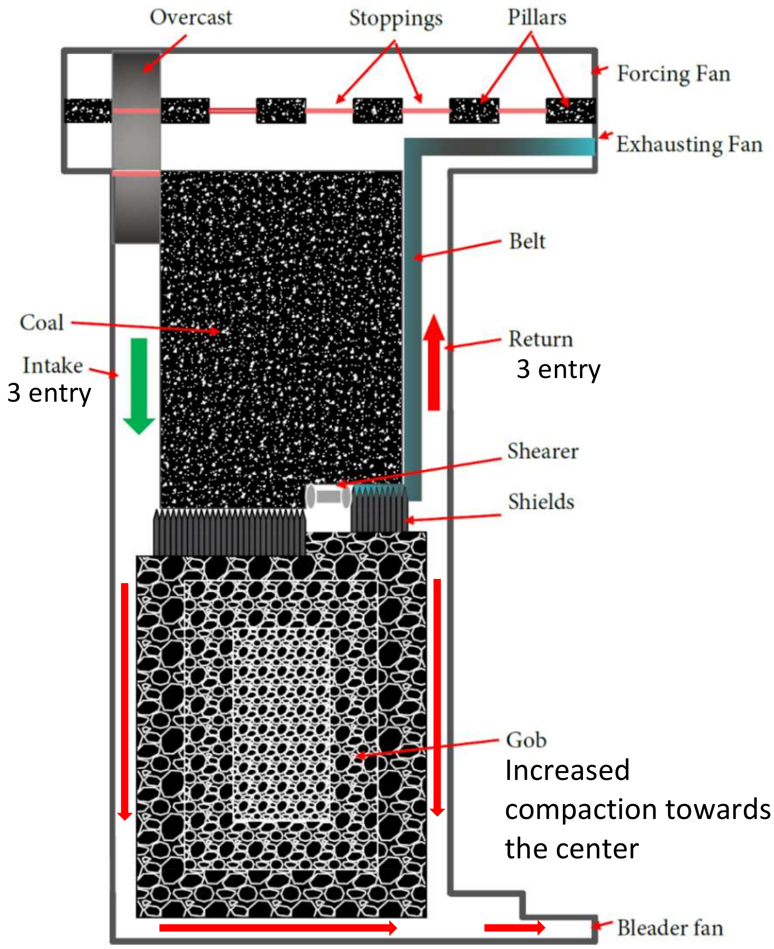

Figure 1-2 Typical longwall panel Layout

1.3 Methane related ventilation importance

Methane was termed as miners' curse, and it is still one of the major safety hazards in underground coal mines. The estimated average methane content in coals for the Central and Northern Appalachian regions are 5.4 to 10.4 (m^3/ton) (C.M. Boyer, 1990). Longwalls were first introduced in the early 20th century and technological improvements allow current longwall mines to produce up to eight to ten thousand tons per working shift. As the production keeps increasing, the methane liberation simultaneously increases which is challenging for the ventilation dilution. Additionally, methane can potentially transport through both overlying and underlying strata towards the caved and compacted gob. Consequently, the gob becomes a gas storage reservoir which may create the over-pressure gob to trigger gas-outing from the gob to the face. This gob-gas-outing is one of top mining hazards in longwall coal mines because it can potentially induce the methane gas over the limit, causing gas outburst at the face or an explosion at the face with ignition.

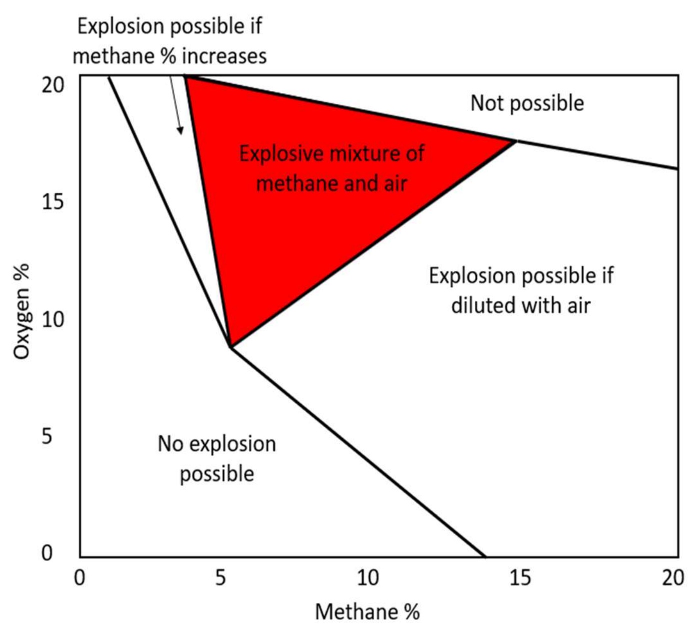

Figure 1-3 Explosive range of methane

Many types of strata gasses can be emitted during coal mining, including methane, nitrogen, carbon dioxide, ethane and other heave hydrocarbon gases. However, methane is of particular interest for underground coal mines because of its abundance and relativity low explosive range. Under normal atmospheric condition, methane becomes explosive when the air mixture contains 5-15% of methane. The explosive range for methane is shown in Figure 1-3. When an explosive air mixture with methane is coupled with an ignition source and adequate oxygen, an explosion is likely (Karacan, 2011). Therefore, the Part 75 in CFR details both excessive methane concentration in the air mixture and when to de-energize the equipment. The current regulation for excessive methane under CFR 30 section 75.323 is when concentrations of methane reaches 1% or beyond, the equipment must be de-energized and corrective action should be made to the ventilation to reduce methane concentrations under 1%. Then further, if the concentration of methane reaches 1.5%, all unnecessary personnel is removed from the area and non-AMS electronic equipment is disconnected at the power source (Code of Federal Regulations, 2014).

1.3.1 Mine gob and ventilation interactions

Much is known about operating a ventilation system by using fundamental equations such as: Bernoulli's equation, Atkinson's equation, and fan laws. In recent years, with the assistance of computational fluid dynamics (CFD), further knowledge is being sought about airflow concentrations, gas and dust, and even porous media such as a longwall gob and its properties. Kurnia et al. (Kurnia, Sasmito, & Mujumdar, 2014) use CFD to study the methane interaction with the ventilation system along an entry/continuous miner face. Furthermore, many researchers study gob properties and issues related to the gob and numerous researches have separately studied ventilation system optimization. There is, however, a noticeable gap of studies with the focus on the interface between the ventilation system along with the bleeder system and the gob. Little is known about how the gob interacts with the ventilation system specifically around the longwall face and tailgate split (T-split). Furthermore, the bleeder fan adds a whole new level of complexity because the bleeder fan can potential change the pressure balance at and around the face and gob. Therefore, the goal of my study is to determine what are the effects of the bleeder fan and the gob on ventilation system and how their settings influence the overall ventilation performance under the various ventilation incidents.

Chapter 2

Background and Literary Review

2.1 Background of the Study

2.1.1 History of Mine Disasters and Subsequent Legislation and Enforcement

The coal mining industry has been plagued with disasters. There have been 376 fatalities in the coal mining industry since 1970 (“Coal Mining Disasters: 1939 to Present,” n.d.). In December 1909, 703 miners lost their lives due to coal mine explosions. This came to be known as “bloody December” and was a factor in the creation of The US Bureau of Mines. Two literatures summarize the history of US legislation relating to the mining industry and the underground coal industry specifically (Brnich and Kowalski-Trakofker, 2010)(Brune and Goertz, 2013). A list of substantial US legislation is listed as follows:

1910 – Law 61-79, established the United States Bureau of Mines (USBM) whose objective was mine safety research and investigation.

1941 – Law 77-49, gave the federal mine inspectors the right to enter and inspect or investigate coal mines annually.

1947 Law 80-326, authorized the creation of a new Code of federal regulations for lignite and bituminous coal; however, there was no mention of enforcement.

1952 – Law 82-552, gave the USBM authority to conduct annual inspections and enforcement authority including the power to issue imminent danger withdrawal orders and violations.

1966 – Law 89-376, enhanced the 1952 act to all coal mines and included repeated unwarrantable failures as a possible withdrawal order. This was also the first mention of a minimum standard for rock dusting (65%) (Brune and Goertz, 2013).

1969 – Law 91-173 (The Federal Coal Mine Health and Safety Act of 1969), was the most comprehensive legislation passed in the US related to the mining industry. Under the new law, two annual inspections were required for surface mines and four for underground mines. It also created many new standards as well as strengthening the existing mine health and safety standards already in place.

1977 – Law 95-164, further strengthened the 1969 act and combined both coal and non-coal mines into one act.

2006 – Mine Improvement and New Emergency Response Act of 2006 (MINER) mainly focused on the post-accident response of the industry, including mandating that emergency plans be made and reviewed every 6 months, 2-way communication and tracking systems be used for miners, availability of mine rescue teams, and caches of SCSR's, along with many other regulations.

2.1.2 Recent Citations Related to Underground Mine Methane in Underground Coal Mines

Citations are no small matter in the mining industry. Fines can be more than $50,000 and having a mine operator associated with a pattern of violation would be devastating. As of June 14, 2018, there were a total of 2,379,364 citations issued by MSHA since 2000, which correlates to approximately 372 daily citations. Specifically, for US underground coal mines, the average number of citations is 2.57 significant and substantial (S&S)/order Violations per 100 inspection hours in 2017. Since underground mines present unique and difficult challenges, they require a different set of rules compared to their surface counterparts. For example, ventilation requirements for gas mitigation, roof support, non-owned or even abandoned wells, and subsidence are just a few areas which can be exclusive to underground mines. Specifically, methane is an area of concern for underground coal mines, Table 2-1 shows the most common methane citations.

Table 2-1 Descriptions of the most common 75.323 citations from Figure 2-2

CFR 30 Part 75.323			Description of the CFR code.
(a)			Tests for methane concentration must be within 12 inches from the roof, face, ribs, and floor.
(b)	(b)(1)		1% or more methane is present in the mine ventilation system.
		(b)(1)(i)	Electrically powered equipment, except for intrinsically safe atmospheric monitoring systems, be deenergized and mechanical equipment be shut off after 1% or more methane is determined in the Ventilation system.
		(b)(1)(ii)	When the ventilation system has 1% or more methane, changes or adjustments to the ventilation system shall be made to reduce the methane concentration to under 1%.
	(b)(2)	(b)(2)(ii)	1.5% or more of methane is present in the working face, or air course except for intrinsically safe equipment all powered equipment shall be disconnected at the power source.
(c)			
(d)			
(e)			The concentration of methane in the bleeder split of air immediately before the air in the split joins another split of air shall not exceed 2%.

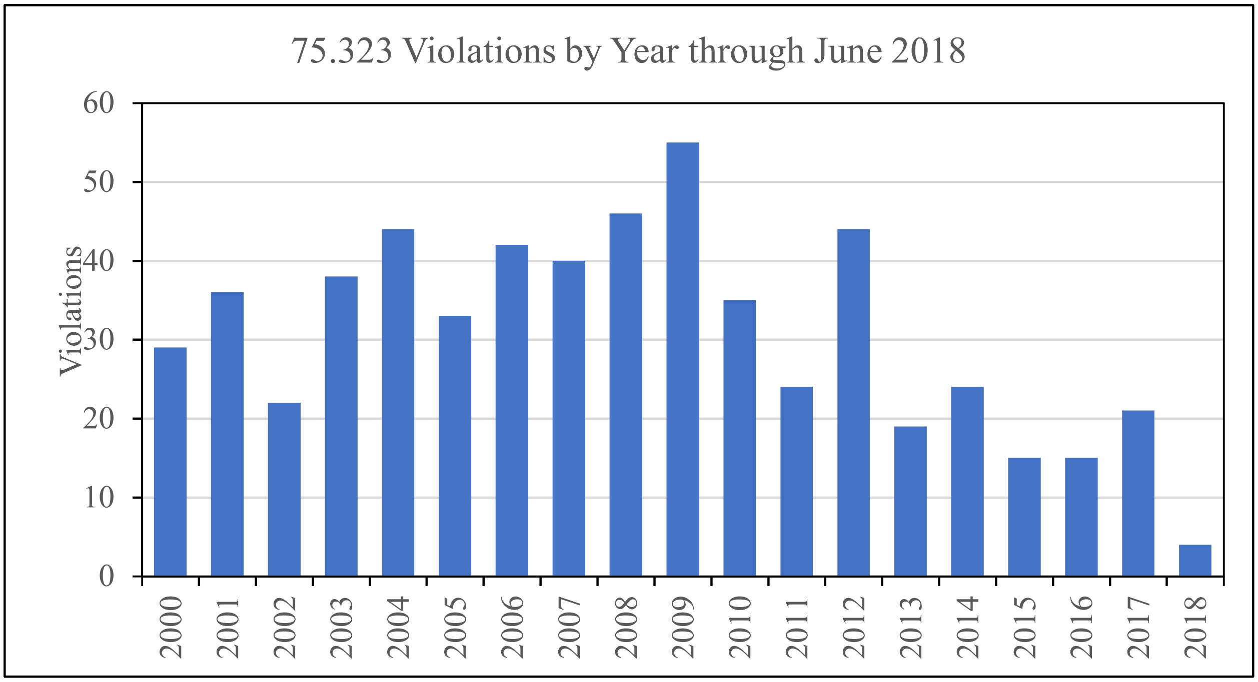

Figure **2-1** Methane related violations (75.323) by year for underground coal mines

Ventilation for underground coal mines is becoming more difficult as production rates and subsequently rate of advances increase the methane related risk potential. Citations given for methane related issues are filed under 75.323. There are around 25 different types of 75.323 violations; however, they all pertain to actions for excessive methane, and/or methane monitoring. For example, the most commonly cited violation for this subset is 75.323(e) which is issued by the inspector when methane in the bleeder system exceed 2%. Between January 2000 and June 2018, a total of 587, 75.323 violations were on record for underground coal mines. Figure 2-1 shows all of the 75.323 violations graphed in a per year basis. Since 2000, there have been 254, 75.323(e) citations which accounts for a little over 43% of all excessive methane citations given, with the next highest cited approximately 13.5%. This second highest citation, 75.323(b)(1)(ii), is for the failure to adjust ventilation controls for the mine excessive methane.

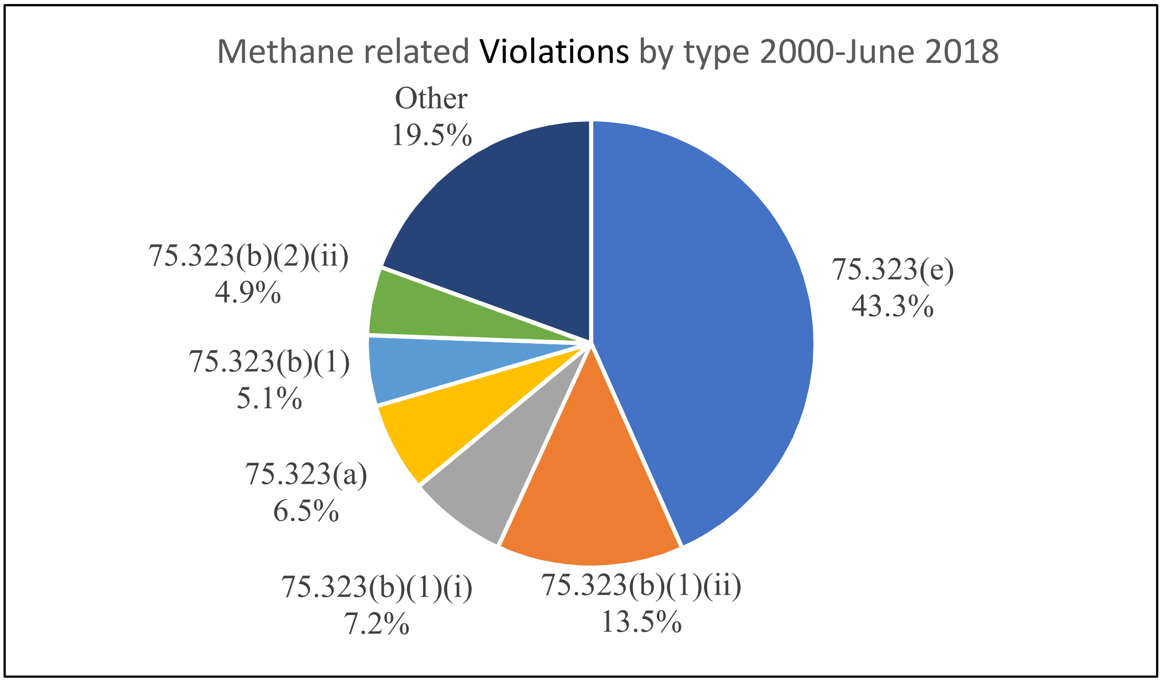

Figure 2-2 Methane related violations by various types, the description of each type can be found in Table 2-1; 75.323(b)(2), 75.323(c), 75.323(b)(1)(iii), 75.323(b), 75.323(c)(2), 75.323(b)(2)(i), 75.323(c)(1) accounts for a total of 16% of the 19.5% in the other category, with numerous other 75.323 types account for the last 3.5%.

Figure 2-2 shows both 75.323(e) and 75.323(b)(1)(ii) account for over 50% of the total methane related citations given throughout the 21st century. No other violation type exceeded 10% which shows a massive need for improvement in the above-mentioned violation types. Particularly concerning is that the highest cited violation is for excessive methane (75.3223(e)), and the second highest is for not altering the ventilation controls for excessive methane (75.323(b)(1)(ii)). These statistics highlight one of the motivations for our research which is to understand the mechanism of excessive methane concentration. There is 43.3% of the violations of excessive methane gas in the mine openings, which would naturally trigger the mine to take the corrective actions to address the excessive methane concentration. However, 13.5% violations remain on not altering the ventilation controls for

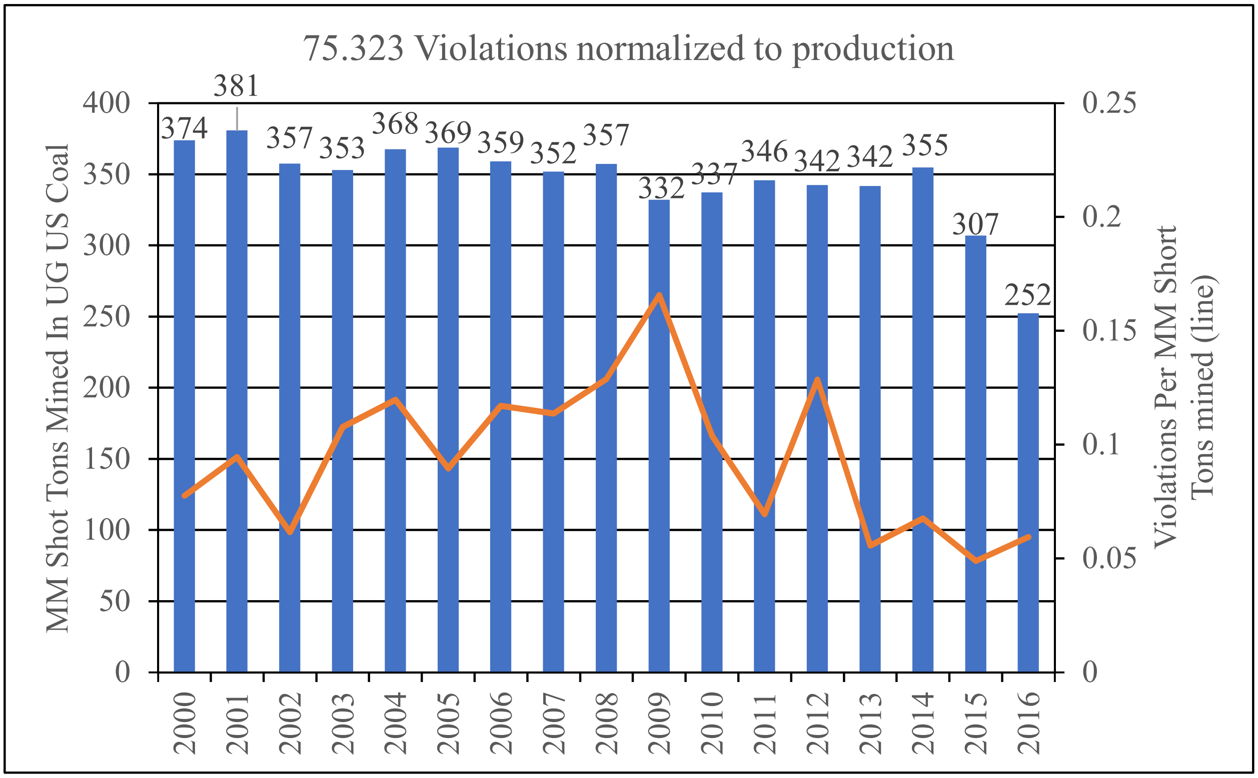

Figure 2-3 Underground coal production and methane related violations per million short tons produced

excess methane. This suggests the actions taken by the operators do not address the gas problem effectively, and in other words, the miner operators may not fully understand the causing factors for excessive methane. In order to make technically sound decisions for the ventilation alteration, the contributing factors and the underlying mechanisms should be fully understood for any ventilation modifications. This is exemplified when considering for about every three citations given for excessive methane, there is one citation given for failing to alter ventilation controls.

Violations should naturally have a close relationship to production rate and the number of operating mines. Figure 2-3 shows the relationship between production and violations. It is interesting to note that there is no clear indication that as production increases so does violations. For example, from 2009 to 2011 production increased by 14 million tons in total while violations per million tons mined had a sharp decrease. Furthermore, in 2003, 2006, 2009, 2012, and 2016, the production decreased from the previous

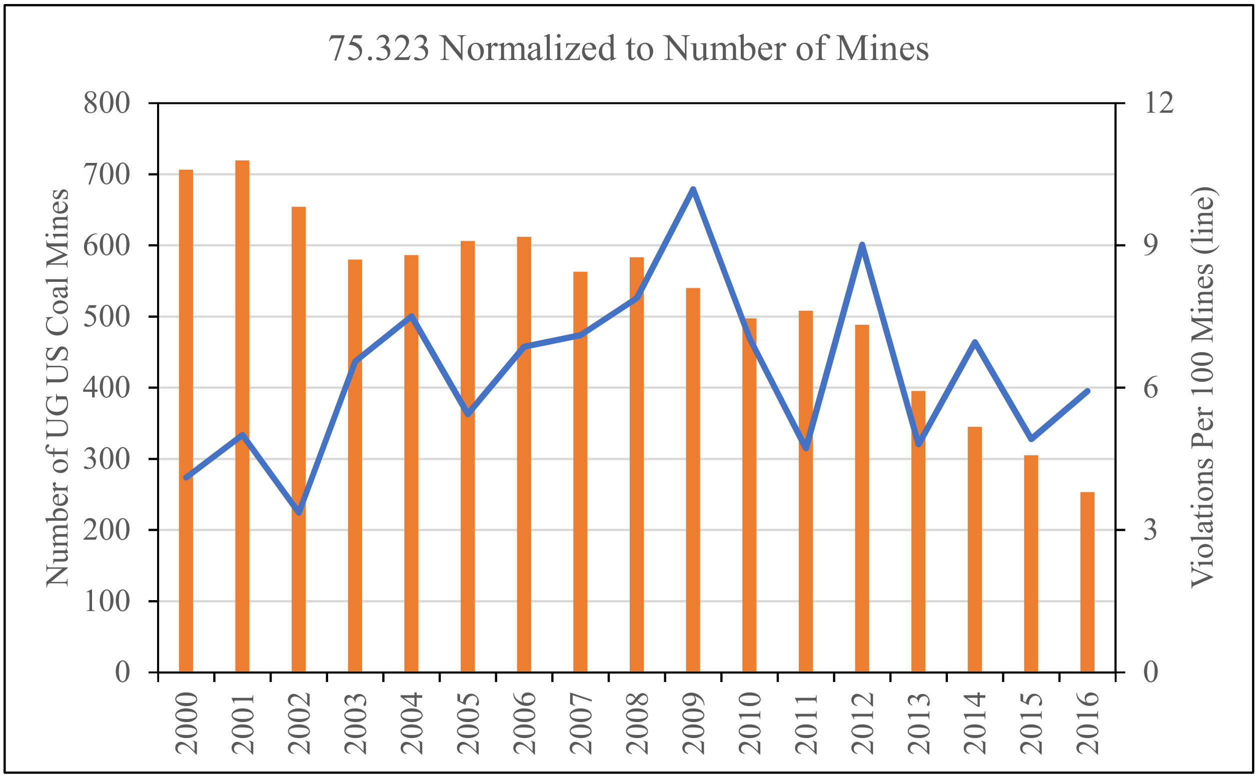

Figure 2-4 Operational Underground Coal mines and methane related violations normalized to operational UG coal mines

year but the violations per million tons mined increased. Thus, coal production does not seem to be the best indicator of 75.323 violations.

Figure 2-4 shows a trend in which violations seem to have little correlation with number of operational mines. Throughout the 21st century, violations per 100 mines has generally increased while the number of mines has gone down over half. Little can be said definitively about the root cause of this trend. However, one such prediction could be that while over half of the underground coal mines have closed, the total coal production from underground coal has only decreased by around one third (~350 MM tons to ~250 MM short tons in Figure 2-3). The remaining operational mines, therefore, must have a higher production in order to create this production. Consequently, this increased strain on the ventilation systems of individual mines, due to the increased production, could be the cause of increased citations.

2.2 Literature review

Ever since mining has gone underground, people have been looking for ways to optimize their ventilation effectiveness. New approaches and theoretical frameworks are used to address ventilation challenges and the engineers tried various best practices based on the improved understanding of the ventilation airflow system. All the attempts have been conducted with the goal of optimizing the system, and with the dynamic nature of mining the network changes before it can be realistically be understood. The advances in computing technology have not had substantial effect on the predictive capabilities of mine ventilation system. Wang et al., (Wang, Ren, Ma, & Zhang, 2018) briefly discussed the use of modern mine ventilation software which is fantastic for determining the overall airflow and pressure distribution in a mine. However, the work did not have the capability to create 2D or 3D profiles that was needed to determine gas and dust distributions. This gap between mine scale network analysis and localized airflow distributions has led researchers to focus on localized phenomena. Throughout this section many studies were reviewed and analyzed. The reviewed studies demonstrate that previous work have been predominantly focused on local phenomena with the belief that a summation of optimized parts makes an optimized system.

2.2.1 CFD application in mine ventilation simulation and optimization

Many researchers have used CFD to understand flow patterns and gas/dust distributions in underground environments. Aziz et al. (AZIZ et al., 1993) were among the first to publish their CFD work, they conducted numerical simulations to investigate dust distributions at a longwall face. Furthermore, Brune et al. (Brune et al., 1999) used advanced computer modeling to assist in understanding airflow distributions by varying 3 parameters: bleeder fan pressure, airflow split at the tailgate corner, and adding an internal bleeder system. They showed that all three parameters could be successfully implemented by CONSOL Energy Ltd. There are a wide range of topics that CFD can assist to improve the understanding and design. However, for the purpose of this study methane distributions, and longwall panel topics was discussed in the following chapters.

2.2.2 Airflow investigations in underground mines

Studies always focus on providing guidance and improving underground mine environment. Field longwall face ventilation study are technically challenging because direct field measurements are typically impossible due to its inaccessibility after caving (Schatzel et al., 2011; Yuan et al., 2006; Yuan and Smith, 2008). Even though the limited access of the direct field measurement, the in-depth studies of the gob and longwall face related to ventilation are still demanded for engineering control of safety and health conditions. This leads to the theoretical studies as a surrogate to understand the ventilation challenges, spontaneous combustion in the gob and the localized airflow patterns in the face and around the shields.

2.2.2.1 Investigations of mine gob gas flow behaviors

Spontaneous combustion is of interest because of its severity for spon-com-prone coals. After the coal is mined, the oxidation process begins in which the coal self-heats. If there is not enough airflow to eliminate the heat from the confined gob and enough oxygen is present to accommodate self-heating, spontaneous combustion becomes a risk to produce hazardous gas CO and heat. Under these conditions the coal can eventually reach thermal runaway at which point a fire can occurs (Yuan and Smith, 2008). Therefore, many CFD studies have been conducted focusing on the gob region with the goal of determining where this region of self-heating coal can happen and determine which method can mitigate the risk. This process involves simulating a gob with a focus on airflow patterns, oxygen, and methane concentration,

Yuan et al. (Yuan et al., 2006) simulated three different longwall panel arrangements in an effort to determine flow patterns and regions where spontaneous combustion can occur within the gob. A U-tube system, U+L system, and a bleeder system were all simulated and they concluded that the U-tube system had a region of possible self-heating almost immediately behind the shields. Results indicated that this region of possible spontaneous combustion was pushed further back into the gob by both the U+L and bleeder system. However, with the addition of a bleeder, a second region of possible self-heating was formed in the rear of the gob. Ren and Balusu (Ren and Balusu, 2005) investigated the effect of panel layout, gob gas holes, and types of gases injected on longwall panels with the goal of minimizing spontaneous combustion hazards throughout the life cycle of a longwall panel. By using field data to calibrate their CFD model, they determined geological factors have little effect on ventilation but have large influence on the gob. Gob gas drainage boreholes were also investigated in their study, with the authors concluding that fluxes in flow rates cause an increased risk in spontaneous combustion hazard. Furthermore, after sealing the panel no major difference are seen between using nitrogen and boiler gas for gas injection and the location of gas injection point has major implications in creating desirable oxygen distributions. Esterhuizen and Karacan (Esterhuizen and Karacan, 2017) conducted a reservoir and CFD simulation to provide guidance on modeling gob permeabilities. The study modeled a fully and partially caved gob as well as a zone of rock fracturing above the collapsed region. Two CFD simulations were conducted to determine the effect that the depth of gob gas boreholes have on gob flow patterns. Their Results indicated that permeability is highest around the shields and that a borehole located in the caved zone results in higher methane production but also has significantly more influence on gob airflows. Yuan and Smith (Yuan and Smith, 2008) simulated a completed gob and an active gob with a bleeder system to determine where spon com hazards occur. Three different types of coal were simulated in the study. Results showed that ventilation conditions and the property of coals strongly effect the spon com hazard. When the rise in temperature was seen, oxygen availability became the driving factor because the original oxygen was consumed in the oxidation of the coal.

2.2.2.2 Face airflow/ventilation controls simulation for underground mines

There are two important issues that can be grouped together dust control and diesel particulate matter (DPM). For coal mines, DPM is not a severer hazard because of limited usage of diesel engines in underground coal mines. The coal dust is a prominent issue and much attention has been made to determine best practices to mitigate airborne dust around the longwall face. There are two main sources of dust at the longwall face: dusts from the shearer and dust generated from the adjustment of shields, and crusher/transfer from armored face conveyor (AFC) (Cai et al., 2018). Furthermore, metal and nonmetal mines are concerned with DPM because miners spend their shifts next to or inside of diesel vehicles. Both respirable dust and DPM have been proven harmful to humans and are kept under strict standards 1.5 mg/m^3 for respirable coal dust (Code of Federal Regulations, 2018) and 160_{TC} $\mu g/m^3$ for DPM (Code of Federal Regulations, 2018). In this section, general ventilation efficiency and airflow patterns around headings, entries, and faces were discussed and reviewed.

Cai et al. conducted a CFD simulation of a longwall face with shields, shearer, and a 10-meter gob region (Cai et al., 2018). They showed that high dust concentrations can be seen in front of the shearer and within 10 meters of the advancing shields. They showed these areas can be out of compliance with MSHA's dust standards and mitigation steps are necessary. Zhang et al. (Zhang et al., 2018) studied the effect of air velocity has on dust concentration for a longwall section. The study concluded that increasing the air velocity has a positive effect on dust control because of the increased turbulence and this effect decreases as velocity increases. Wang et al. (Wang et al., 2018) studied the effect of shearer position and cutting direction have on ventilation flow patterns along a longwall face. A U-tube ventilation scheme was simulated complete with a small gob (10 meters behind the shields). These simulations were validated with filed data and results suggested that shearer position has a large effect on localized flow distribution but little influence on overall flow patterns. Furthermore, cutting against the airflow (tailgate to headgate) created a smaller disturbance in airflow patterns then cutting with the airflow (headgate to tailgate). Lu et al. (Lu et al., 2017) simulated both methane and dust in a continuous miner heading with a focus on determining the best auxiliary vent system. Results indicated that more airflow positively impacted dust and methane concentrations, while individually brattice cloth and blowing exhaust systems were not sufficient and the brattice cloth with a blowing exhaust system preformed the best when compared to all nine cases.

Zheng et al. (Zheng et al., 2015) simulated the effect of a load haul dump (LHD) and a haul truck orientation on DPM distribution in a mine roadway. Their results indicated that because of the temperature differential between the exhaust and mine air DPM migrated towards the roof and extended up and down stream. Assimilation with mine air occurs at different times depending on vehicle orientation. Cheng et al. (Chang et al., 2019) preformed three CFD simulations to determine the effect of duct length on DPM distributions. The models show that DPM follows airflow very closely and that high concentrations of DPM correlate with vortexes in the airflow. The study recommends that the vent duct be placed closest to the face to minimize the vortex effect around the entry. Zheng et al. (Zheng et al., 2017) simulates a LDH and a moving truck inside a roadway. Results show that LHD operators are constantly overexposed to DPM while haul truck drivers may be overexposed depending on their direction of travel. This study provided airflow and DPM distributions but had no mention of mitigative techniques that could be used in terms of ventilation controls.

2.2.3 Methane distribution simulation in underground mines

As previously mentioned, methane is a substantial problem for underground coal operators. If methane concentrations reach between 5-15%, a mine explosion is possible with a proper ignition source (Mishra et al., 2016). Therefore, many studies focus on dilution on methane around the face, both for longwall and CM entry driving. Initial studies focused on the how well CFD can predict patterns with the addition of methane gas. Wala et al. (Wala et al., 2007) compared CFD simulation results to a full scaled model of a continuous miner entry with a curtain. Their studies showed positive agreement between measured velocity and methane data and the predicted values in both Shear-Stress Transport and Spalart-Allmaras turbulence models. Toraño et al. (Toraño et al., 2009) simulated methane and airflow distributions in a roadway and used field measurements to validate their CFD model. They found that methane accumulated around the roof and face of the roadway, then methane concentrations decreased further from the face, followed by an increase in concentrating. The effect of methane injection points was studied by

Kurnia et al. (Kurnia et al., 2014), in which they conducted a series of CFD simulations to determine the effect of methane source quantity, and location have on methane dispersion inside a mine tunnel. They further investigated the use of rectangular ducts with flow directors instead of circular ducts for auxiliary ventilation; concluding that if oriented properly, the directing of airflow to locations with high methane accumulation reduces overall methane concentration, and focusing the airflow at a point is more effective than dispersing it to several points. Over time, researchers justified, through successful implementation of CFD studies, that CFD is a valid predictive tool for airflow distribution and research was started to conduct more predictive and optimization related work.

Wang et al. (Wang et al., 2017a) systematically calculated the methane emission rate for the ribs and longwall face using over and underlying strata. Introducing different methane emission rates across the face depending on the time since the face has been exposed. They conduct six simulations in a U-tube ventilation scheme to determine the effect of shearer position and cutting direction have on methane distribution around the working face and gob area. Then, Wang et al. (Wang et al., 2017b), altered the parameters to determine their influence on the system. A multitude of variables were adjusted: methane emission rate, in seam gas content, adjacent gas bearing strata, U+L ventilation scheme, and dust sprays were all simulated in regards to methane concentration around the face. Wang et al. (Wang et al., 2017b) concludes that methane emission rate has a large impact on methane distributions around the face, but methane gas from adjacent strata has the most effect on the tailgate corners methane distributions. Furthermore, as they determined that an open cross cut in the tailgate, which effectively changing the U-tube system to a U+L system, significantly dilutes the methane accumulation in the tailgate corner. Also, the addition of drum sprays greatly increases the local turbulence seen around the shearer, which decreases methane concentration locally and downstream. Sasmito et el. (Sasmito et al., 2013) used CFD to compare which stopping arrangements in a room and pillar mine dilute methane the best while minimizing pressure loss. Furthermore, six different auxiliary ventilation controls were simulated for a cross cut geometry. Forcing and exhausting systems were investigated with and without brattice cloth and compared for methane concentration, airflow patterns. Energy requirements for each of the six scenarios were also discussed, ultimately concluding that an exhausting system with brattice cloth is the most cost-effective ventilation arrangement. Finally, left and right cuts were investigated for methane flow patterns, with cutting nearest to the intake air first providing the best methane concentration reduction. Mishra et al. (Mishra et al., 2016) used CFD to confirm the recommendation concluded by Bakke and Leach (Bakke and Leach, 1962) that a layering number greater than five is desirable for the dispersion of methane. In conjunction with filed measurements, they simulated six different air velocities to determine its effect on methane layering in the tailgate corner of the longwall panel. It was concluded that velocity is a key driver in methane dispersion and the length and thickness of the methane layer decreases with increases in velocity. Overall a 3 m/s air velocity was enough to keep methane concentration under 1%; this correlates to a layering number above five which collaborates the recommendation made by Bakke and Leach (Bakke and Leach, 1962). Tanguturi et al., (Tanguturi et al., 2017) simulated a six km longwall panel with four different face location, 0.5, 1, 3, and 6 km. The longwall panel geometry was identical to site conditions i.e. the panel was undulating from start to finish. However, this provided a fascinating insight on how flow through the gob occurs. Results showed that oxygen egress is highest when methane emission is lowest; also, the authors concluded that ventilation airflow and controls have a significant impact on gas concentrations up to 250 meters behind the face. However, after 250 meters, buoyancy and gob variables such as: inclinations/geometry, type of overlying strata, and permeability play a much bigger role in determining airflow patterns.

Finally, Tanguturi and Balusu (Tanguturi and Balusu, 2014) used CFD to investigate methane flow patterns in and around the gob. They determined that the tailgate corner area of the face/gob presents a problem in terms of methane concentrations and presented three ways to mitigate the problem. By simulating gob drainage, back return ventilation, and adding a curtain to the face they showed, in all three methods, methane concentration in the tailgate corner of the gob was reduced. Two figures are shown from their paper, Figure 2-6 show the methane concentration in the gob while altering the gob drainage quantity, and Figure 2-7 shows the methane concentration in the tailgate region of the gob both with and without a curtain along the face. This study was the only study found that was created with the intention of discussing

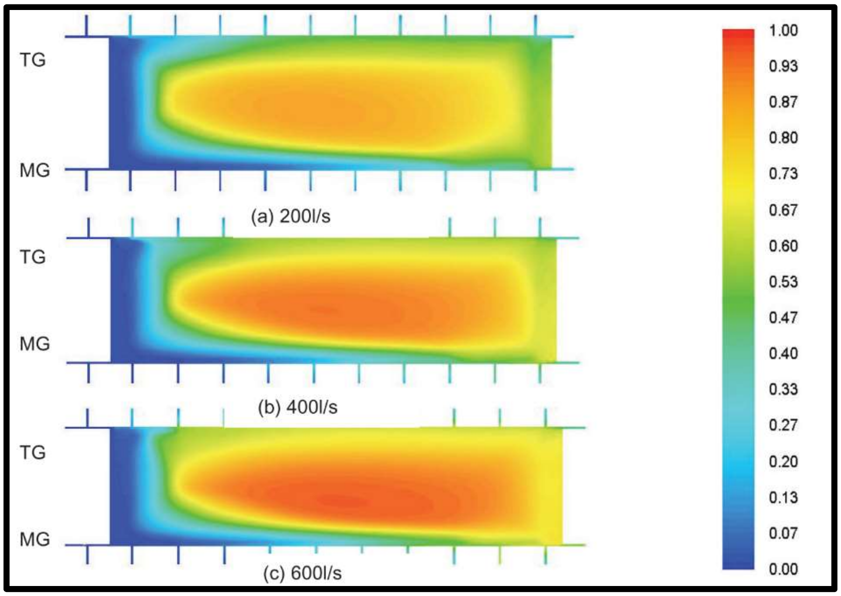

Figure 2-6 CFD simulation of gob with different drainage levels figure taken from K. Tanguturi & Balusu, 2014

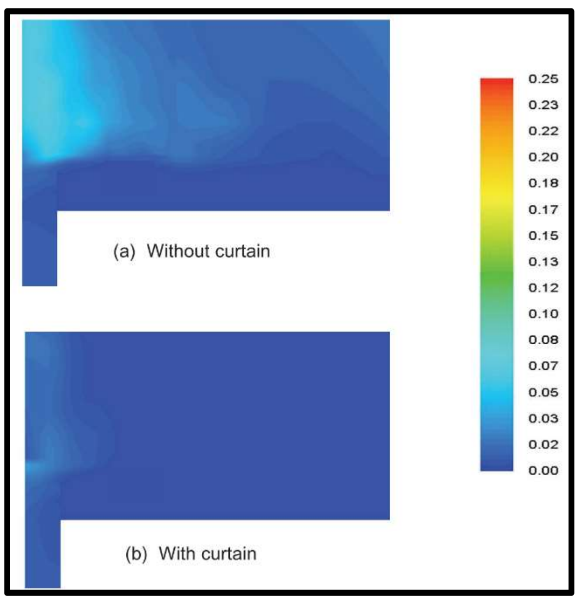

Figure 2-7 CFD simulation of tailgate corner methane concentrations with and without curtain figure taken from K. Tanguturi & Balusu, 2014

methane accumulation around the tailgate region of the gob; many papers discuss this region as a problem are but only indicating/reporting as a side observation.

2.2.4 CFD Turbulence model selection and their application conditions

There are three major classifications of CFD turbulence including direct numerical simulations (DNS), large eddy simulation (LES) and Reynolds Averaged Navier-Stokes equations (RANS). DNS and LES provides the most level of detail and simulation accuracy. However, the miniscule cell sizes required to predict flow patterns make the computational requirements unattainable by modern personal computers (Wang et al., 2018). RANS equations are widely used in engineering applications and generally viewed as an accurate tool. Therefore, understanding RANS equations can be paramount in creating an accurate flow field using turbulent models in CFD. The following reviews provide a summary of two comprehensive studies (Chen, 1995; Zhai et al., 2007).

Major types of RANS models are shown below in Table 2.2. All turbulence models aim to show how turbulent energy and eddies form and dissipate. However, they all provide different levels of complexity and accuracy. There are zero, one, two, and multi eddy viscosity models (EVS) models. The zero equation models assume a constant turbulent viscosity number, and the single equation model uses variables such as turbulent kinetic energy to calculate the eddy viscosity. This, then, adds one equation to the list of transport equations. Two equation models have been the most popular throughout the 20th and 21st centuries. Although there are many forms of two equation models, K-w, k- ε, k-W, k-kl, the k- ε model has been the most widely used. While these models are similar to the one equation model, they resolve an extra equation for eddy viscosity instead of using predefined parameters like in the single equation model. Finally, the multi-equation models consider varying levels of details such as the wall boundary layer effect on turbulence.

Another type of RANS equation is the Reynolds Stress Models (RSM). Previous studies have found RSM to be better suited for recirculating or swirling air patterns. Many view RSM as generally superior to other RANS models (Zhai et al., 2007). However, since swirling patterns, such as a turbine or cyclone, are not expected in a mine simulation model, RSM will not be considered for this current study.

A number of researchers have studied the effect of turbulence models in the context of mining applications; Toraño et al. (Toraño et al., 2009) simulated the same geometry using four different turbulence models: Spallart Almaras, k-omega, k-epsilon, and SST. Findings indicated that all models fit experimental data well, but the k-epsilon model preformed the best. Furthermore, Sasmito et al. (Sasmito et al., 2013) conducted a test of: Spallart Almaras, k-epsilon, k-omega, and RSM models and concluded that Spallart Allmaras was preferable to the others because of the lower computational time and relative error under 15%. Kurnia et al. (Kurnia et al., 2014) conducted tests to determine which turbulence model to use in their study of auxiliary ventilation. They tested the same models as Sasmito et al. (Sasmito et al., 2013) and concluded that k- ε gives reasonably good agreement with experimental data and provides fast computational time.

There are only a few cases in which research in mining used a turbulence model different from k-ε (Sasmito et al., 2013; Wala et al., 2007). The k- ε turbulence model was developed originally by Launder and Spalding (Launder and Spalding, 1974); and since then, it has been widely adopted in engineering applications because of its high accuracy and low computational time. The k- ε model has also been widely used by mining researchers (Cai et al., 2018; Kurnia et al., 2014; Lu et al., 2017; Mishra et al., 2016; Ren and Balusu, 2005; Sasmito et al., 2013; Tanguturi et al., 2017; Tanguturi and Balusu, 2014; Wang et al., 2018; Xu et al., 2015; Yuan et al., 2006). Since there is a large agreement in the literature that signifies the k- ε model is accurate, it was selected as the turbulence model used in this study. The two k-epsilon equations that are added to the general transport equations are shown in appendix A.

Table 2.2 List of RANS turbulence models, figure adjusted from Zhai et. el 2007

RANS												
EVM											RSM	
0 equation	2 equation								Multiple equation			
zero equation	standard k-ε	RNG k-ε	realizable k- ε	LRN-LS	LRN-JL	LRN-LB	LRN K-w	SST K-w	v2f-Dav	V2f-lau	RSM-IP	RSM-EASM

Chapter 3

Experimental Work and Numerical Modeling

Penn State Mine Ventilation Lab (PSU-MVL) is equipped with the physical-scale mine ventilation model designed by Dr. Shimin Liu. The first step of my work is to create a three-dimensional (3D) computer model of the physical geometry using AutoCAD. This CAD model was then used through the entire modeling of my project. This geometric model is used throughout my project and the geometry was slightly altered for specific sections which was described as needed when I tried to introduce the ventilation interruptions. The various CAD models were then imported into the CFD program, Cradle software packages. Cradle package is selected because of its availability and its ability to quickly and accurately perform both computational and post-processing work. The project consists of two main phases illustrated in Figure 3-1, experimental work for the lab data collection for calibration and validation of the CFD model and investigations of gob gas emission and its interaction with the ventilation system through validated CFD models.

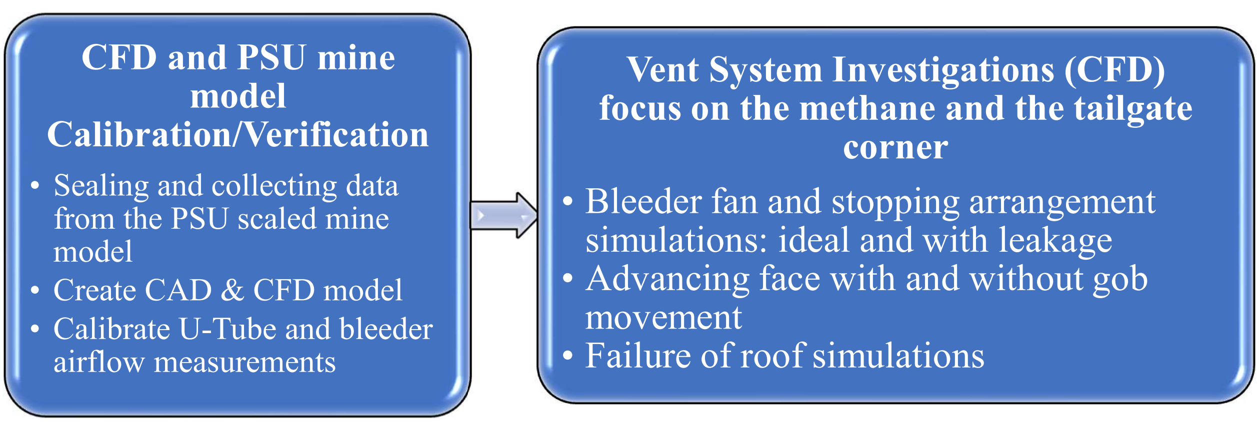

Figure 3-1 Overview of the project

3.1 Scaled Model Validation and CFD Calibration

3.1.1 Introduction to the PSU scaled model

A 1/100th physical scaled model of a typical longwall mine was designed and manufactured in the PSU ventilation lab. The model is fabricated by acrylic sheets for mimicking mine roof and floor and by PVC rectangular tubing for pillars. The acrylic sheets were then sealed using double sided sealing tape and the seams were later sealed with a hot glue gun. The model consists of a 'main' section, a continuous miner section, a longwall section, and a ventilation bleeder section. There is a five entry 'main' that measures a total of 3.2 meters in length, followed by a three entry headgate in the longwall sections. Three of the five entries of the main are designated as intake entries and an overcast (same dimensions as the entries) connects the intake and headgate. The dimensions of each entry are 5 cm in width by 4 cm in height. The overcasts as well as the main section can be seen in Figure 3-2.

The longwall face itself has the dimensions of 1 m of panel width, 8 cm by 4 cm at the working face. There are three ventilation monitoring locations across the face. There is a gob section immediately behind the longwall face which measures around 1.2 m in depth by about 0.8 m in length. Most importantly, the gob can be packed with glass beads which can be arranged in specific patterns to obtain designed precise porosities. The gob section has 41 ventilation monitoring locations at which gas samples can be taken and analyzed. These locations are evenly spaced out across the gob. The tailgate and bleeder system are also three entries, and the bleeder continues from the headgate around the gob to the bleeder fan. The longwall section and bleeder section can be seen in Figures 3-3 & 3-4**Error! Reference source not found.**. There is multiple ventilation monitoring locations in the bleeder system as well as the headgate and tailgate as illustrated in Figure 3-3. There are permanent and adjustable stoppings which are made to ensure they can fully or partially block the airflow as desired. The continuous miner section can be fully blocked off with these adjustable stoppings and for the duration of this study the CM section will be blocked off. However, some of the CM section can still be seen in the left side of Figure 3-3. Foam plugs are used to seal off all ventilation monitoring locations when they are not in use for sampling and monitoring , they are the green dots along the entryways in Figure. 3-2

Three fans are installed with the whole model with the fan locations being in the: intake entry for a forcing ventilation system, return for an exhausting ventilation system, and one exhausting fan in the bleeder system. The fans are attached to a variable frequency drive that ranges from high to low power settings; with the forcing fan on high setting the longwall face can obtain an airflow of 1.2 m^3/min.

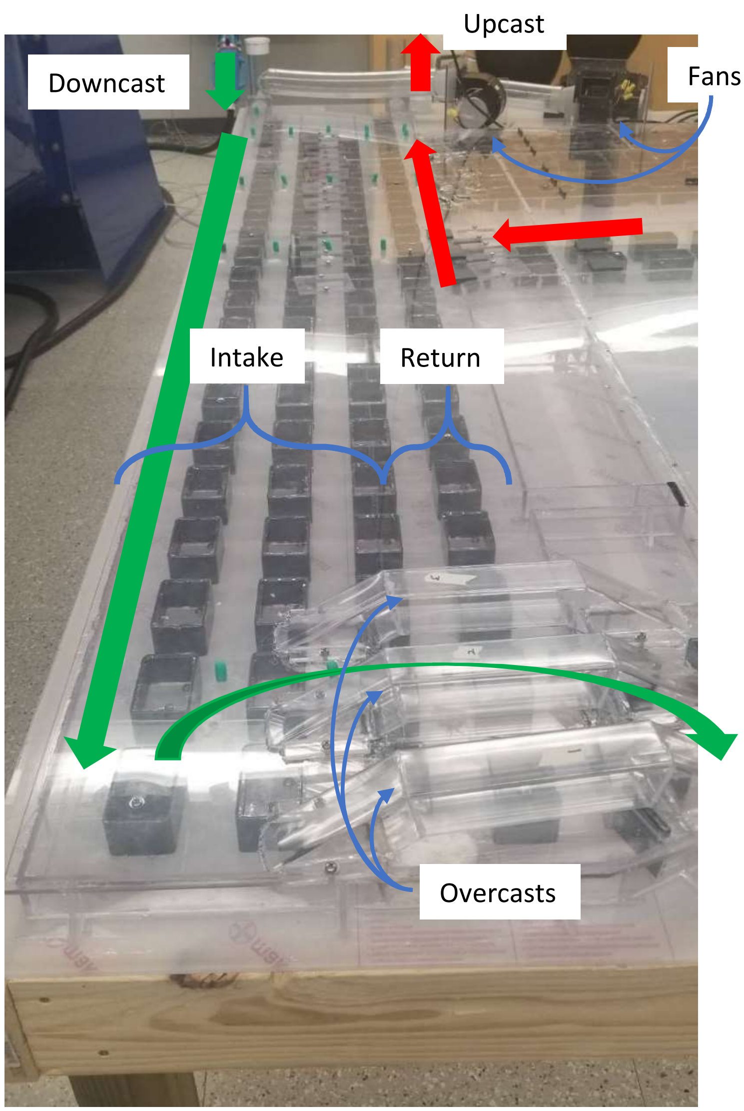

Figure 3-2 Picture of the mains and overcasts in the PSU mine mode

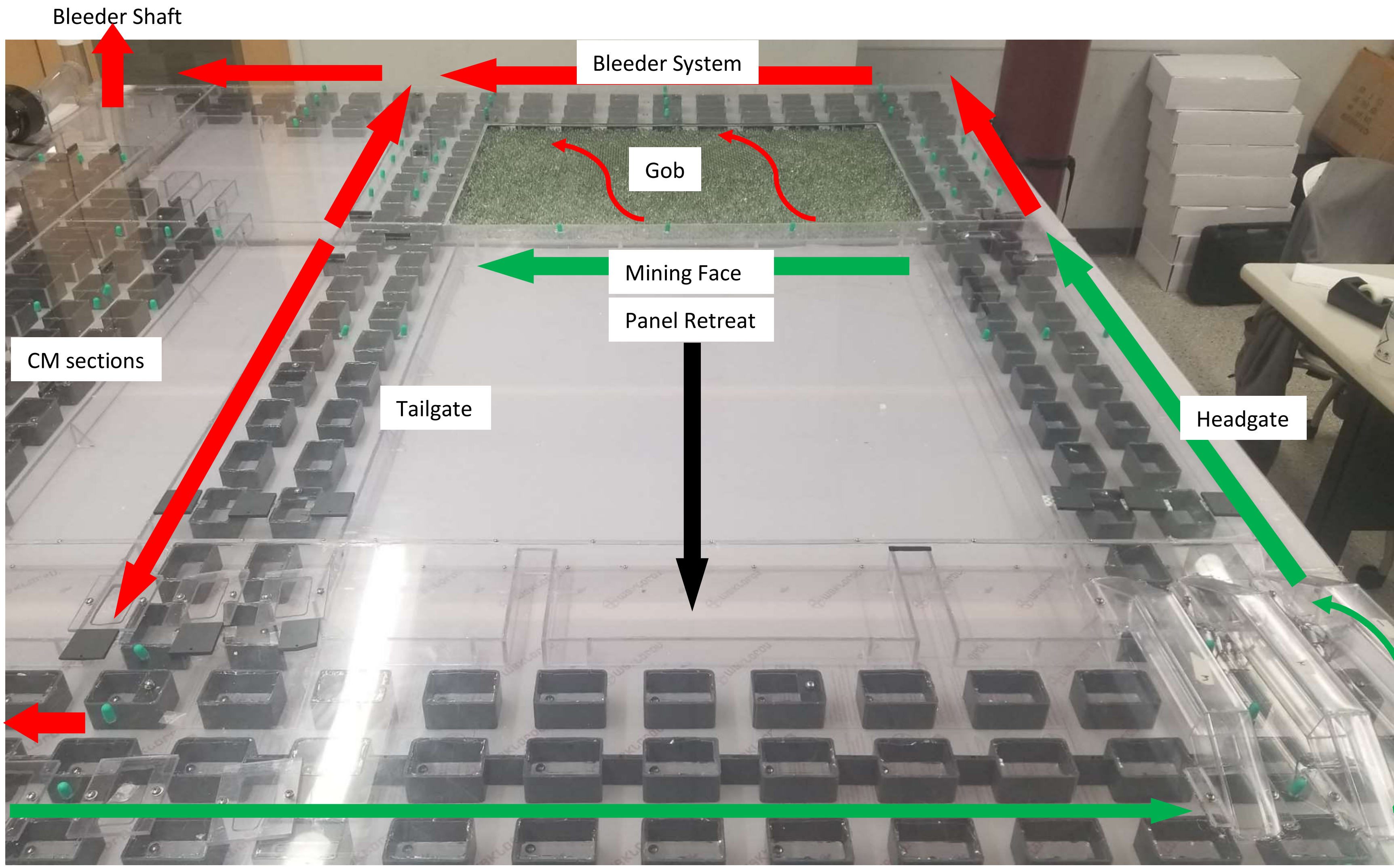

Figure 3-3 Picture of the longwall section in the PSU mine model

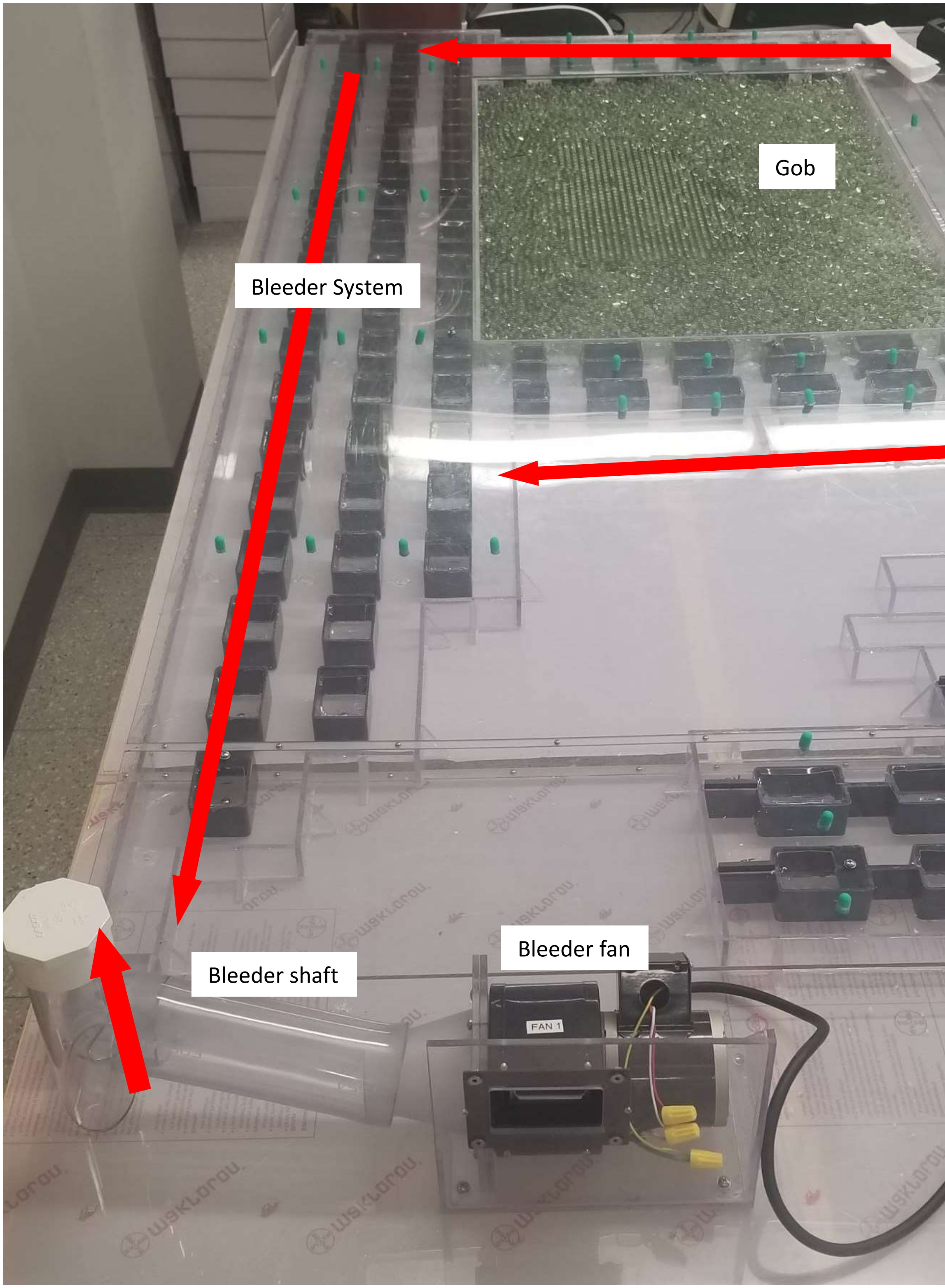

Figure 3-4 Picture of the bleeder system in the PSU mine model

3.1.2 Sealing of physical scaled model

At the beginning, the PSU mine ventilation model was checked for leakage and the boundary conditions for the CFD model must be obtained. One important assumption that CFD uses is that the model geometry is a closed system, i.e. there is no air leakage. Under this assumption, all fluids entering the system should exhaust at designated ports and mathematically it should meet $\sum Flow_{in} = \sum Flow_{out}$. This is a valid assumption for the subsurface mine ventilation system which is a closed airflow system. To have a calibrated CFD model, it is extremely important to have zero leakage from the physical mine model. Furthermore, to ensure accurate pressure gradients leakage from entry to entry should be minimized (leakage across parallel pillars).

Hot-wire anemometers were used for velocity measurements in the PSU mine model. Eight anemometers were simultaneously used in conjunction with computers to measure air velocity at designated monitoring locations. Each anemometer has an operating range of 0.1 m/s to 25 m/s for velocity with a resolution of 0.01 m/s; the accuracy of the anemometer is ± 5% m/s of the measured value. They were purchased from PCE America Inc. specifically model PCE – 423 were used, and Figure 3-5 shows one anemometer as an example. For accurate velocity readings the anemometers must be aligned parallel to the air velocity being measured. For comparison, the velocity measurement was consistently measured at the center of each entry or face. Each velocity measurement was a point measurement. This method was chosen after preliminary tests showed little measurable differences in velocity readings from varying the vertical location of the measuring point. The anemometer placement in the entry is shown in Figure 3-6.

Figure 3-5 Picture of a hot wire anemometer that was used in model validation

To quantify the leakage in the PSU ventilation physical model, velocity measurements were taken from seven locations across a U-tube ventilation scheme. This means the gob and bleeder system completely sealed off, the forcing fan also set on the highest setting. The goal was to determine how to best seal the scaled model. Positions 1-7 in Figure 3-7 were used as velocity measurements positions. The model were sealed with clear double-sided mounting tape, hot glue, and packaging tape as needed. This continued until the measured intake and return airflow are within 10%. Since each measurement has an inherent 5% error, 10% of the total value was considered an acceptable error for the measurement.

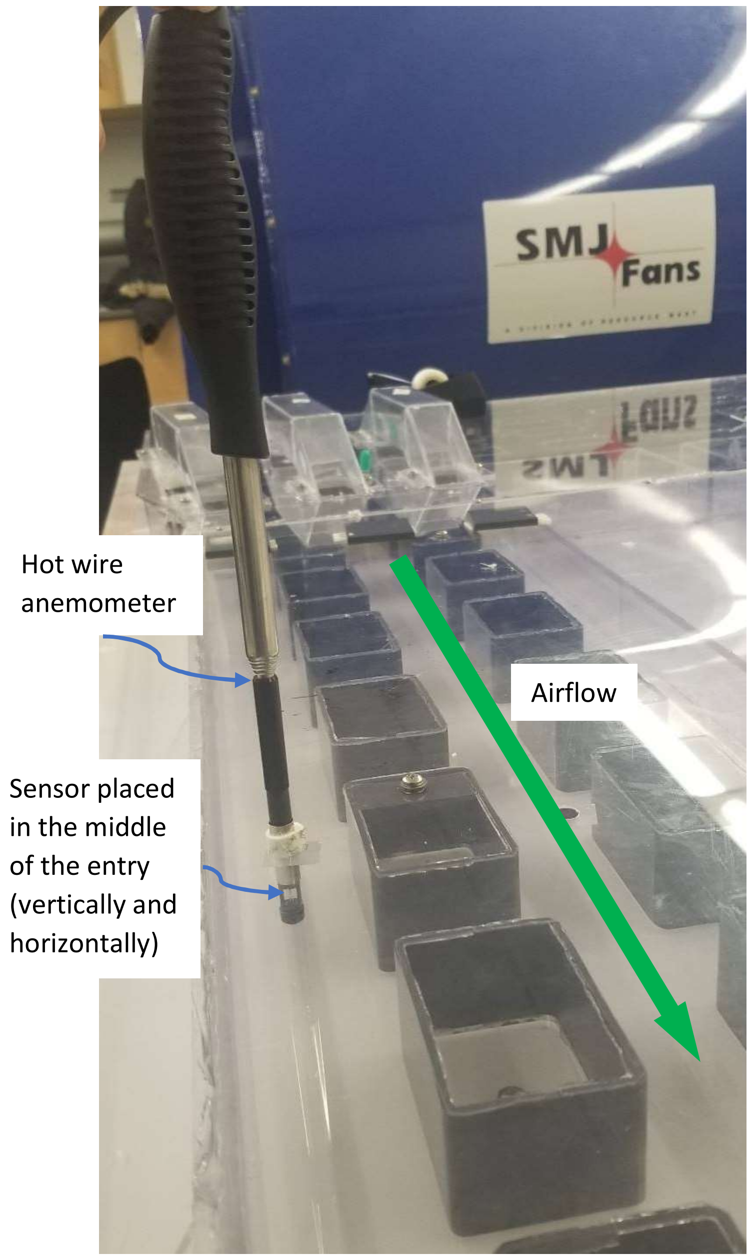

Figure 3-6 Hot wire anemometer set up from position 3 in figure 3-7

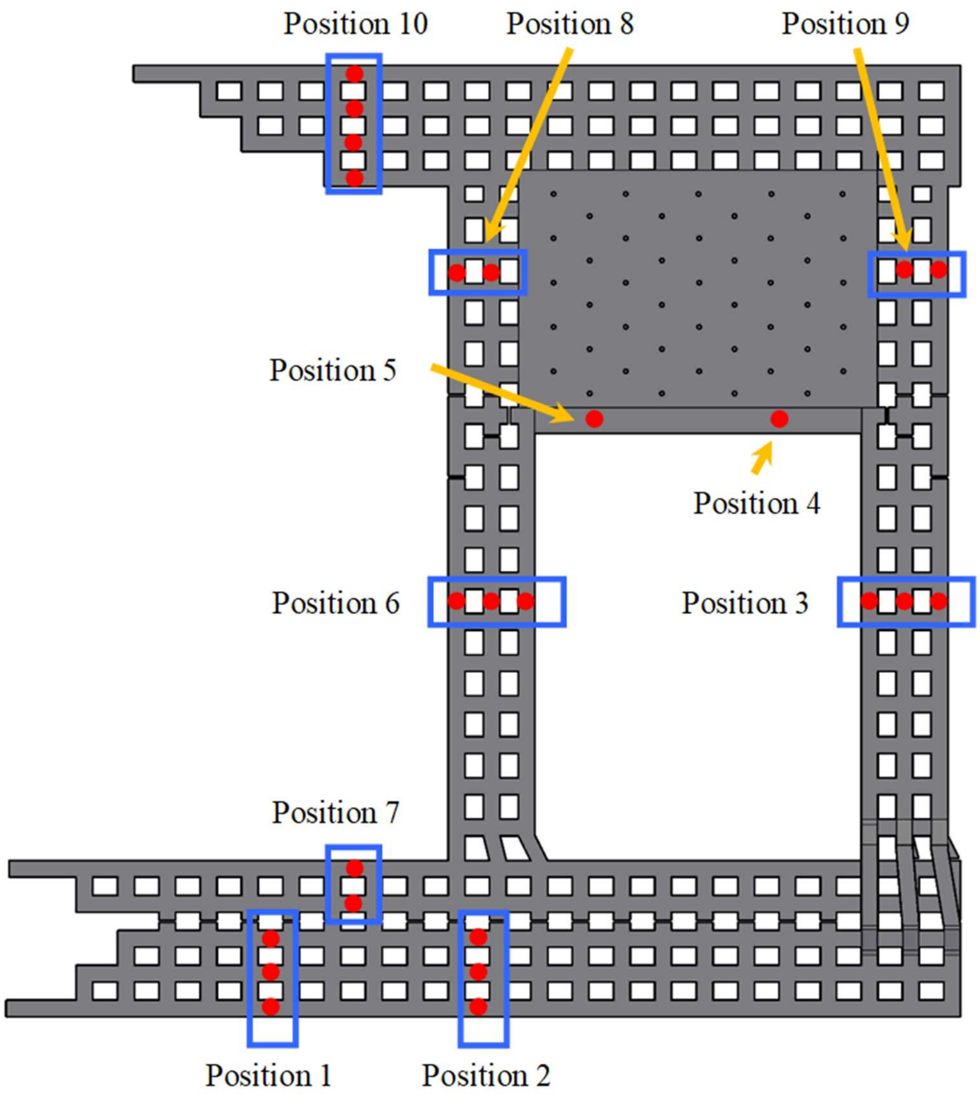

Figure 3-7 Velocity measurement locations in PSU mine model

3.1.3 CFD modeling and mesh independence study

For CFD modeling, a mesh independence study was conducted to determine the optimal cell size that can be used throughout all the simulations. Because geometries in studies vary in size, there is not a uniform accepted standard cell size. However, the common practice among researchers is to perform a mesh independence study, which concludes the chosen mesh size does not influence the simulation results significantly. 5 simulations were conducted with cell sizes varying from 2 cm, 1 cm, 0.5 cm, 0.25 cm, and 0.125 cm. Each simulation was conducted with the same initial and boundary conditions shown in Table 3-1. Only pure air (no gas mixture) was considered in these simulations for simplicity and because the velocity profiles were the only variable of interest. 8 points were investigated across the cross section of the face, this was shown as A-A' in Figure 3-8, velocities at each point was the simulated outputs and all the data were plotted to determine the optimized cell size. Figures 3-8 showing the headgate corner of the face was provided to demonstrate the velocity measurement locations. All the results were presented in Chapter 4 section 4.1.2

Table 3-1 Initial and boundary conditions for the mesh independence study

Inlet (Pressure inlet)	350 pa, 21.5°C, 100% air
Return (Pressure outlet)	0 pa, 21.5°C, 100% air
Bleeder (Pressure outlet)	-140 pa, 21.5°C, 100% air
Walls	Rough surface, ER=0.0043m
Gob porosities	0.10, 0.12, 0.13, 0.15
Temperature (initial condition)	21.5°C
Pressure (initial condition)	101,025 pa

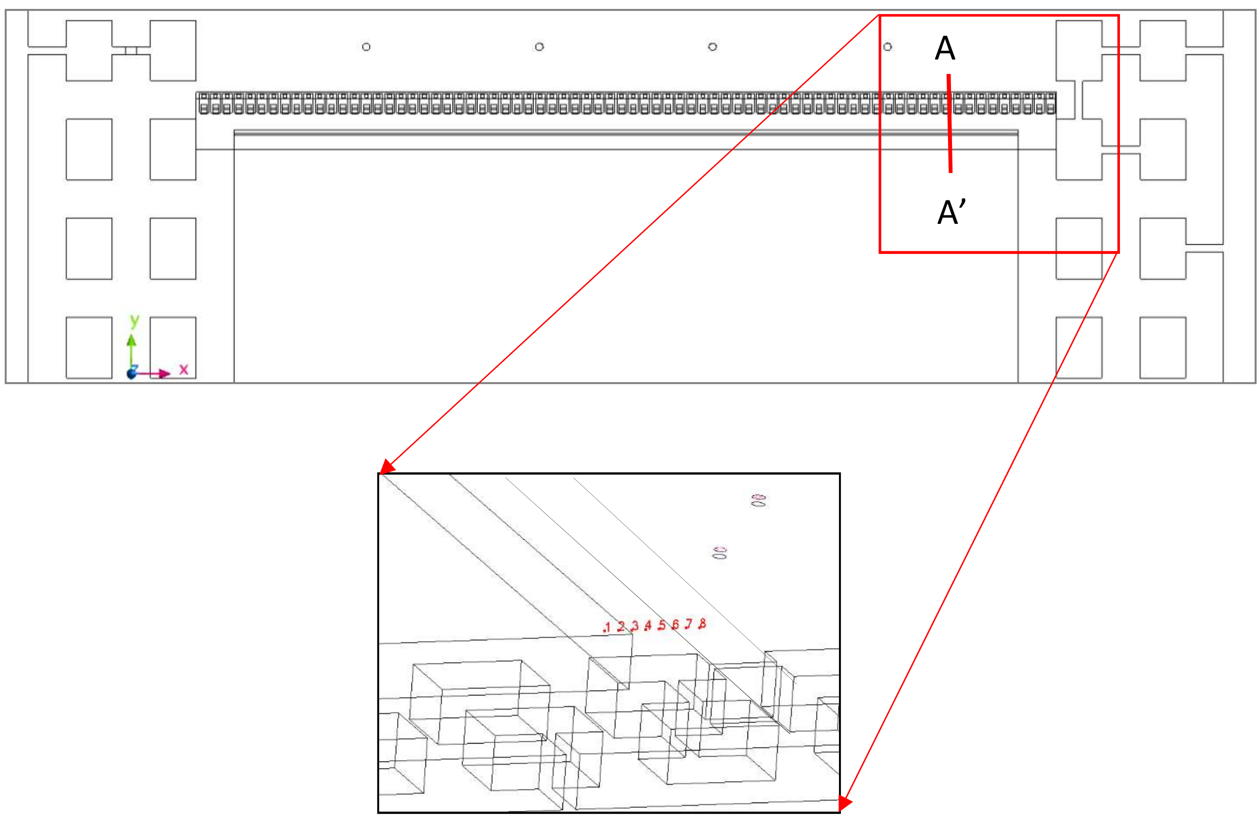

Figure 3-8 Location of velocity reference points for mesh independence study

3.1.4 Validation of CFD model with experimental results

Since the velocity measurements for U-tube ventilation scheme have already been collected after the physical model was properly sealed. CFD modeled velocity results can be compared and validated against the experimental data. Each entry's velocity at the seven locations was compared to the same point in the CFD modeled results. Since the pressure in the scaled model was too low to measure with the current instrumentation guesses will be made as to what inlet pressure to use. subsequently, the guess and check method will be used to align the velocities in the CFD simulation with the measured scaled model velocities. Adjustments to the boundary conditions until the CFD values align with the PSU scaled model measurements. Boundary conditions consist of: wall roughness, total or static pressures, volumetric inflow rates, and outflow rates (for the bleeder). A reasonable estimate of 10% error is actable; however, regions of high turbulence could be higher. As stated in the previous section the ventilation system being tested is a U-tube ventilation system with a forcing fan.

Once the U-tube ventilation system is calibrated within 10% error, the bleeder fan was turned on in the simulation on at the same settings as the main fans. The bleeder fan was set up as an exhausting fan in both the physical scaled model and numerical simulation. This provided a final check to ensure the system was fully validated. A porosity region to simulate the gob is now needed for the CFD model.

There are various types of porosity models that are available in Cradle; the particle model was chosen for this study due to its similarity to model conditions. There are three variables used by the particle model: porosity, particle diameter, and shape factor. Since glass marbles where used in the scaled model, a shape factor of 1 (perfect sphere) and their respective particle diameter can be used; therefore, only porosity is the only true unknown. The particle size chosen for the model was 10mm which aligns with the model diameter used. A gob porosity of 0.1 and 0.15 was used in Cheng et al. (Cheng et al., 2016) therefore these values will be the base line for this study. Figure

3-9 shows the porosity zones used throughout the gob, and their corresponding input parameters can be seen in Table 3-2.

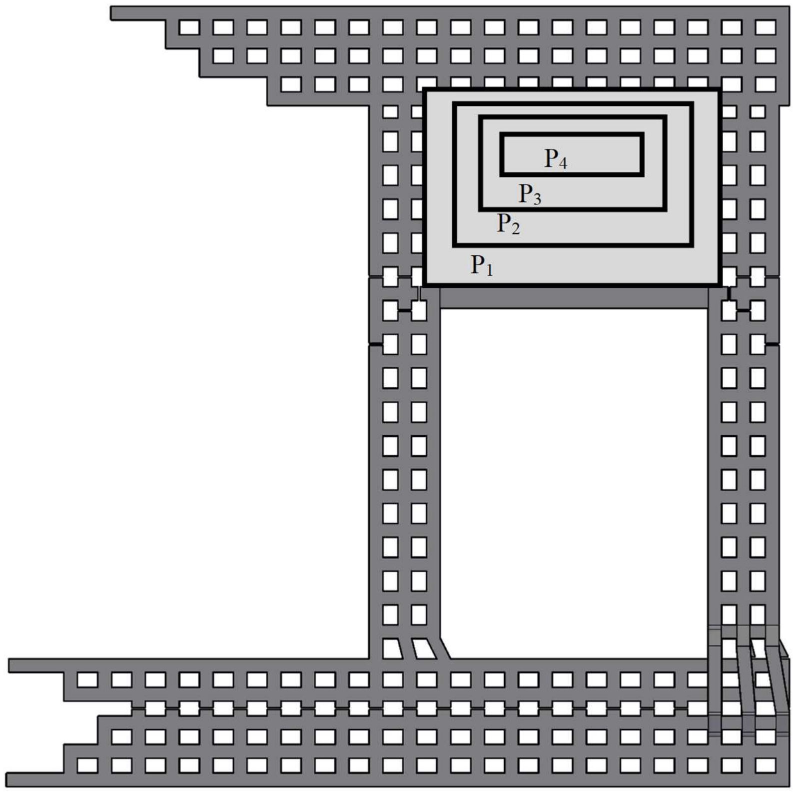

Figure 3-9 Gob porosity regions in the numerical simulation

Table 3-2 Gob porosities used for different porosity zones

Gob regions	P1	P2	P3	P4
Gob porosity	0.15	0.13	0.12	0.1
Shape factor	1	1	1	1
Particle diameter (m)	0.01	0.01	0.01	0.01

The main goal of the gob/bleeder simulation was to determine how well the porosity model can predict the airflow distributions around the gob and bleeder while simultaneously testing how well the CFD model can predict a more complex geometry. Simultaneously, the scaled model was tested again with the addition of 3 velocity measurement locations in the bleeder. These total 10 locations were shown in Figure 3-7**.** The headgate stoppings were kept completely closed while tailgate stoppings were fully removed (opened). The measured velocities were then compared to the CFD modeled velocities. The CFD model was then calibrated and adjusted for the scaled model measured results accordingly. Again, an estimated error of 10% is deemed actable as there is an inherent 5% error in the velocity measurements themselves.

This concludes the validation part for the CFD model. The objectives completed include the following:

1) The PSU mine model is proven to be sealed (<10% error).
2) A plan for meshing all future simulations is created
3) Air velocity measurements from a U-Tube scheme can be predicted by a CFD model (5%-10% error).
4) CFD air velocity measurements can predict bleeder and gob velocities (5%-10% error).

3.2 Ventilation System Investigations

3.2.1 Ventilation effectiveness: ideal conditions and stopping leakage

Turbulency and air quantity were directly related to methane control. It is well-known that turbulency can help methane dispersion in the air mixture and the air quantity can dilute the methane in the ventilation air. I used the validated CFD model to investigate the effects of different bleeder fan settings and stopping arrangements on the ventilation system. I wanted to point out that the upper corner of the tailgate is where the methane can accumulate and this area was the focused area in all my following studies.

Different headgate and tailgate resistances and bleeder fan pressure settings were simulated with each test and the results were compared to the U-tube scheme to determine its effectiveness. Two sets of testing were conducted. One is with no stopping leakage case and another is with leakage across the main. I referred these two cases as ideal and leakage scenarios. Furthermore, only airflow distributions were of interest in this section, therefore all simulations were conducted without methane source and emission.

To minimize the number of simulations, an initial test of bleeder fan settings was conducted. The main fan was set at 350 Pa (determined from the verification section) and the bleeder fan pressure was adjusted from 10-90% of the main fan pressure with each increment of 10%. This provided a baseline to determine the optimized bleeder fan setting for the pressure. Three bleeder fan pressures were selected. The selections were made based on the tailgate airflow split; an airflow split close to a 1:1 in the tailgate corner was selected as well as above and below this 1:1 ratio.

3.2.1.1 Ideal conditions without leakages

A total of 36 ideal condition scenarios were simulated, with three variables being investigated: bleeder fan settings, headgate entry resistance setting, and tailgate entry resistance setting. A total of 3 different bleeder fan pressures were simulated: 20%,40%, and 60% of the main fan pressure. These settings were determined in chapter 4 section 4.2.1.2. Next, the headgate entry resistance settings will be changed, this will vary the amount of air that is allowed to bypass the face and travel around the gob. Four different headgate resister arrangements will be tested; completely closing the headgate resister, then allowing 5%, 10%, and 15% of the cross-sectional area of each entry to be open. Finally, the tailgate resisters will be altered to allow 5%, 10%, and 15 % of the cross-sectional area to be open. In total 4 headgate resistances will be simulated each with 3 different tailgate resistances and each of those with 3 different bleeder fan settings. Table 3-3 shows the initial 36 simulations being conducted.

Table 3-3 Ventilation effectiveness variables for each simulation. (Bleeder fan pressure in chart)

Headgate / Tailgate	Closed			95% closed (high)			90% closed (medium)			85% closed (low)		
5% open (high)	20	40	60	20	40	60	20	40	60	20	40	60
10% open (medium)	20	40	60	20	40	60	20	40	60	20	40	60
15% open (low)	20	40	60	20	40	60	20	40	60	20	40	60

3.2.1.2 Stopping leakage handling in the simulation

The previous 36 simulations were performed under ideal conditions assuming no stopping leakages. However, this was not a realistic scenario, as stopping leakage can account for significant leakages throughout the mine. Therefore, the same 36 simulations were again tested under the same conditions with assumed stopping leakage quantify across the main. The updated AutoCAD geometry shown in Figure 3-10 **s**imulates leakage at the main stoppings. To allow airflow to pass from the intake to return, 5% of cross-sectional area was opened in every fourth stopping. These stoppings were circled in red in Figure 3-10**.**

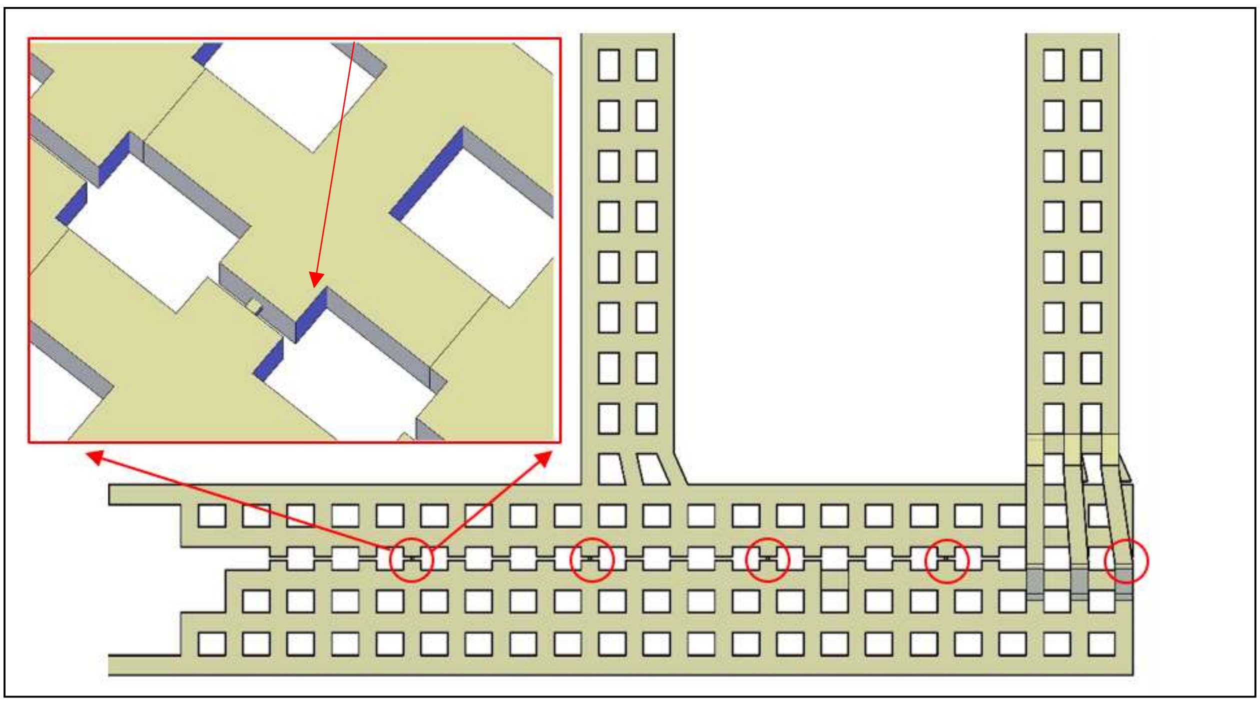

Figure 3-10 Altered model geometry for the addition of stopping leakage

3.2.1.3 Legend notations for ventilation effectiveness simulations

All 72 simulations for ideal and leakage scenarios were completed and the airflow analyses at the headgate and tailgate splits were investigated and discussed. For each simulation, the following ventilation parameters were recorded including headgate bleeder airflow, face airflow, return airflow, tailgate bleeder airflow, and finally airflow at the bleeder fan. The gob airflow cannot be easily measured because the flow was in a porous medium. After all the airflows were measured, the gob airflow was estimated from the simulated values. Gob airflow is the bleeder fan airflow minus the headgate and tailgate bleeder airflows. Figure 3-11 shows all of the simulated velocity measurements and their measuring points. The arrow colors in Figure 3-11 correspond to the bar color in Figure 3-12**.** Each simulation had a graph with two bars. The first bar labeled "Airflow around Headgate Split" corresponds to the total airflow going into the headgate (panel airflow), the second bar corresponds to all the airflow that doesn't travel down the headgate bleeder (airflow across the face). The second bar for each simulation should equal the yellow section (face airflow) of the first bar; however, due to measurement error from point velocity measurements some error is expected. Also, the total airflow for each bar and percentage of air going to the gob, return, and tailgate bleeder is shown. This can be seen in Figure 3-12. The title of each graph indicates the bleeder fan pressure and the corresponding tailgate setting while the headgate settings is shown under each set of bars.

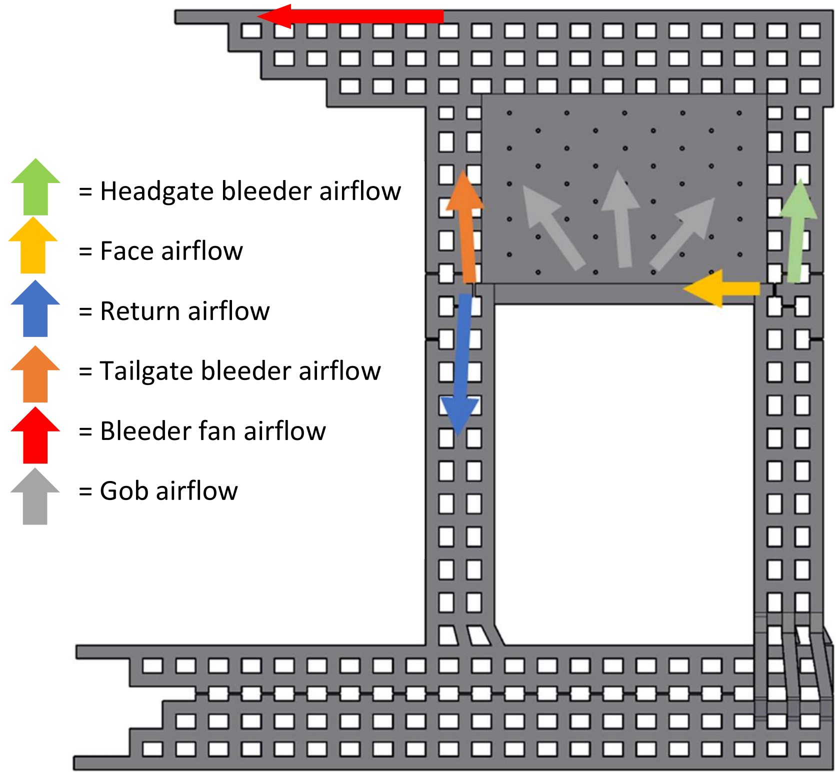

Figure 3-11 Location of airflow measurement point for the ventilation effectiveness graphs

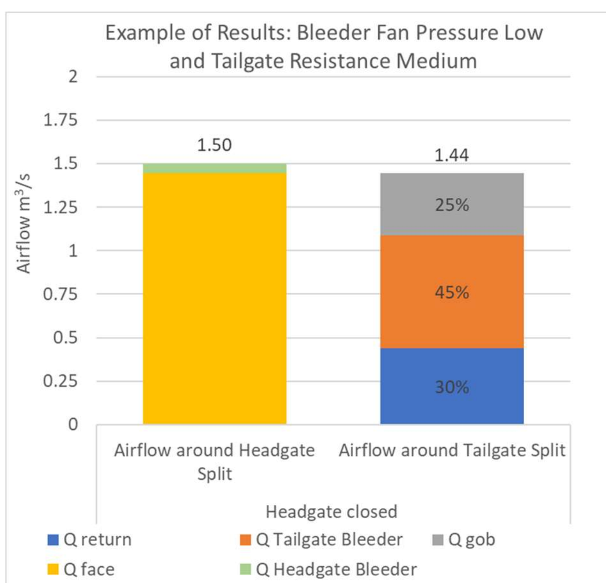

Figure 3-12 Example of bar graph made for the ventilation effectiveness simulations

3.2.2 Initial face advancement study (gob moves with the face)

A final set of simulations were conducted with the initial model geometry before the working face geometry is improved. These simulations focus on how advancing the face will affect the simulated velocity and methane distributions around the face. The tailgate corner is specifically focused in this section because it is widely known to have excessive methane concentrations and sporadic airflow patterns. Based on the literature review, no study has been reported for a dynamic face advancing with working gob and bleeder system. Furthermore, the headgate and tailgate stoppings remain in place for all the simulations. The simulation results provide valuable insights as to how the airflow patterns are altered by an active mining process. New geometries must be created to simulate this face advancement.

13 geometries were created for the face advancing simulation. The only geometry modification is the face location which is progressively moving toward the main and extending the gob as a result. Because the gob region was extended, the additional methane emission points were added to the gob. These points were located evenly throughout the gob and can be seen in Figure 3-13. In each created geometry the face and gob were advanced 1cm compared to the previous location. The same initial and boundary conditions were used for all 13 simulations which listed in

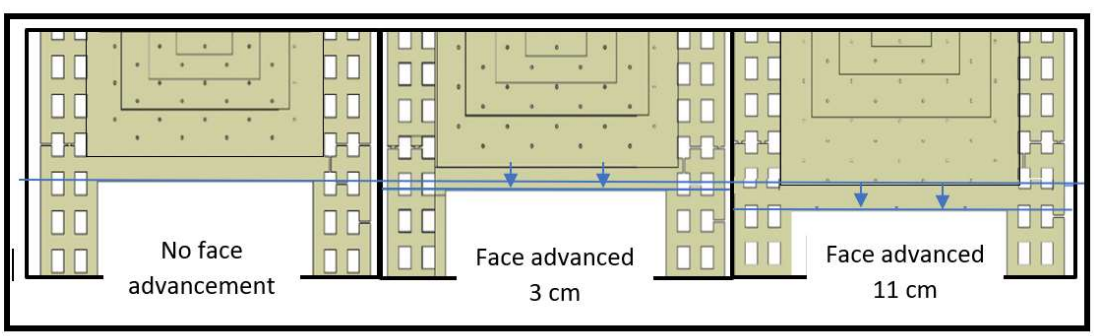

Figure 3-13 Advancing face geometry left no advance middle 3cm advance, right 11cm advance

Table 3-4. Figure 3-13 shows the differences between two of the geometries as 3 cm advance and a 11 cm advance.

As expected, the airflow patter would be somewhat similar because the flow geometry only varies slightly compared to the based model. Additional gas injection points were added as needed to accommodate the enlarging gob following the same pattern. All the simulation results were plotted and described in Chapter 4.

Table 3-4 Initial and boundary conditions used for primitive face advancement study

Main intake (Pressure inlet)	350 pa, 21.5°C, 100% air
Return (Pressure outlet)	0 pa, 21.5°C, 100% air
Bleeder (Pressure outlet)	-140 pa, 21.5°C, 100% air
Coal Face (Velocity inlet)	0.005 m/s, 21.5°C, 100% methane
Gob injectors (Velocity inlet)	0.005 m/s, 21.5°C, 100% methane
Walls	Rough surface, ER=0.0043m
Gob porosities	0.10, 0.12, 0.13, 0.15
Temperature (initial condition)	21.5°C
Pressure (initial condition)	101,025 Pa

3.2.2.1 Methane injection strategy and its boundary condition

The boundary condition for methane injection was created such that the methane concentration seen at the face should be 2%. While this is over the required action limit set forth by CFD 30 part 75 it provides a good framework for how to improve a faulty ventilation system. Since the methane entering the face must be constant for all the simulations, a velocity defined inlet was selected. Based on the methane inflow needed and the cross-sectional area of the gob and face injectors a velocity of 0.005m/s was estimated. The methane would enter the model through two areas the gob injectors and the mining face. The face provides a constant input volume of methane distributed equally throughout the entire face. The gob has a multitude of methane injection points as illustrated in Figure 3-13. Each methane injector is a velocity inlet and methane flows equally through each of these points. As the face retreats more methane injection points were added to accommodate the pattern illustrated in Figure 3-13.

3.2.3 Improving the face geometry with shields and an armored face conveyor (AFC)

Previously the CFD geometry was simulated without any objects in the longwall face i.e. no shields or AFC. For the remaining simulations shields and an AFC were added across the longwall face to simulate a working longwall face. Precision in the geometry of these added objects cannot be expected as it would greatly increase computations time and provide marginal returns on airflow patterns. Therefore, rough geometries were made of only key parts of each objects. Simplifying the geometry is typically done throughout CFD studies to help the mesh creation process and to decrease computational time. The longwall shields and AFC were shown in Figure 3-14 from multiple viewing angles.

Since the shields and AFC were used for the three remaining sections, I first created a baseline to compare future test results. One simulation was conducted with the addition of the shields and AFC under the initial and boundary conditions shown in Table 3-5**.** For the duration of the simulations the shields and AFC were considered as a solid object with the material specified as steal.

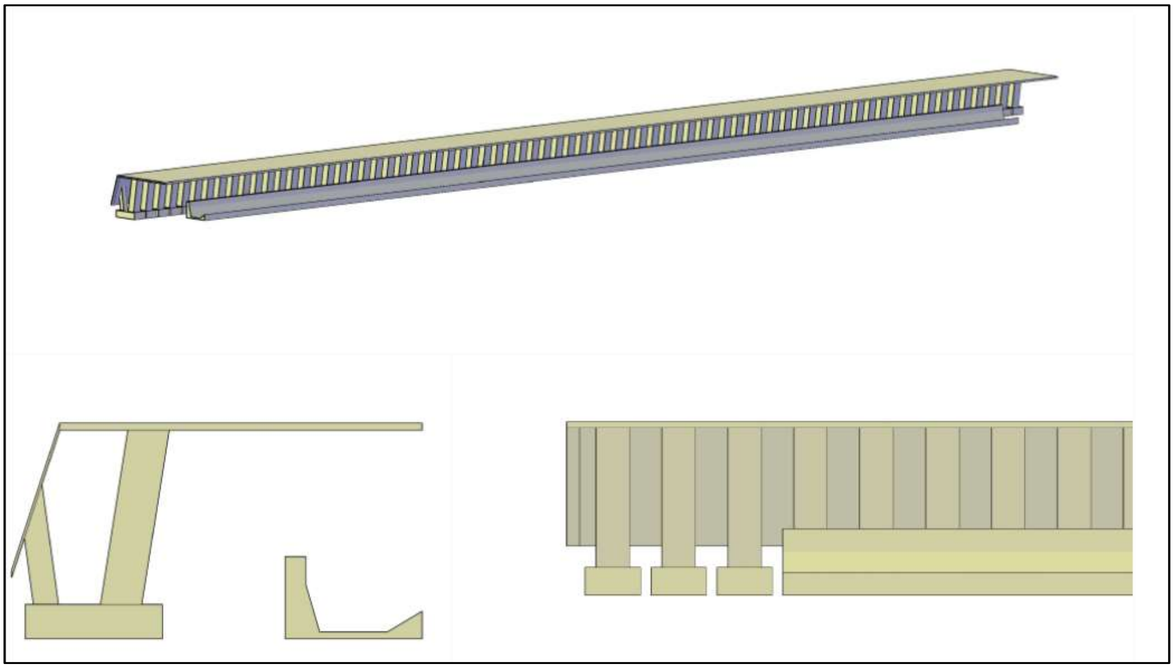

Figure 3-14 Multiple views of the added shields and AFC geometry

Table 3-5 Initial and boundary conditions for baseline model simulation

Main intake (Pressure inlet)	350 pa, 21.5°C, 100% air
Return (Pressure outlet)	0 pa, 21.5°C, 100% air
Bleeder (Pressure outlet)	-140 pa, 21.5°C, 100% air
Coal Face (Velocity inlet)	0.005 m/s, 21.5°C, 100% methane
Gob injectors (Velocity inlet)	0.005 m/s, 21.5°C, 100% methane
Walls	Rough surface, ER=0.0043m
Gob porosities	0.10, 0.12, 0.13, 0.15
Temperature (initial condition)	21.5°C
Pressure (initial condition)	101,025 pa

3.2.4 Face advancement simulations with stagnant gob

In the literature, some studies have studied the interactions between the longwall airflow and the gob immediately behind the shields. The bleeder system has not been simulated in the past reported literature. One question that has been of interest is how the ventilation air interacts with an advancing face and a lagging gob. At certain conditions, the immediate roof does not collapse right after the shield advanced because of combined effects of strong roof and stress conditions. This leaves an open area behind the shields in which air and methane could accumulate. Three different geometries were simulated with a goal to observe how the face airflow interacts with the gob and this empty region behind the shields. The three different geometries can be seen in Figure 3-15 with the only alterations being that the face has advanced 1 cm in each case. Simulation were conducted under the same initial and boundary conditions as the previous section and are listed in Table 3-5 and meshed in the manor described in the mesh independence study. Results are presented in figures in chapter 4 which describe the velocity and methane interaction specifically around the face and shields. A discussion about the created figures and the baseline study is then presented.

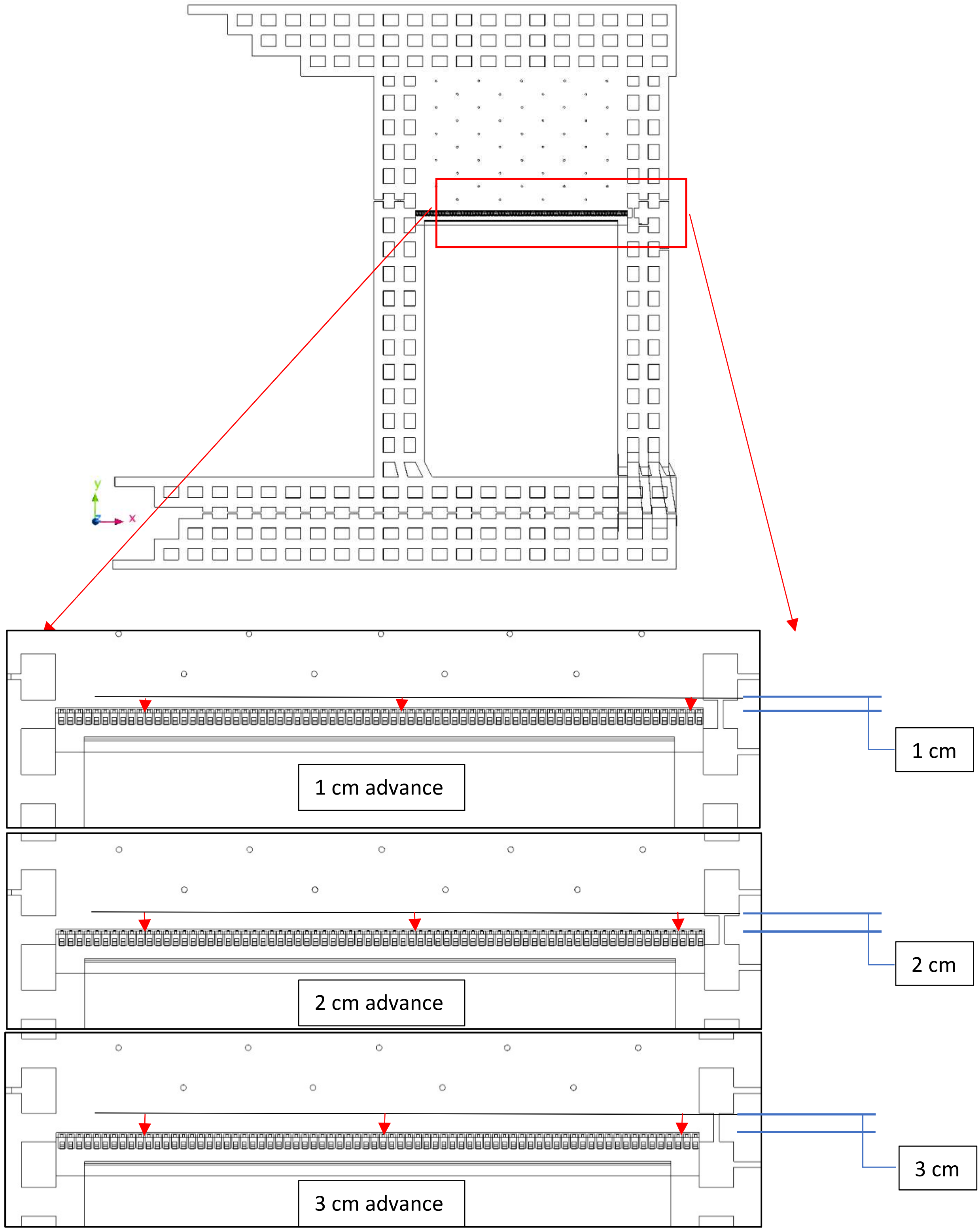

Figure 3-15 Different face geometries for the face advancement study

3.2.5 Roof incident

3.2.5.1 Roof incident simulations: tailgate corner

Since the 2010 Upper Big Branch disaster, there has been much focus on the mitigation of methane around the face and its adjacent regions. It is crucial to know how a mine ventilation system preforms under normal circumstances for the baseline information. It is also important to understand how the ventilation system reacts to the possible ventilation failure cases. However, few CFD studies have been conducted to determine what would happen to the airflow patterns in a minor or major emergency scenario such as a roof falls or air course convergency. As an example, these simulations showed the ventilation system around the longwall face in an effort to determine how severer roof sag or roof failures (together called roof incident) at an intersection of the tailgate entries and cross-cuts can affect the airflow down the tailgate and methane control around the face. These simulations were conducted by creating four new model geometries with different locations and severity of roof falls.

There are three roof incidents, and their locations can be seen in Figure 3-16. Each of the three locations were simulated as an isolated roof fall event with a fourth simulation being a combination of all three locations. This should provide a comprehensive look as to what will happen if the roof surrounding the tailgate corners were to sag or fail. Since roof incidents are unknown until miners find them this approach, of simulating multiple locations as well as multiple severities, can show how severity and location of roof fall can influence the ventilation system. With the ultimate goal of providing a precursor in the ventilation data to a miner finding the roof incident.

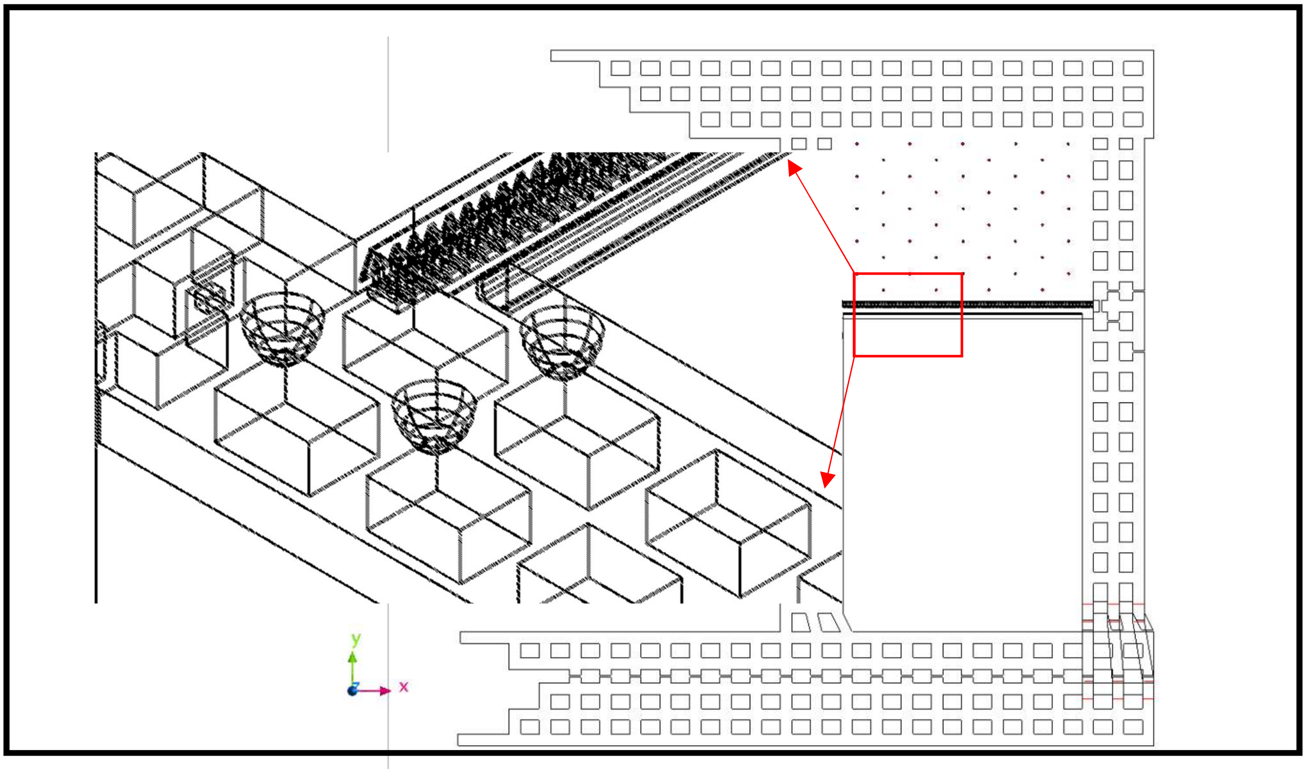

Figure 3-16 Simulated roof incident locations

Each simulation was conducted under the same initial and boundary conditions which were shown in Table 3-5. The only differences between the simulations will be the location of the specific roof incident for the simulation. Furthermore, the mesh scheme that was identified in the mesh independence study was used for all meshing. Since the main focus of this study is on how the roof incident affects the methane concentrations around face and tailgate these areas will be focused in the figures. Also, the methane concentrations at multiple height were created; these figures show the methane concentration at 25%, 50% and 75% of the mining height. Results were then compared to the initial baseline test of the longwall face that was conducted earlier in the improving geometry section.

3.2.5.2 Roof incident simulations: tailgate corner with curtain

In the previous section, the ventilation system was simulated in a disaster event, a roof incident in the T-split. It is shown in Chapter 4 section 4.2.5.2 that methane concentrations increase as and airflow across the face decreases which can potentially create pockets of methane within the T-split region. To follow a risk management approach, the next step after identifying an event has occurred is to determine ways to mitigate this event. These simulations place a curtain in the walkway of the longwall face to increase the turbulence across the face and create mixing. The goal these curtains was to create enough turbulence to fully utilize the mine ventilation air to dilute the incoming methane. As described in Chapter 4 section 4.2.5.2, the turbulence across the face in minimal and if the turbulence increased enough the methane can evenly distribute around the ventilation air leading to a seemingly lower overall methane concentration and a safer environment.

Curtains have long been used in the mining industry to block or redirect airflow in ways which are desired. Curtains and auxiliary ventilation systems are used in entry driving to divert fresh air around the continuous miner. While this method does not decrease the average overall methane concentration in the air, it does dilute the methane across more of the ventilation air making it seem as though the concentration decreased. I introduced the curtains for the same reason to create turbulent environment for the full dispersion. However, curtains have not been introduced across the longwall face as a way to promote mixing and turbulence before as a common practice. While hanging curtains along the face could increase resistance of the longwall and may be a hindrance to miners at the face they could be deployed automatically once a disaster has realized. Therefore, these simulations aimed to determine what effects by placing two curtains along the face on both the airflow in a non-disaster environment for a pseudo baseline and a disaster environment.

The shape of the curtain has long been a large variable in the mining practice. It was determined that a curved curtain with a small hole in the center provides good airflow disruption while keeping the pressure loss and potential ‘dead zone’ behind the curtain low. Figure 3-17 shows the shape and placement of the two curtains in the longwall panel. The same shape curtains were used for both curtains. As shown in Figure 3-17 the curtains are placed roughly at the middle of the panel, this was intentionally done to determine the effect of the curtains on the streamlined airflow.

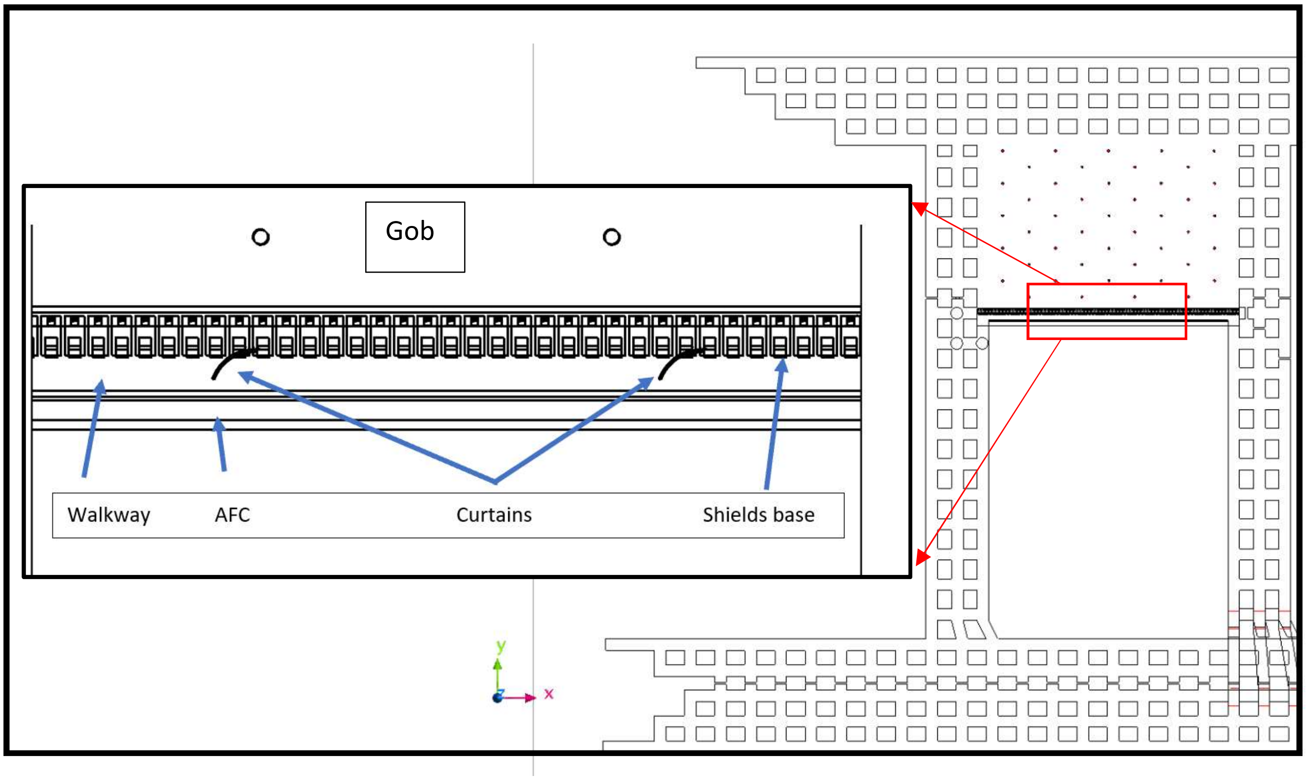

Figure 3-17 Curtain geometry and Curtain placement

The first simulation consisted of the two-curtain placement with no roof falls, this allowed a comparison between the curtain and no curtain simulations to be made. Next, the two curtains were added to the geometry for all four of the roof incident scenarios. The initial and boundary conditions were the same as listed in the roof fall with no curtain section with the only alteration being the added curtain geometry. Furthermore, the mesh scheme that was identified in the mesh independence study was used for all meshing.

Chapter 4

Results

4.1 CFD and Scaled Model Calibration

4.1.1 Sealing of Scaled Model

Initial testing trails of the PSU physical-scaled model showed an air leakage of 75% because of the stopping leakages. The physical model was then sealed by gluing with hot gun glue. The final sealed model was found to have less than 10% leakage by using the hotwire anemometer measurements. Total airflow in and out of the model for the sealed model was listed in Table 4-1, airflow measurements were taken from points 2 and 7 as shown in Figure 3-7. In total the model was sealed in 6 trials with the final air leakage is approximately 8%. The total airflow entering into the model was measured to be 1.20 m^3/s and 1.10 m^3/s existed out the model. Figure 4-1 shows the calculated airflow at each of the seven locations; after 4 trials it became clear that Point 1 was under high turbulence and its values were increasingly similar to that of Point 2. Therefore, Point 1 was dropped as a measuring point because its unstable airflow due to highly turbulence. After the 3rd test, a clear trend along the face emerges. Airflow measured along the face were around 1.25 times lower than what was expected. Since the face has a larger cross-sectional area the wall effect is believed to account for the 1.25 difference, this was also seen for all CFD simulation results. Once this 1.25 factor was taken into account the airflow throughout the model is relativity constant as expected. Some leakage was measured across the headgate and tailgate stoppings despite great attention being made to seal these stoppings. Table 4-2 lists the raw airflow measurements with Figure 4-2 showing the measured headgate and tailgate leakages and adjustments made to the airflow across the face for the final trial. After 6 sealing attempts of Scaled model was determined to be sealed with an airflow error dropping down from 75% to 8%.

Table 4-1 Scaled model leakage data

Test number	1	2	3	4	5	6
Airflow in m^3/min	1.31	1.25	1.13	1.21	1.21	1.20
Airflow out m^3/min	0.33	0.78	0.83	0.86	0.99	1.10
% of Airflow Lost	75.1%	37.7%	26.5%	28.7%	18.4%	8.3%

Table 4-2 Fully adjusted final airflow measurements

Location	Main	Headgate	Face 1	Face 2	Tailgate	Return
Measured Airflow m^3/min	1.2	1.16	1.15	1.15	1.1	1.1

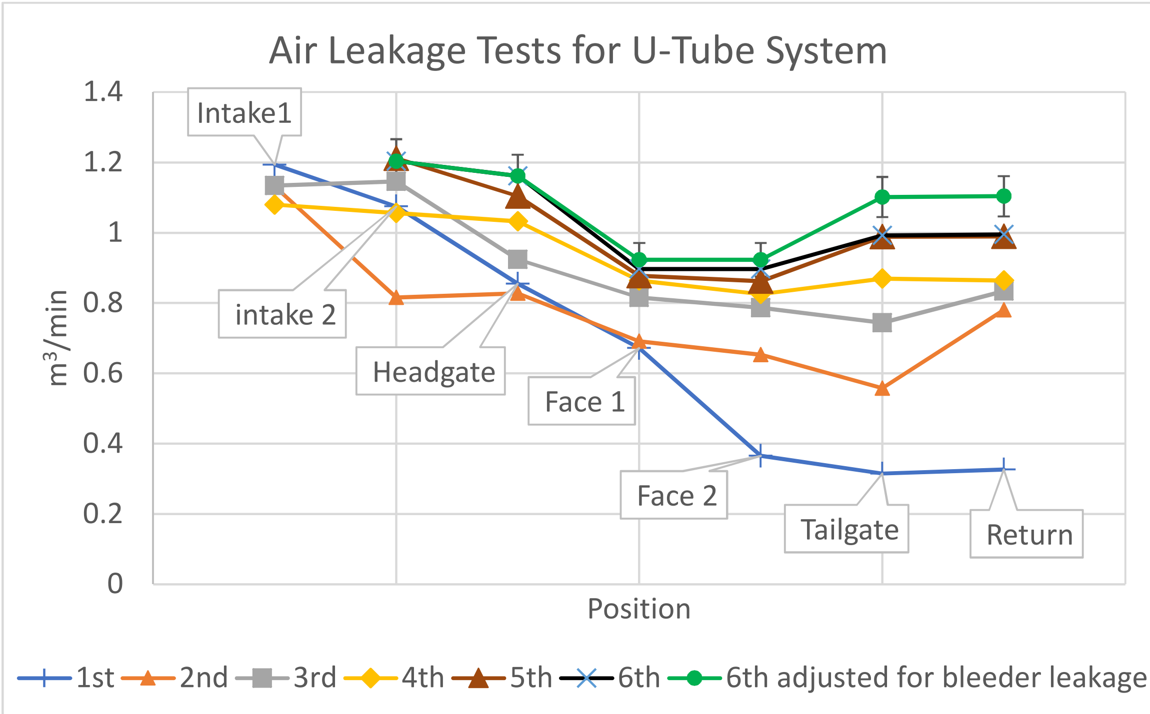

Figure 4-1 Airflow measurements throughout model sealing process

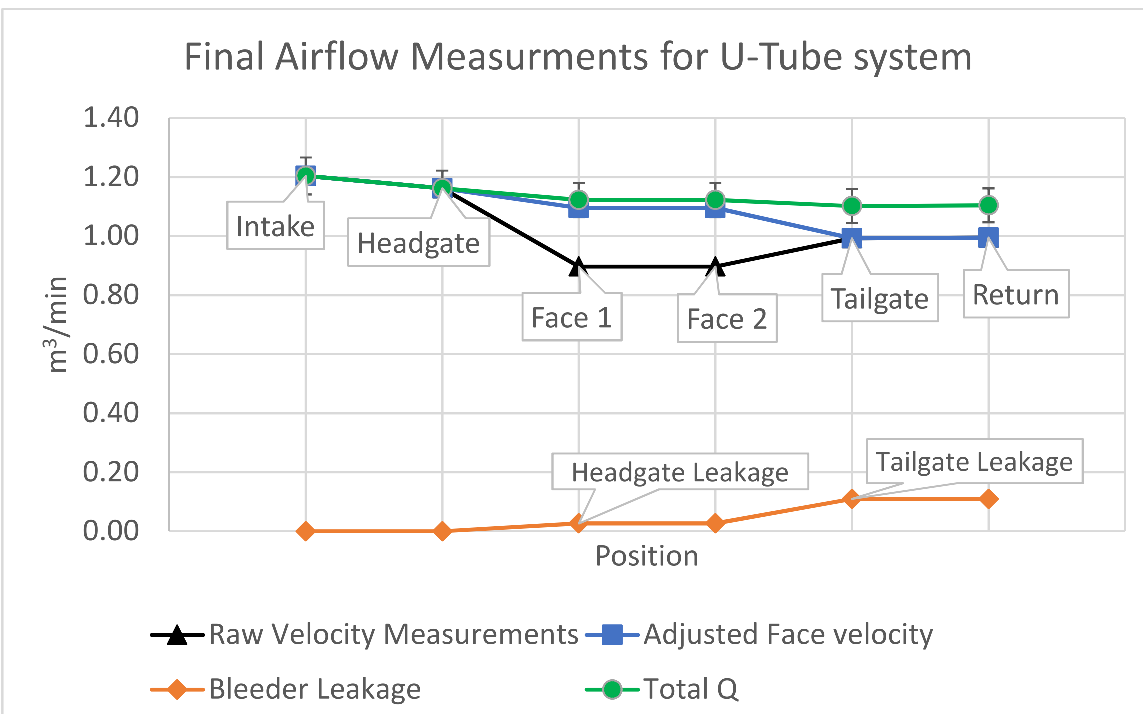

Figure 4-2 Final airflow measurements from leakage testing

4.1.2 Mesh Independence Study for CFD Model Establishment

For CFD modeling, the mesh size can determine the computational efficiency and the accuracy of the modeled results. I run a series of mesh size CFD models to determine the optimized mesh size for my study. Figure 4-3 A-E showed a drastic difference between the large cell sizes and the small cell sizes and the deviation started to negligible when cell size is 0.5 cm or less at which the velocity profile around the headgate corner becomes plausible. Furthermore, a significant increase in clarity can be seen from the 0.5 cm to 0.25 cm, and subsequently 0.125 cm cell size; however, the overall shape and trend of the velocity doesn't change. Based on these preliminary trails, 0.5 cm was determined for the largest cell size in my subsequent studies. Table 4-3 shows the variables collected from the five simulations with the velocities graphed in Figure 4-4. I compared 0.25 and 0.125 cm cell sizes and found that there is negligible difference between these two cell sizes and the computational time of 0.125 cm was significantly higher than 0.25 cm. I chose not to use 0.125 cm and the minimum cell size is 0.25 cm. Further decreases in computational time should be explored because this study was designed to conduct over 100 simulations. I wanted to point out that I did not consider to include methane in the simulation because adding one mixing gas can triple the computational time based on my trail experience. Therefore, a strategy for creating cell sizes must be enacted.

For the general areas of non-interest such as the mains, headgates, tailgates, and bleeder systems a cell size of 0.5 cm can be justified because no locations specific data would be needed for analysis. However, for the areas of interest such as: the face, any simulated roof falls, the tailgate corner, the headgate corner, the shields, the AFC, and methane injection points a cell sizes of 0.25 cm were used in the study. Again, since no substantial difference can be seen from 0.25 cm to 0.125 cm the increased clarity of the 0.125 cm cells is not worth the extra computational time. This method was used for generating all the mesh network throughout this study.

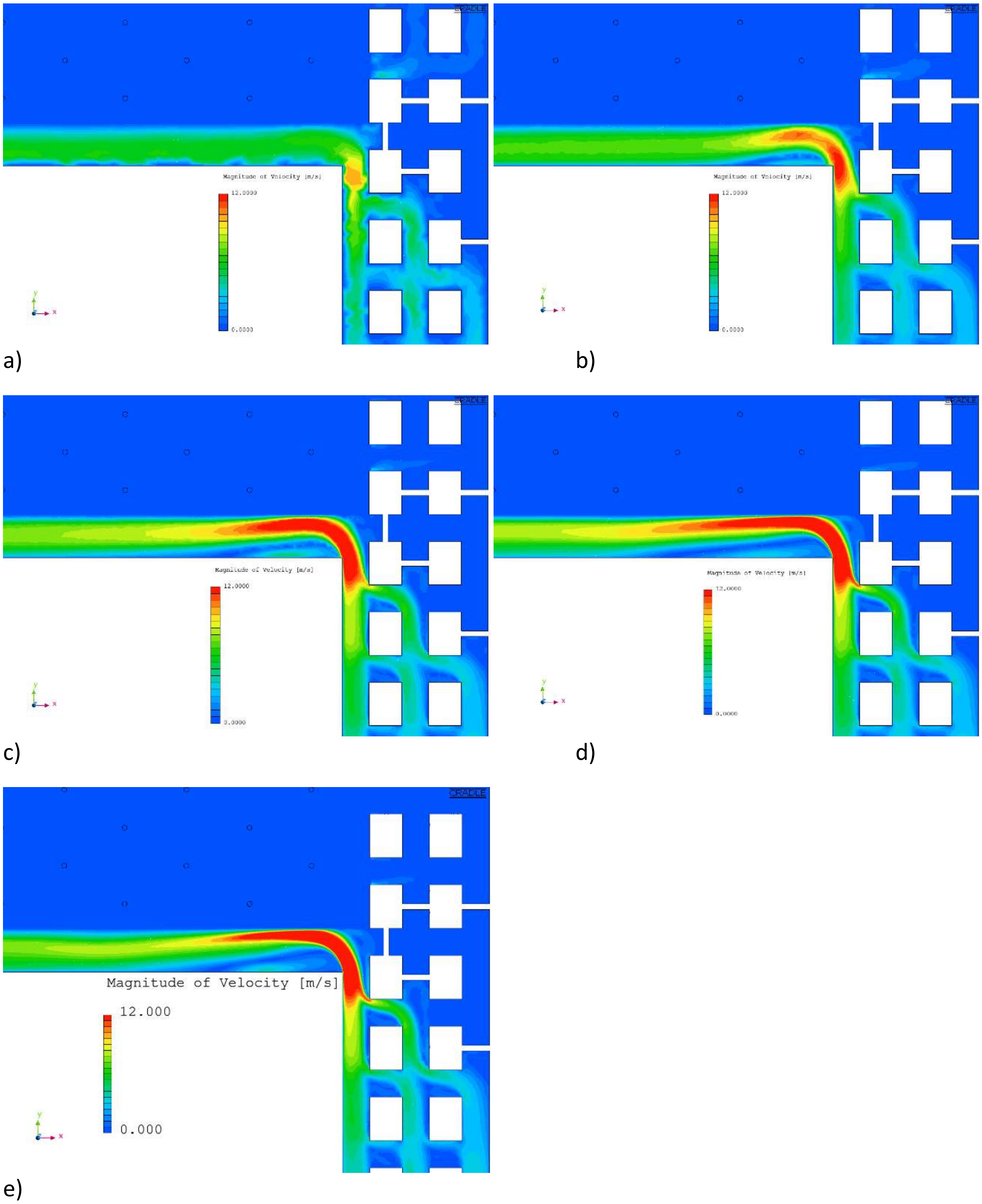

Figure 4-3 Velocity profile for headgate corner bend (cell size: A 2cm, B 1cm, C 0.5cm, D 0.25cm, E 0.125cm)

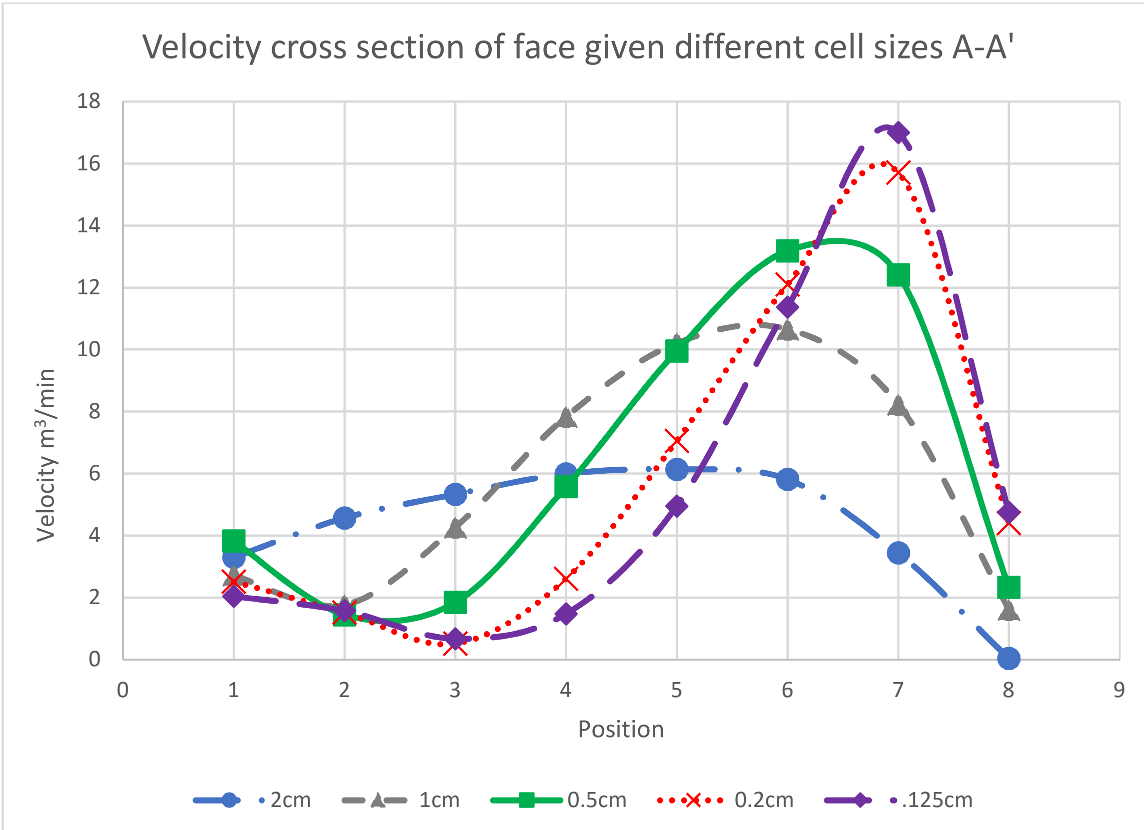

Figure 4-4 Graph of velocity from 8 points across A-A’

Table 4-3 Velocity data from A-A’ for the mesh independence study

point	Position			Cell Size				
	X	Y	Z	2cm	1cm	0.5cm	0.25cm	0.125cm
1	122.48	-61.620	120.00	3.29	2.71	3.82	2.51	2.03
2	122.48	-61.610	120.00	4.56	1.76	1.43	1.51	1.56
3	122.48	-61.600	120.00	5.32	4.26	1.84	0.51	0.66
4	122.48	-61.590	120.00	5.98	7.83	5.57	2.60	1.47
5	122.48	-61.580	120.00	6.13	10.20	9.95	7.05	4.95
6	122.48	-61.570	120.00	5.81	10.65	13.18	12.09	11.37
7	122.48	-61.560	120.00	3.44	8.23	12.41	15.70	17.00
8	122.48	-61.640	120.00	.03	1.6	2.32	4.39	4.75
Cycles till convergence				50	57	126	158	374
Computational time (min)				15	20	75	190	540
Total number of cells (million)				~0.29	~0.93	~3.8	~6	~12.8

4.1.3 Calibration of CFD model with scaled model

4.1.3.1 U-Tube System

The scaled model was sealed and airflow measurements from the seven different locations were obtained. The data has been discussed in Chapter 3 and they were listed in Table 4-1. The mesh generation for these simulations follows the plan laid out in the mesh independence study. The maximum airflow of 1. 2 m^3/min was achieved through the main section of the scaled model. Figure 4-5 shows the initial model geometry with the final boundary conditions marked. The guess and check method were used to

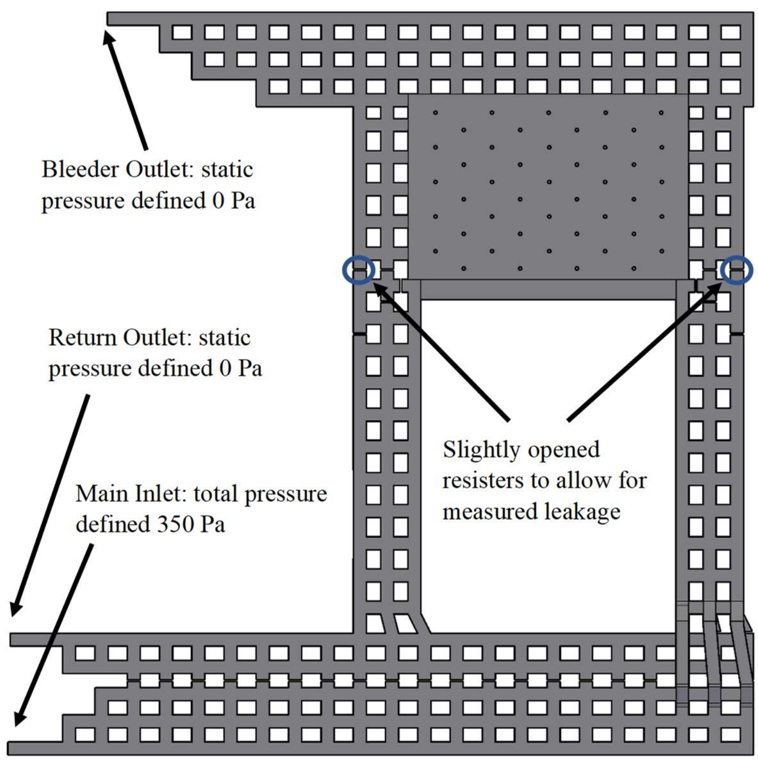

Figure 4-5 Model geometry and boundary conditions

determine these values as they very closely aligned with the measured scaled model values. 2% of the cross-sectional area was opened at the headgate and tailgate to allow for the measured leakage that was experienced in the sealing section.

Table 4-4 Results from U-Tube CFD simulation compared to the physical scaled model measurements

Measured Airflow (Q, m^3/min)						
	Intake	Headgate	Face 1	Face 2	Tailgate	Return
Measured Scaled Model	1.20	1.16	1.15	1.15	1.10	1.10
CFD	1.21	1.19	1.31	1.24	1.03	1.06
Relative Error	0.50%	2.4%	13.5%	7.5%	-6.5%	-4.0%

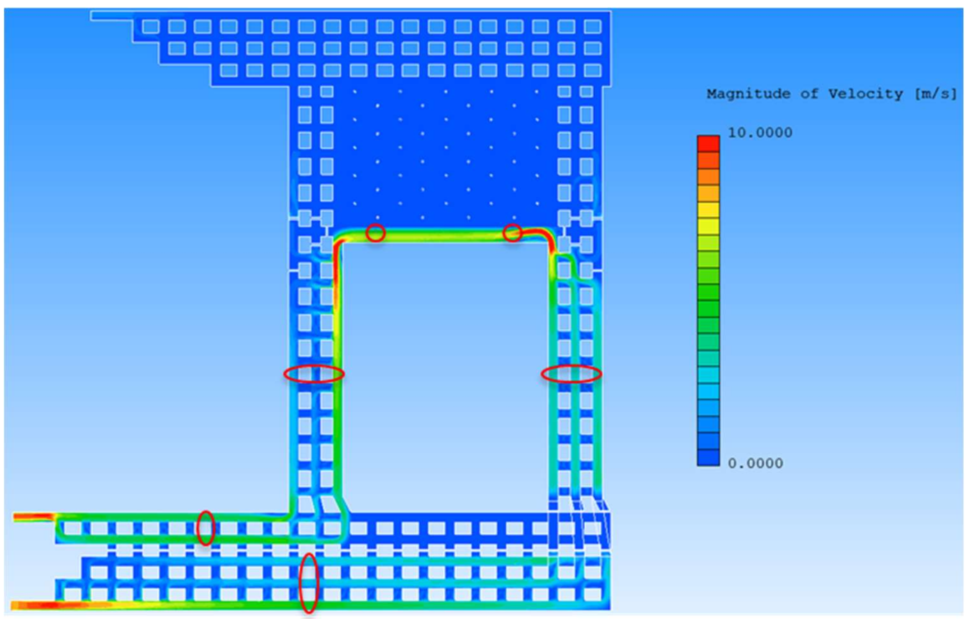

Figure 4-6 Velocity profile of U-tube ventilation scheme

After many guess and check trials, it was determined that a total main fan pressure of 350 pa was needed to create an intake airflow of 1.2 m^3/min with the return and bleeder fan pressures being set to be 0 Pa. Furthermore, the wall roughness was initially calculated at 0.0045 m from an equivalent roughness formula given plastic as a material; however, a roughness value of 0.0043 m was determined to be desirable based on the similarity between measured and simulated airflows.

Table 4-4 shows the measured and simulated airflows at six locations which were marked as red circles on Figure 4-6. For errors, the main and headgate were seen to be under 1% and 2.5%, while areas of high turbulence such as the face showed a relatively high error of 7.5% and 13.5%.

These errors were acceptable because the hot wire anemometer has an inherent error of 5%. Also, all the velocity measurements taken in the model and CFD simulation were taken from a single point (middle of the entry). It is well known that a multi-point traverse of the entries is a better characterization of the airflow. However, due to the size of the scaled model and complexity of the CFD simulation only a single point was possible.

4.1.3.2 Gob Permeability / Bleeder Calibration

Once the U-tube scheme was validated the bleeder system was fully opened and the bleeder fan was turned on to high. The resulting airflow distribution can be seen in Figure 4-7, it is believed that the return airways acted as an inlet to create more of a Y-scheme ventilation network. Due to the physical limitations of the model the tailgate edge of the model was not able to be sealed in the same manner as the rest of the edges. Therefore, when put under negative pressure air can be measured coming into the model at a rate of 0.17 m^3/min as seen in Figure **4**-7. Airflow through the gob region is estimated to be approximately 1 m^3/min which accounts for approximately 68% of the ventilation air.

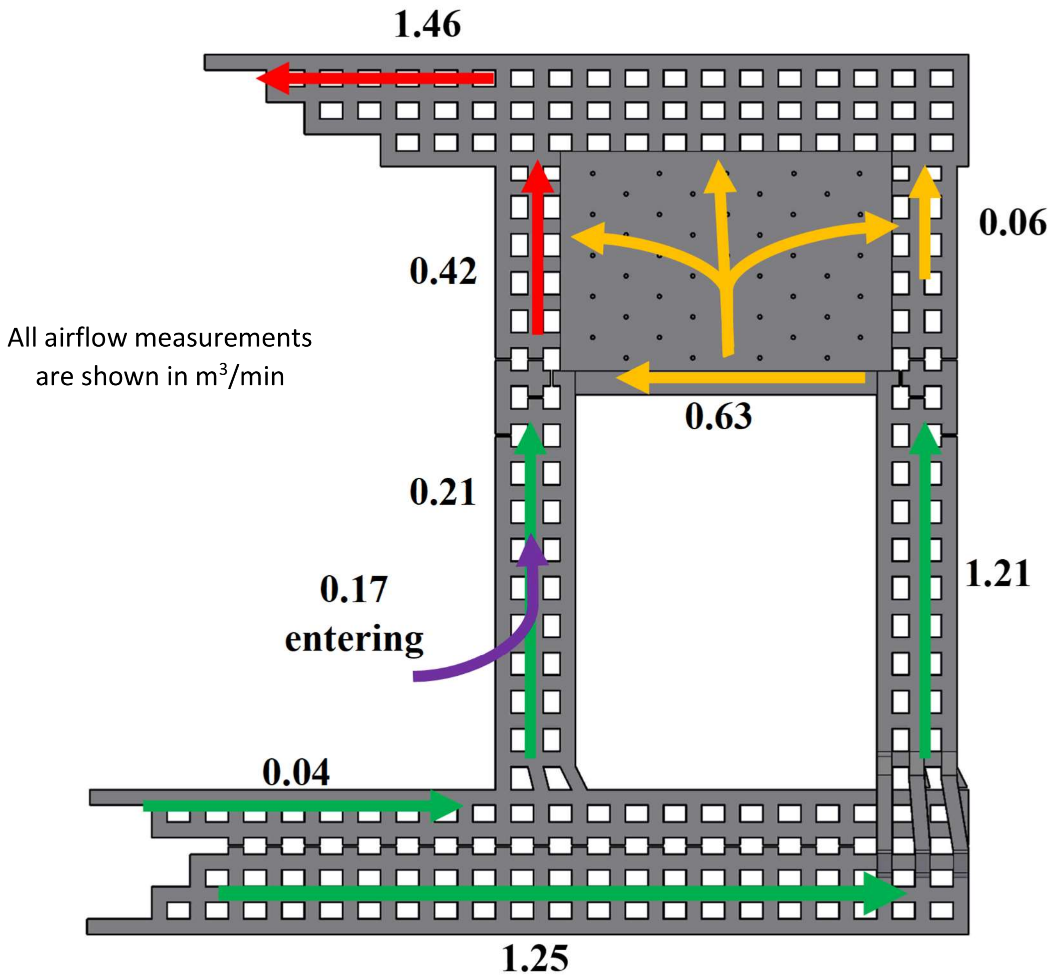

Figure 4-7 Airflow measurements of scaled model with working bleeder system

4.2 Ventilation System Investigations

4.2.1 Ventilation Effectiveness

4.2.1.1 Varying Bleeder Fan Parameters

As stated in the method section airflow distributions around the face and tailgate corner will be investigated while varying three ventilation parameters: bleeder fan pressure, headgate resister, and tailgate resister settings. From the calibration section initial and boundary conditions will be set according to Table 4-5.

Table 4-5 Initial and boundary conditions used for ventilation effectiveness simulations

Main intake (Inlet)	350 pa, 21.5°C, 100% air
Return (outlet)	0 pa, 21.5°C, 100% air
Bleeder (outlet)	User defined pa, 21.5°C, 100% air
Walls	Rough surface, ER=0.0043m
Gob porosities	0.10, 0.12, 0.13, 0.15
Temperature (initial condition)	21.5°C
Pressure (initial condition)	101,025 pa

An initial test was conducted to determine which three bleeder fan settings to choose. The goal was be to have the face airflow split in the tailgate at a 1:1 ratio; then determine another 2 bleeder fan settings in which the ratios are above and below 1:1. Table 4-6 shows the tailgate split airflow ratios with the accompanying bleeder fan pressure. The bleeder fan pressure of 40% roughly correlates to a 1:1 ratio; therefore, the bleeder fan pressures of 20, 40, and 60% were chosen to be investigated further.

Table 4-6 Tailgate air split ratios from various bleeder fan pressures

Bleeder Fan Pressure (Pa)	280	245	210	175	140	105	70	35
Percent of Main Fan Pressure	80	70	60	50	40	30	20	10
Tailgate Split Ratio	1.54	1.38	1.23	1.09	0.96	0.84	0.72	0.61

The headgate and tailgate resistances are defined by the amount of cross sectional that is left open in the entry. Table 3-3 shows all the headgate and tailgate settings used for the following simulations. Airflow Graphs from all 72 simulations are shown as follows starting with ideal conditions.

4.2.1.2 Ideal Conditions

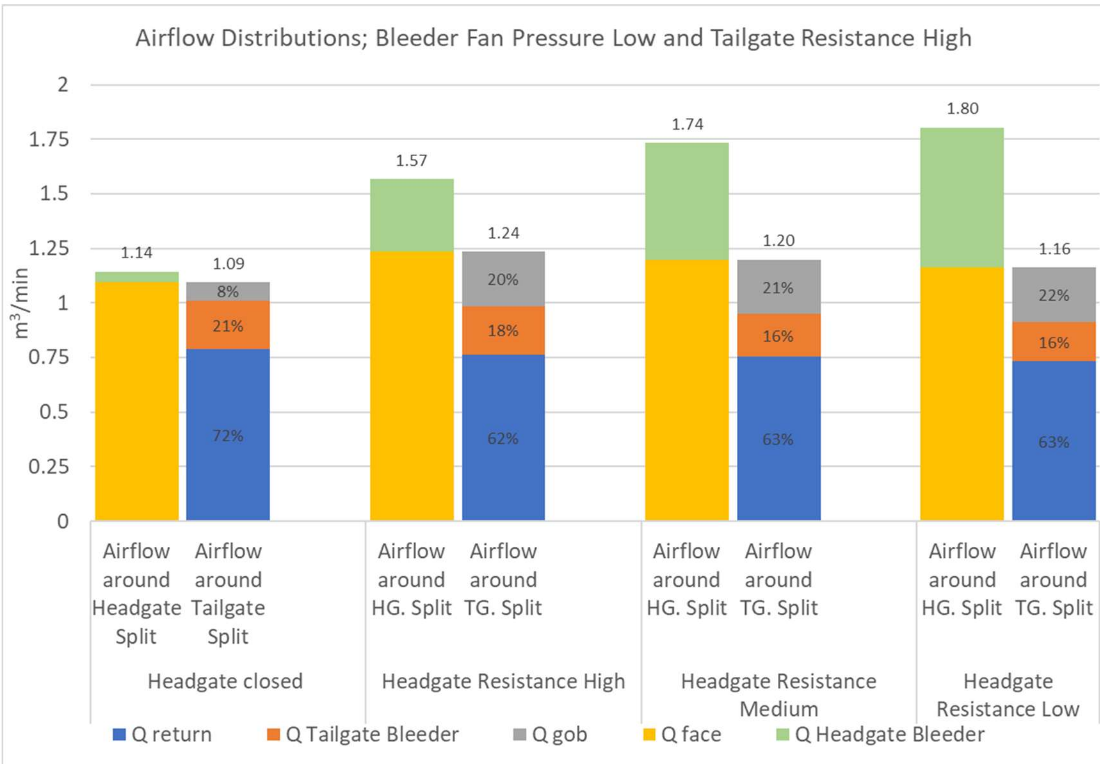

Figure 4-8 Ideal ventilation effectiveness simulations

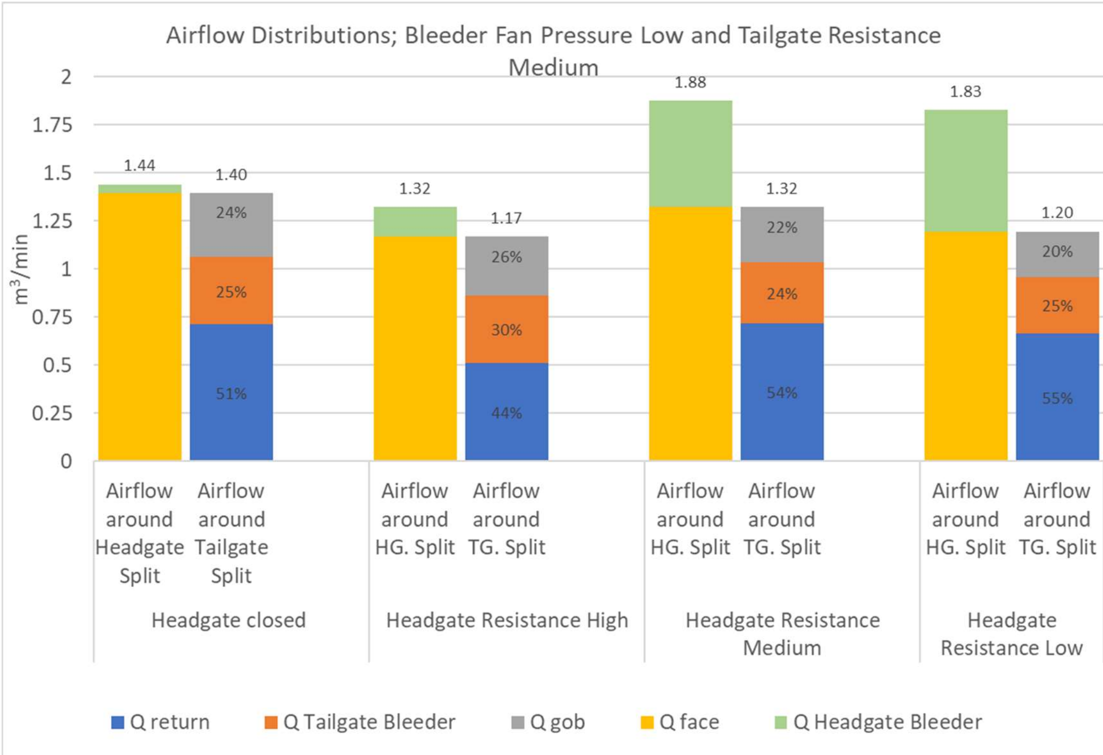

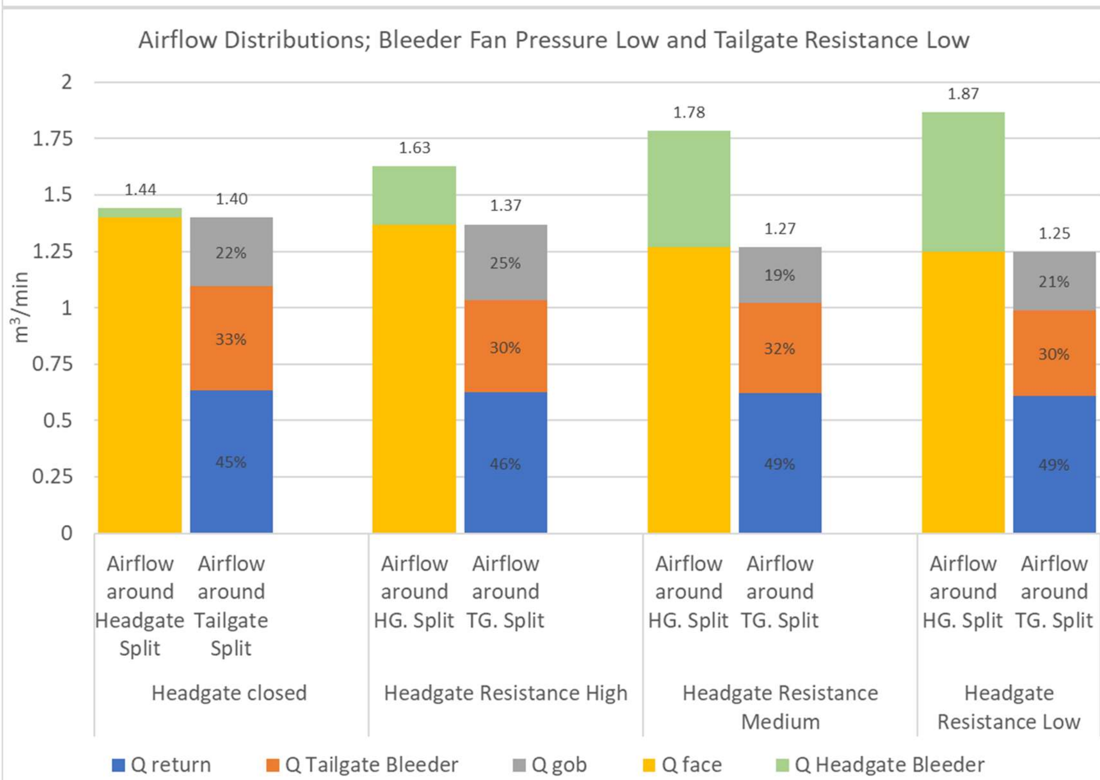

Figure 4-9 Ideal ventilation effectiveness simulations cont.

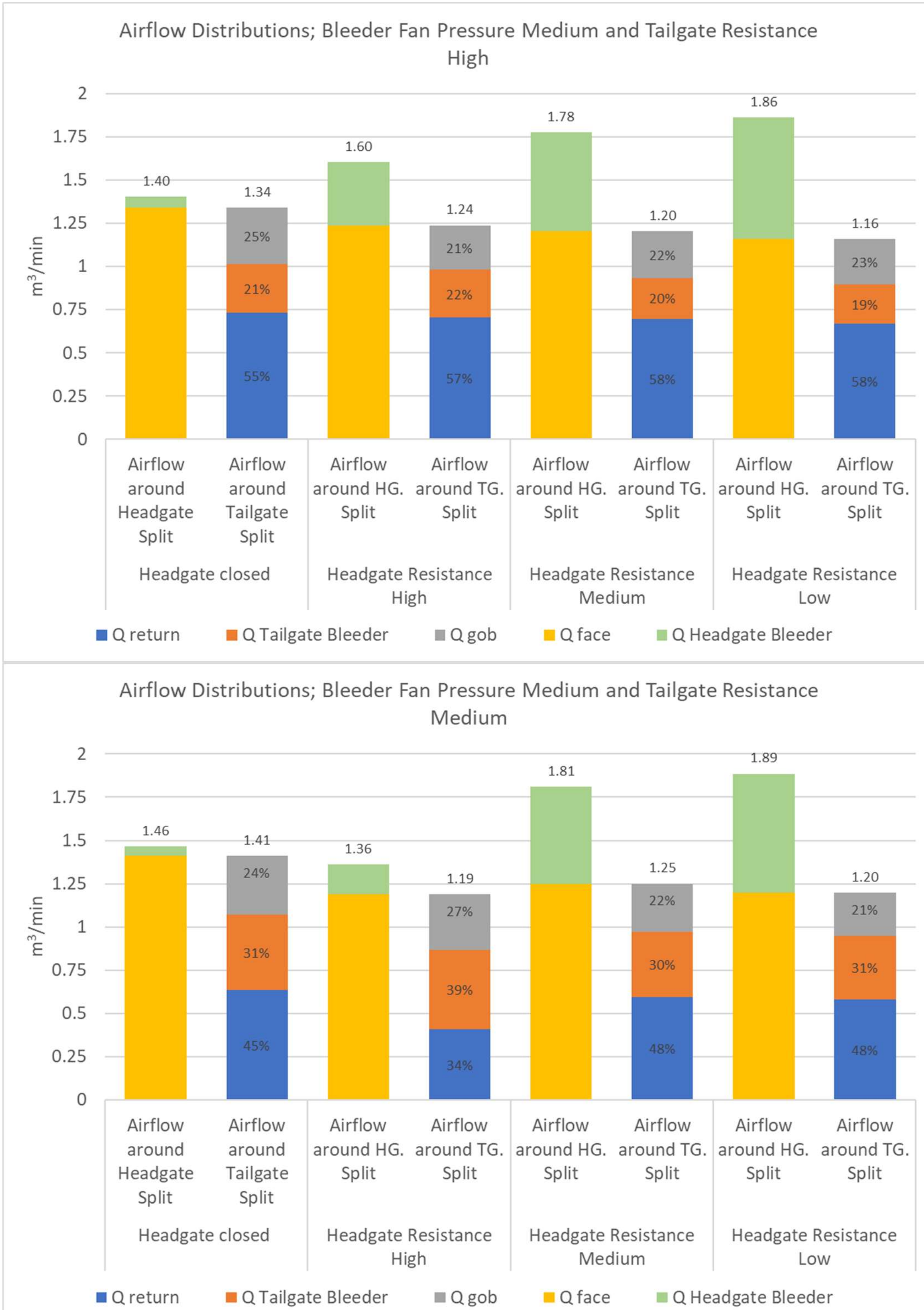

Figure 4-10 Ideal ventilation effectiveness simulations cont.

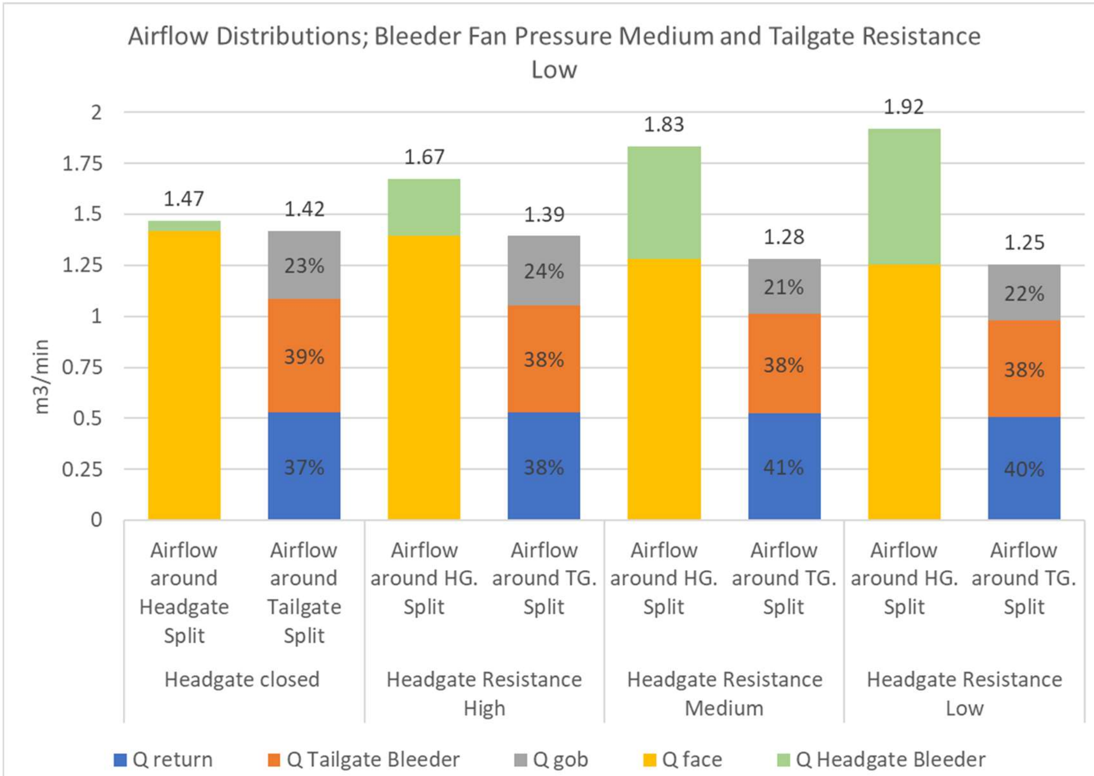

Figure 4-11 Ideal ventilation effectiveness simulations cont.

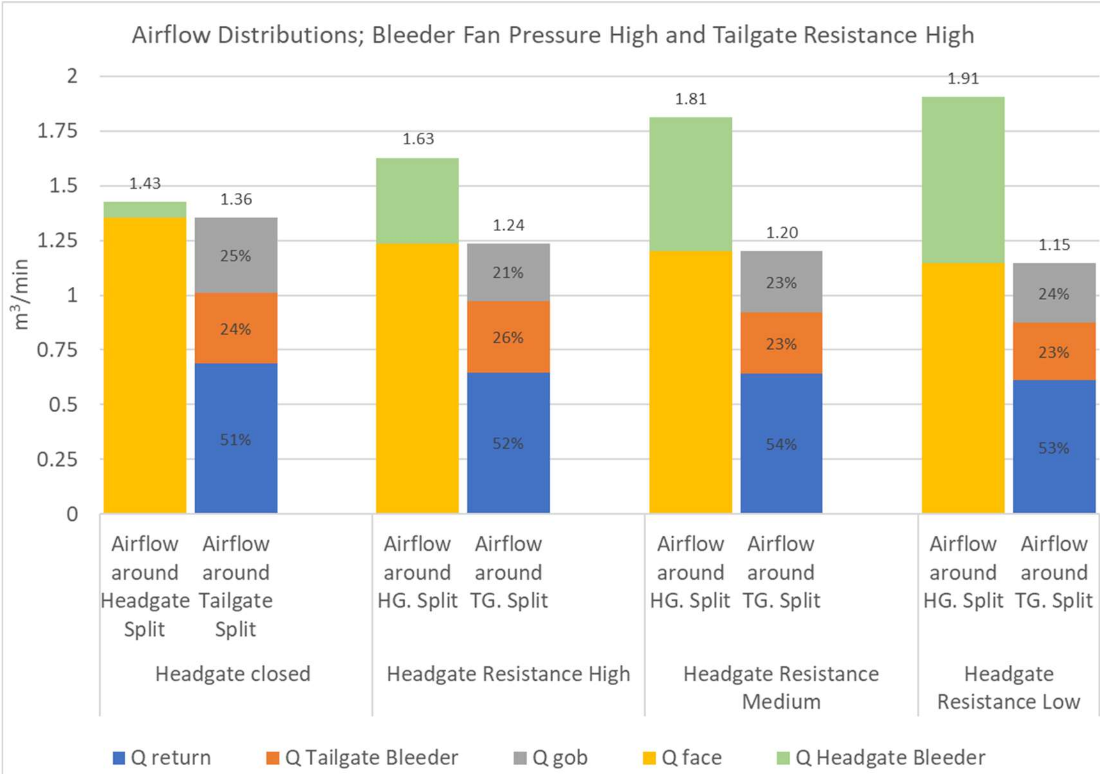

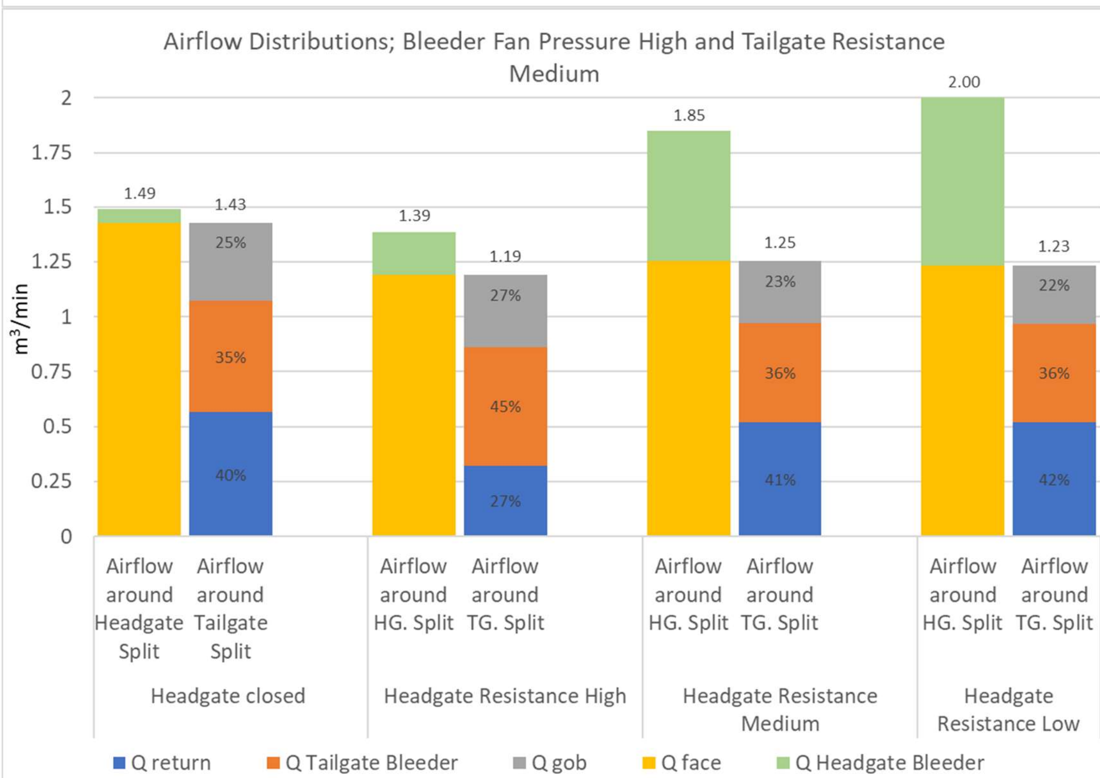

Figure 4-12 Ideal ventilation effectiveness simulations cont.

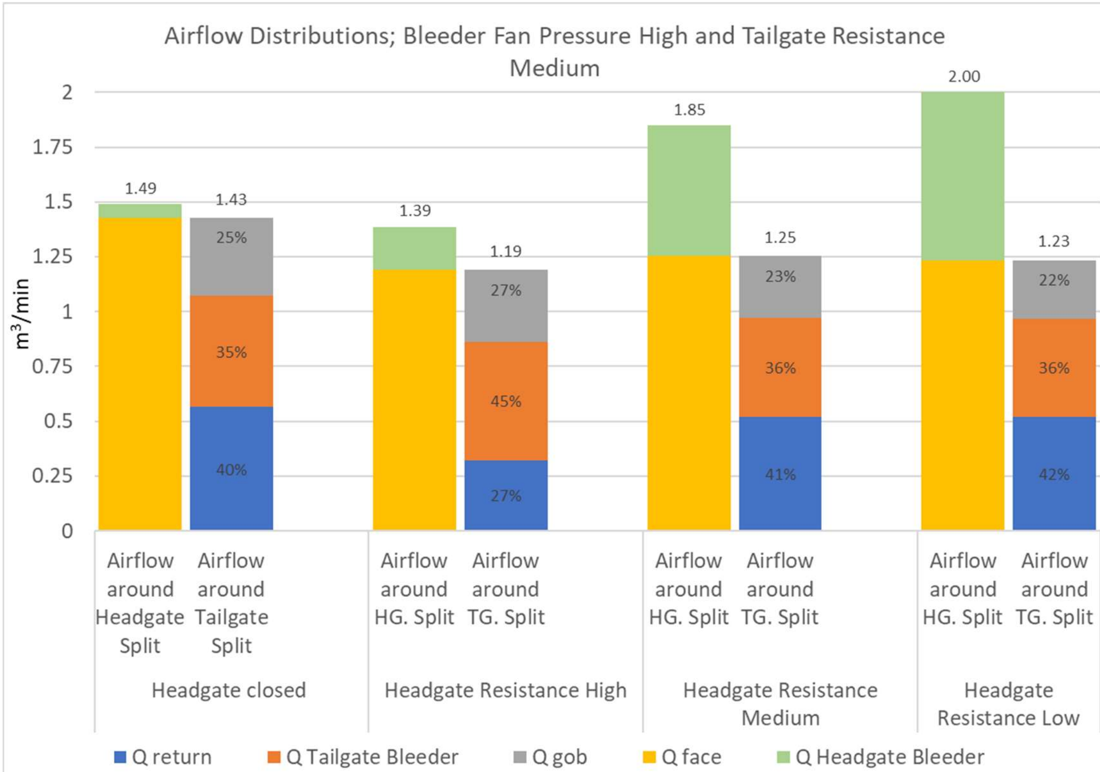

Figure 4-13 Ideal ventilation effectiveness simulations cont.

There are several interesting concepts that are prevalent throughout each of the simulations tested, all of which follow the pattern throughout the variable testing. For succinctness only one example will be given to defend each statement made, however, in almost all cases multiple examples could have been given. This discussion will only be for the ideal cases while the leakage case discussion will happen in a further section.

First, the simulations are confirmed to be calibrated and prove the general ventilation equations used for the prediction of airflow. For example, looking at Figure 4-10 and 4-11 with the headgate closed at a medium bleeder fan pressure as the tailgate resister is opened the total airflow seen through the model increases: 1.40 m^3/min, 1.46 m^3/min, 1.47 m^3/min; this is what one would expect given it correlates to a lower overall resistance. Furthermore, As the tailgate resister is opened it is expected that more air to travel through the resister towards the bleeder outlet due to the lowered resistance. This can be seen by the increase in the orange bar in the same example going from 21%, 31%, 39%. Trends like this can be seen for each of the three variables throughout each of the 36 simulations. Therefore, the mesh size seems to be small enough to capture the details needed to follow the ventilation patterns, and the computational model is further confirmed.

The next point of interest will be about the ventilation effectiveness of the simulations. The highest overall system resistance should occur when the bleeder fan pressure is lowest and resistances are highest, this would be Figure 4-8. Then subsequently the lowest overall system resistance will occur when the bleeder fan pressure is highest and resistances are the lowest which occurs in Figure 4-13. While these should be the two extremes in all 36 simulations very little differences can be seen between the air entering the face (yellow bar and subsequently the 2nd bar in each simulation). Excluding the headgate closed simulations, which is a unique case, the overall airflow entering the face is quite similar, 1.24 m^3/min, 1.20 m^3/min, 1.16 m^3/min in Figure 4-8 and 1.19 m^3/min, 1.25 m^3/min,1.23 m^3/min in Figure 4-13. These are quite similar values and given the drastic differences in resistances is quite interesting. Looking next at the overall airflow entering the panel Figure 4-8 shows 1.57 m^3/min, 1.74 m^3/min, 1.80 m^3/min while Figure 4-13 shows 1.39 m^3/min, 1.85 m^3/min, 2.00 m^3/min. These correlate to ventilation effectiveness ratios of 79.0%, 69.0%, 64.4% for Figure 4-8 and 85.6%, 67.6%, and 61.5% for Figure 4-13**.** Since almost all the airflow is being directed to the face in the high resistance simulations it is expected that the ventilation effectiveness starts at a higher percentage. But it can also be seen in the high resistance cases that once a resistance starts to be lowered the effectiveness drops more substantially because of the higher pressure seen through the entries. Both of these trends can be seen starting with the 79.0% and 85.6% ventilation effectiveness radios. Then the quicker drop off quicker can be seen by the trends between 85.6%-61.5% and 79%-64.4%. This revelation is invaluable because it could provide a mine operator with the information needed to make an informed decision about how to alter the critical ventilation parameters around the longwall face to achieve a more efficient system both in terms of airflow quantity across the face and in terms of dollars wasted on that airflow quantity that isn't going to dilute the face airway.

Another trend that can be seen in almost all the simulates is as the headgate resister is opened less airflow travels through the gob. Take Figure 4-9 for example, when the headgate is closed or at a high resistance about 25% (0.35m^3/min) of the face airflow travels back through the gob. However, when the headgate resistance is medium or low that drops down to about 20% (0.25m^3/min). This is likely due to there being more air in the headgate around the gob, the pressures are more normalized to the face thus 'pulling' less air from the face through the gob. While these simulations don't include geometries for the shields or AFC it is still worth noting the predisposition for the air to 'naturally' take. This pattern can be seen throughout the simulations and carries great importance in the field. Mines with a history or high chance of Spon Com always want to limit the amount of air traveling through gob as this only leads to more oxidation and greater gob temperatures. Running simulations like these under specific conditions for a mine site will undoubtedly help the operator optimize their airflow distribution around the face and gob.

Finally, the effect of closing the tailgate bleeder will be discussed. In Figure 4-12 the top bar graph shows a high tailgate resister setting while the bottom graph shows a medium setting. Looking at the second bar in each simulation it can be seen that the gob airflow is very minimally affected by this variable. Since the tailgate resister is after the gob face interaction it is not a big surprise however, it is still worth noting that the tailgate change does drastically affects the split between the bleeder airway and the return airway. Again, this is what was expected from altering this variable; nonetheless, Operators still could run simulations around this variable to optimize the airflow split. From chapter 2 it was shown that one of the most cited citations was bleeder methane concentration levels. Altering this variable around a specific mines geometries and boundary conditions could be the key to understanding exactly how much air is going through the tailgate resister. Then subsequently, the capability of the airflow to dilute a specific amount of methane gas.

Next the figures from the stopping leakage scenarios will be examined.

4.2.1.3 Stopping Leakage

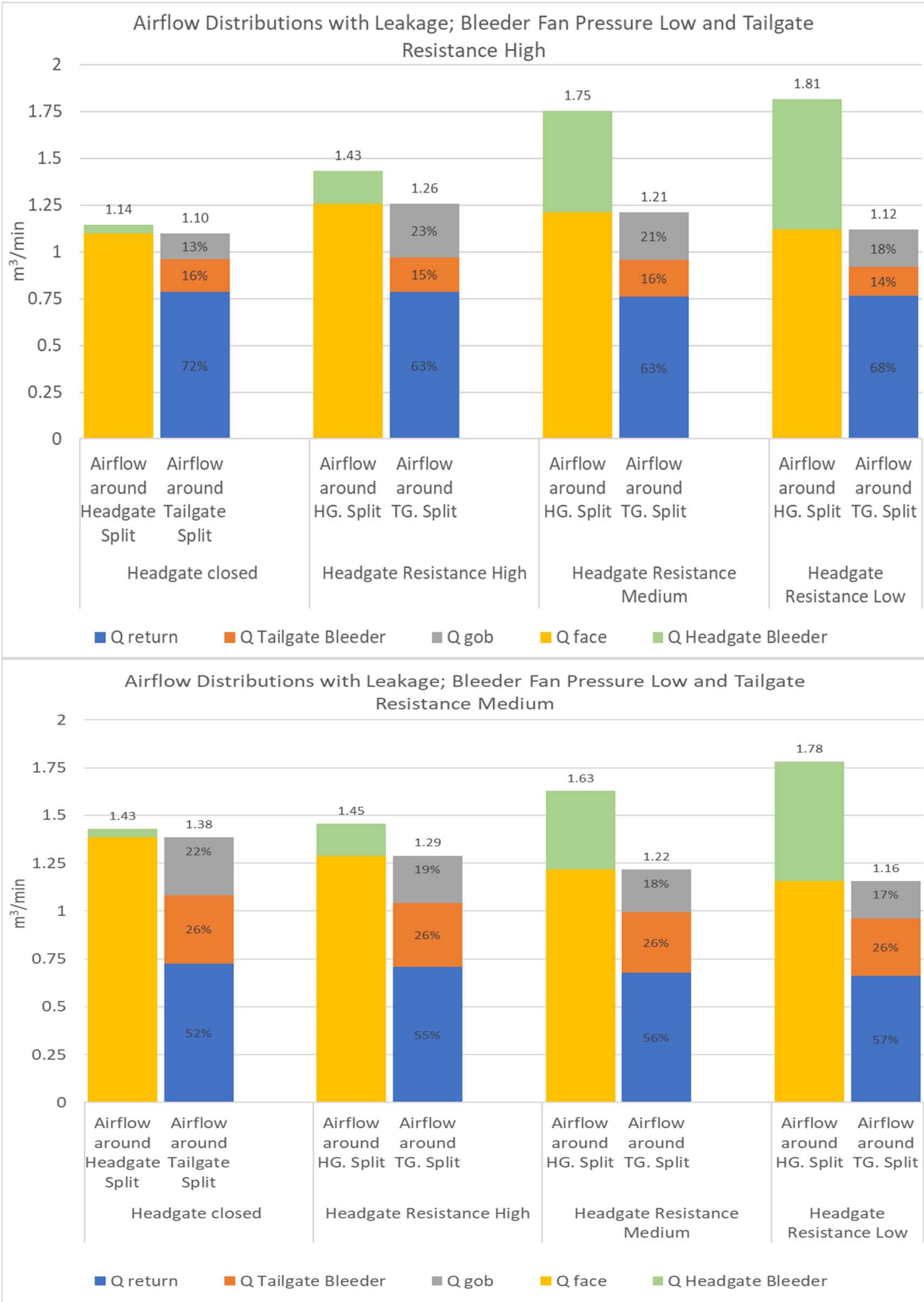

Figure 4-14 Stopping leakage ventilation effectiveness simulations

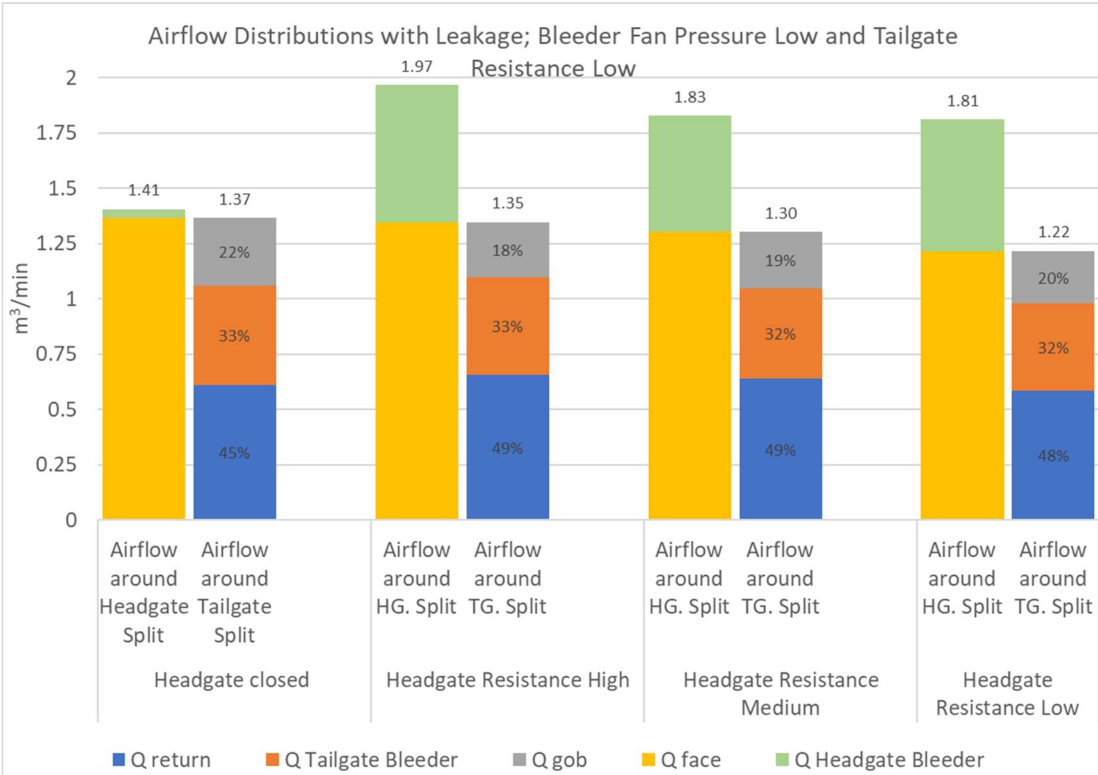

Figure 4-15 Stopping leakage ventilation effectiveness simulations cont.

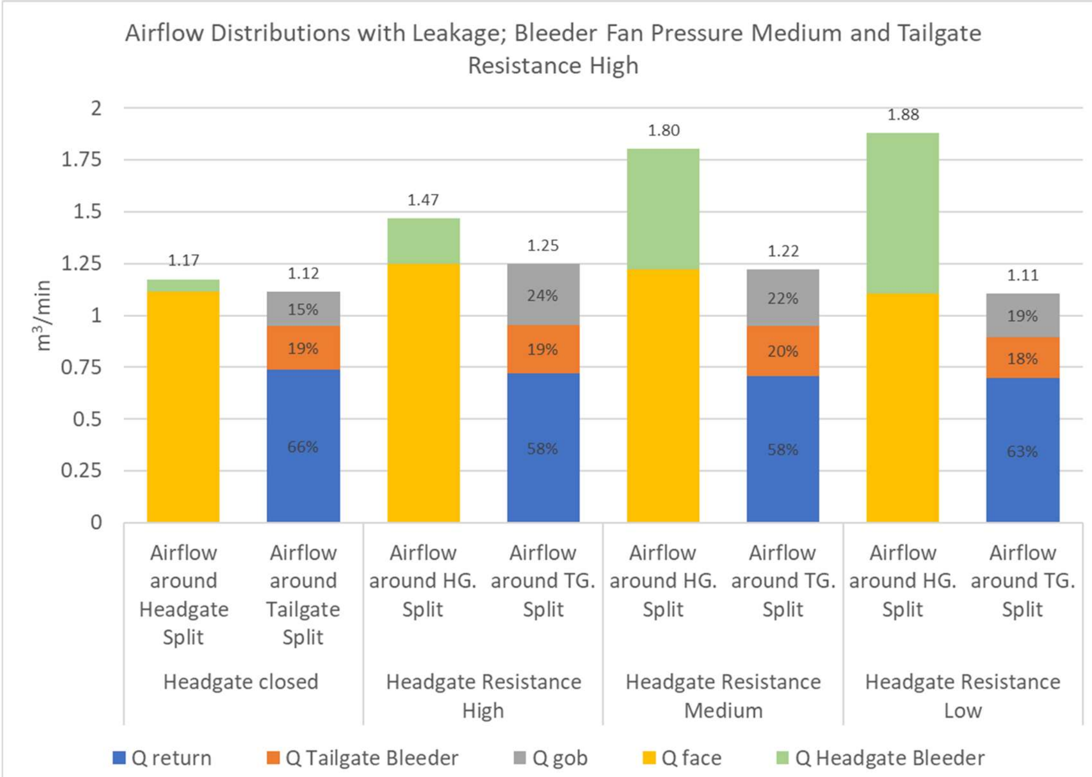

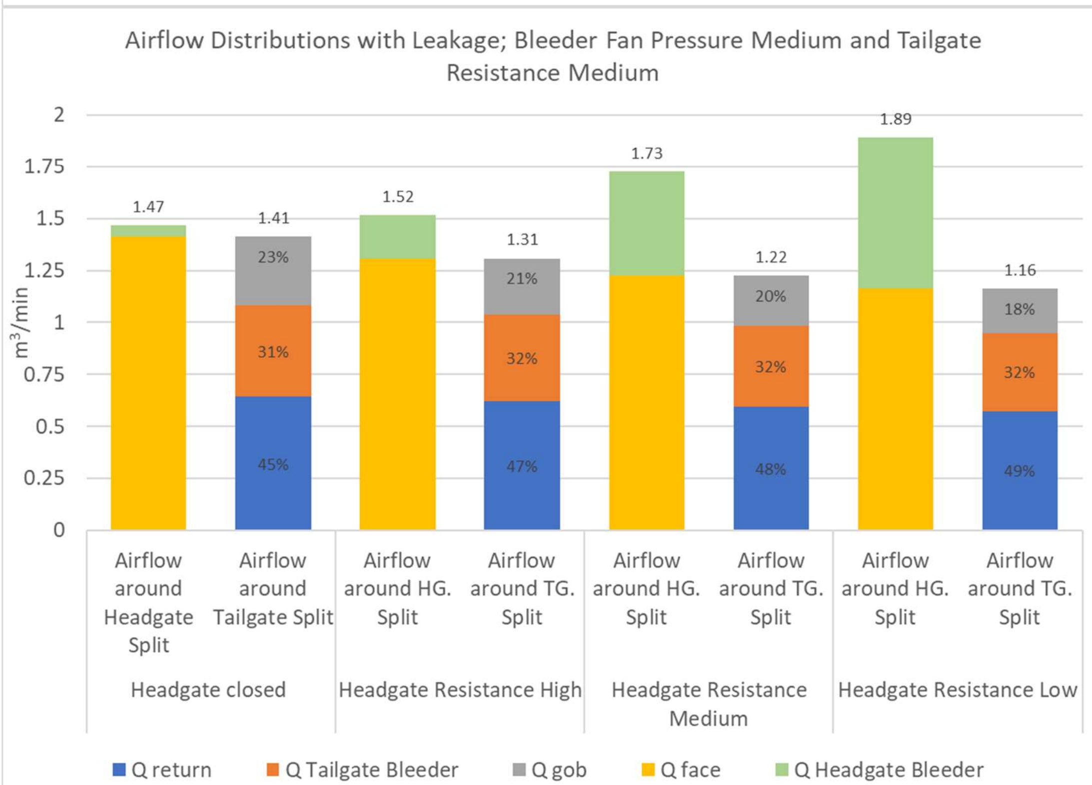

Figure 4-16 Stopping leakage ventilation effectiveness simulations cont.

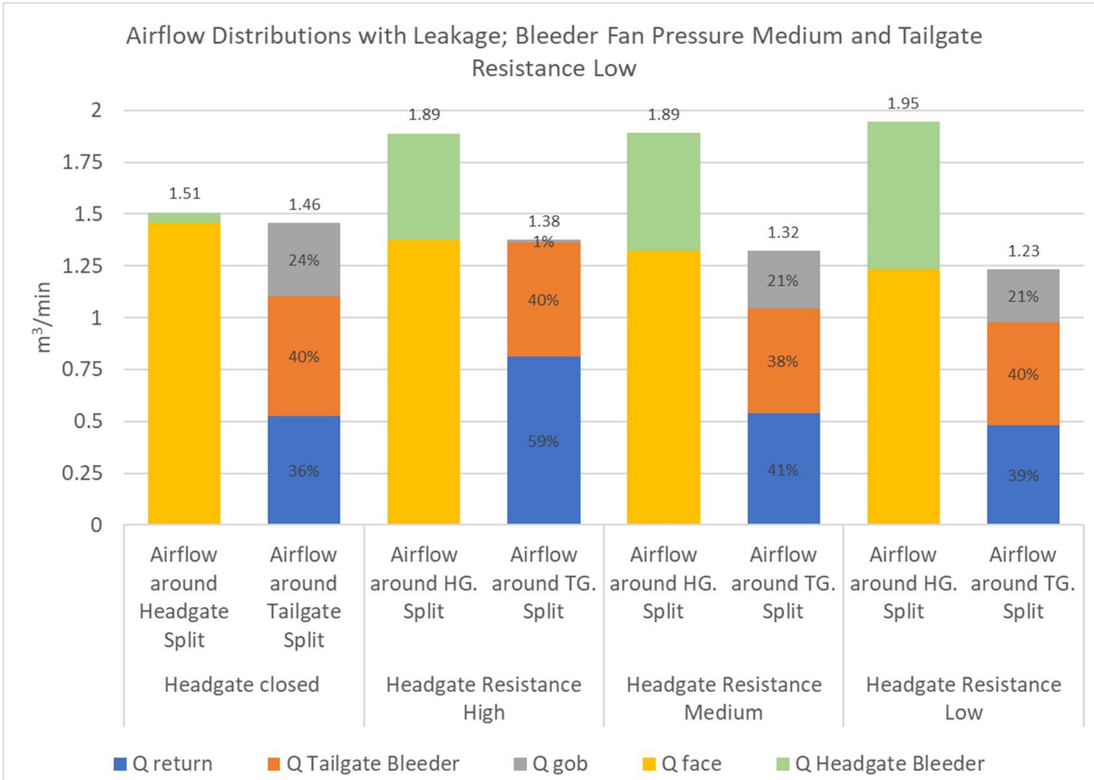

Figure 4-17 Stopping leakage ventilation effectiveness simulations cont.

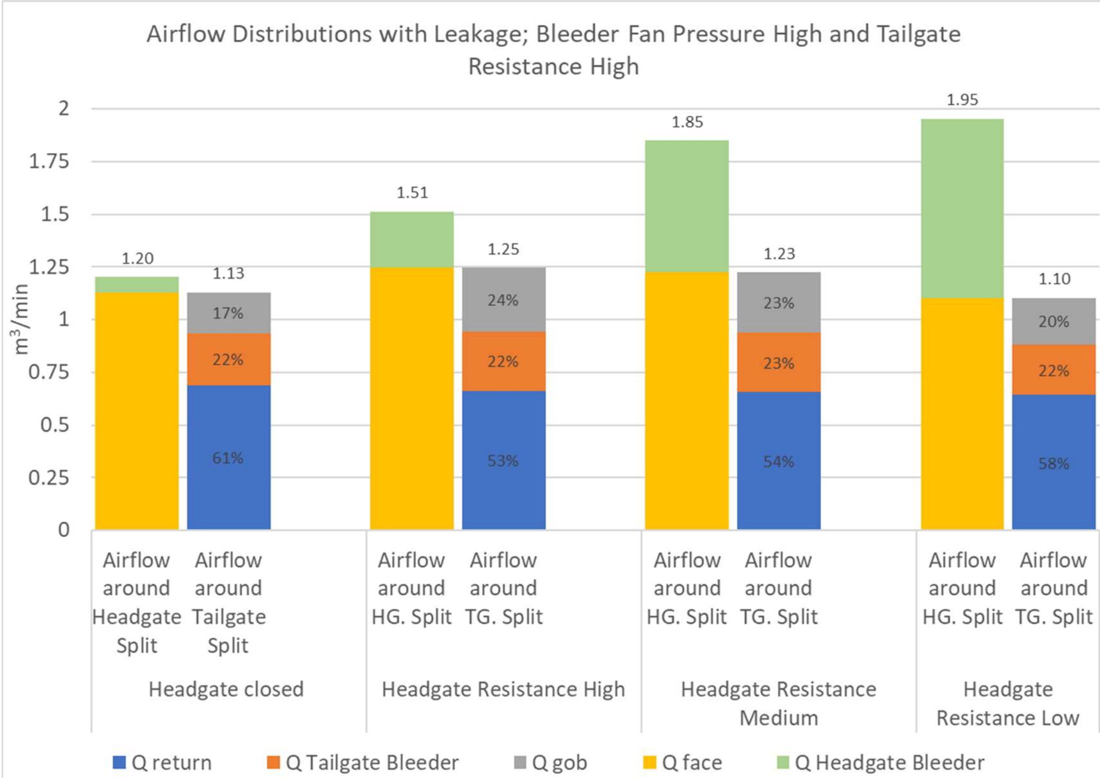

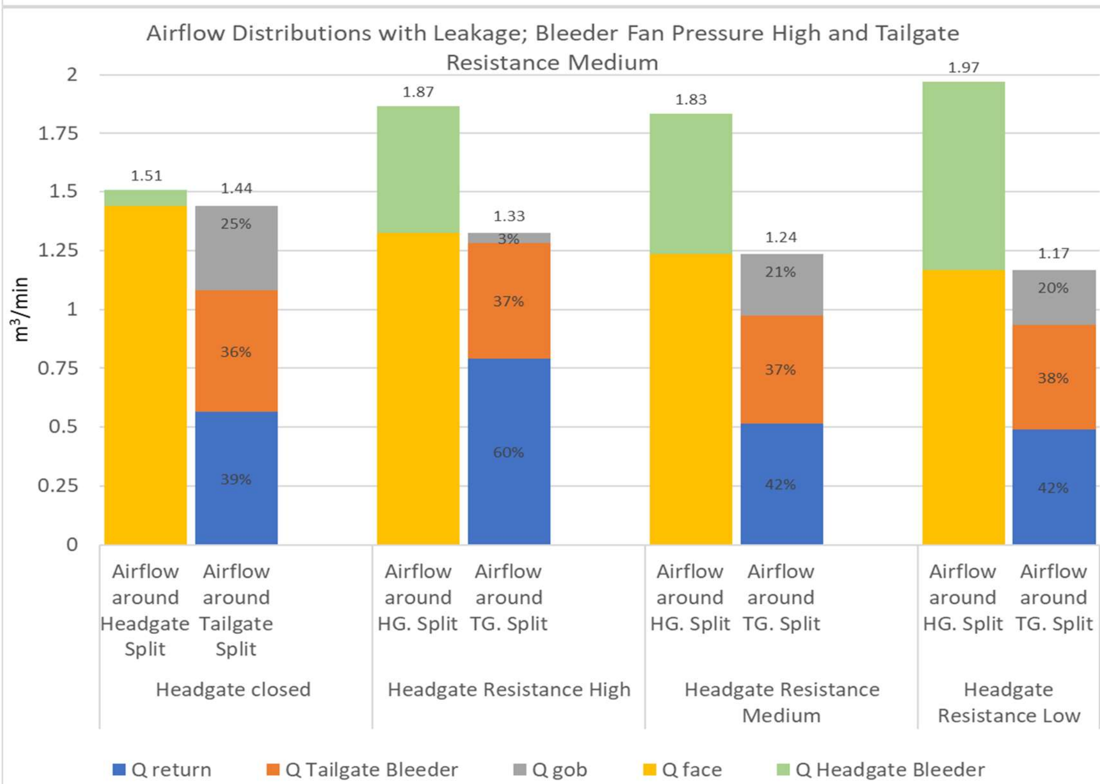

Figure 4-18 Stopping Leakage ventilation effectiveness simulations cont.

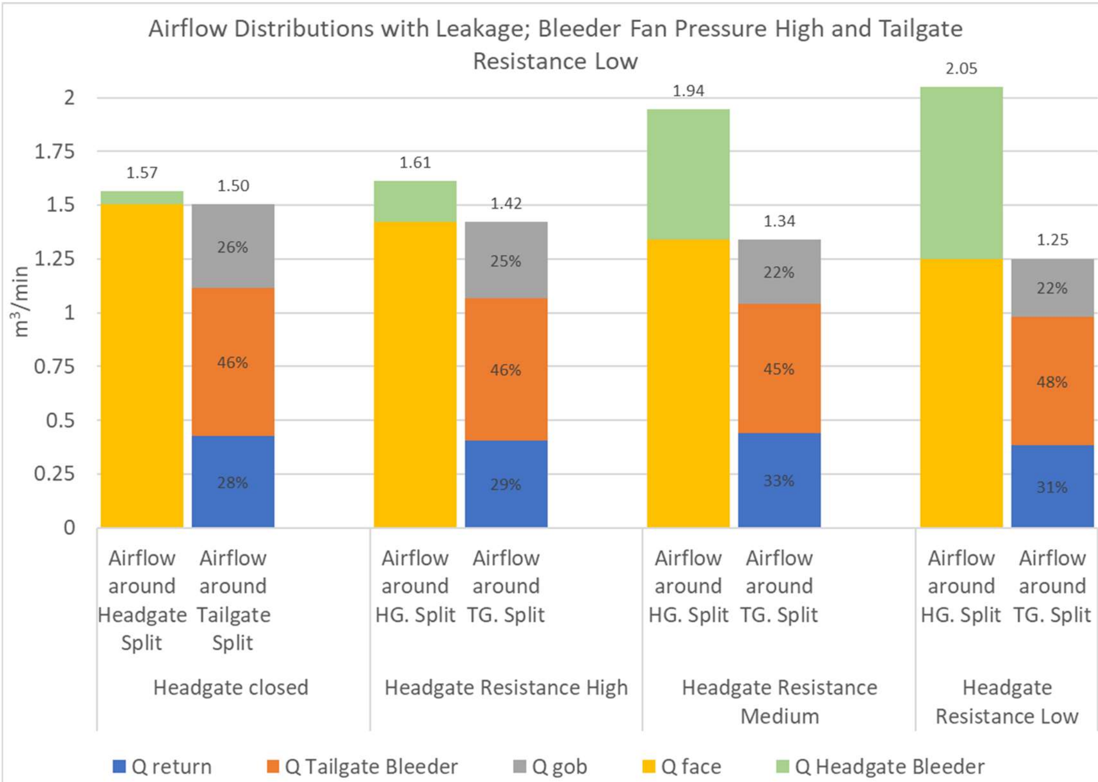

Figure 4-19 Stopping leakage ventilation effectiveness simulations cont.

A comprehensive discussion about the changes in airflow around face was given in the previous section when no stopping leakage was present. Therefore, this section will focus on the differences between the simulations with stopping leakage and those without.

Firstly, since some leakage will be seen across the mains it is expected that lower airflow quantities will reach the face since the same resister and bleeder fan settings will be used. This proved to be true, throughout Figures 4-14 - 4-19 the airflow reaching the headgate split is lower than that of Figures 4-8 - 4-13 with minimal exception. It is also encouraging to see the overall trend of airflow around the face and gob follows extremely closely to that of simulations without leakage. Meaning stopping leakages in the mains has a minimal effect on airflow spits in and around the face. This is most likely due to the relatively large distance between the leakage points and the face; this allows the airflow quantity and pressures throughout the entries to balance before entering the headgate split. Although these simulations didn't change the face location on the panel it would be interesting to determine if the face would ever be at a positioned in the panel where leakages in the main would affect that airflow patterns across the face.

However, when the tailgate resistance is at the lowest, such as in Figures 4-15, 4-17**,** and the bottom graph of Figure 4-18, there is a change in the trend of airflow. When considering leakage, the highest airflow going to the panel is seen when the headage resistance is highest, but when no leakage was account for the highest airflow is seen when the headgate resistance is lowest. This pattern shows up regardless of the bleeder fan pressure which means given a specific amount of stopping leakage there is a clear headgate and tailgate resistance set up that yields the highest face airflow. That having been said, in general, when stopping leakage is introduced lower amounts of air reaches the face compared to no stopping leakage. Furthermore, like the no leakage scenarios, the same pattern of increased airflow to the face is seen throughout the figures as the headgate and tailgate resistance gets lowered; and continuing with the bleeder fan pressures, similar headgate airflow splits can be seen between the two cases. The results clearly show that specific resister settings can yield higher airflow about the face but given the simplistic nature of the stopping leakage and idealized simulation conditions this phenomenon may be exaggerated in the results.

4.2.2 Initial face advancement study (gob moves with the face)

In total 14 different face advancement scenarios were tested allowing the face to progress until the full cycle can be repeated. Three major patterns can be derived from these 13 simulations which will be shown in this section, the remaining 11 simulations will not be shown as they show extremely similar patterns. The three face locations shown are a 3 cm, 7 cm, and 11 cm face advance; since the model is to 1/100 scale this correlates to a 3, 7, 11-meter face advancement. These simulations were completed with methane emission across the coal face as well as throughout the gob.

Through each of the velocity profiles in Figure 4-20 little air mixing can be seen, the flow through the face is extremely streamlined. While this could be attributed to no objects across the face it is worth noting that the air isn't evenly distributed. It can be seen though each of the three cases a layer near the gob of greatly decreased airflow that accounts for about 10%-20% of the cross-sectional area; Figure 4-21 shows this in greater detail with a different view. Given that the entire face airway in empty it would be reasonable to assume a degree of even airflow though0out the cross section. However, Figure 4-21 clearly shows a segregation in airflow, the highest velocity being near the face with the lowest being near the gob. Furthermore, it can be seen that the methane entering from the face is not being properly diluted by the airstream as the majority of the airflow has no methane concentration. This shows that over half of the airstream is not being used to dilute the methane. Proving that even with the proper quantity of airflow reaching the face it is not guaranteed to properly handle methane concentrations.

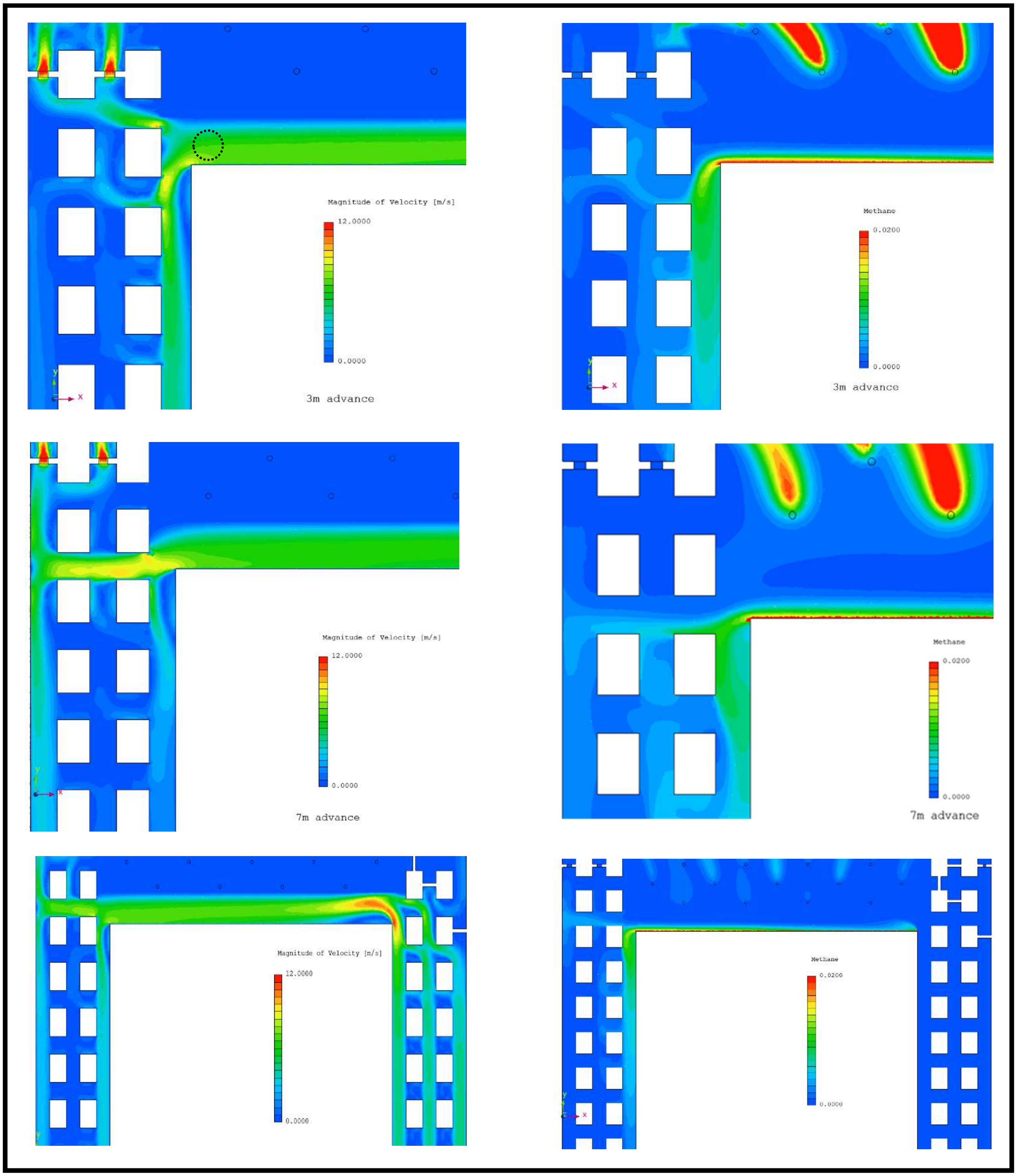

Figure 4-20 Velocity and methane concentrations at 3m, 7m, and 11m face advancement

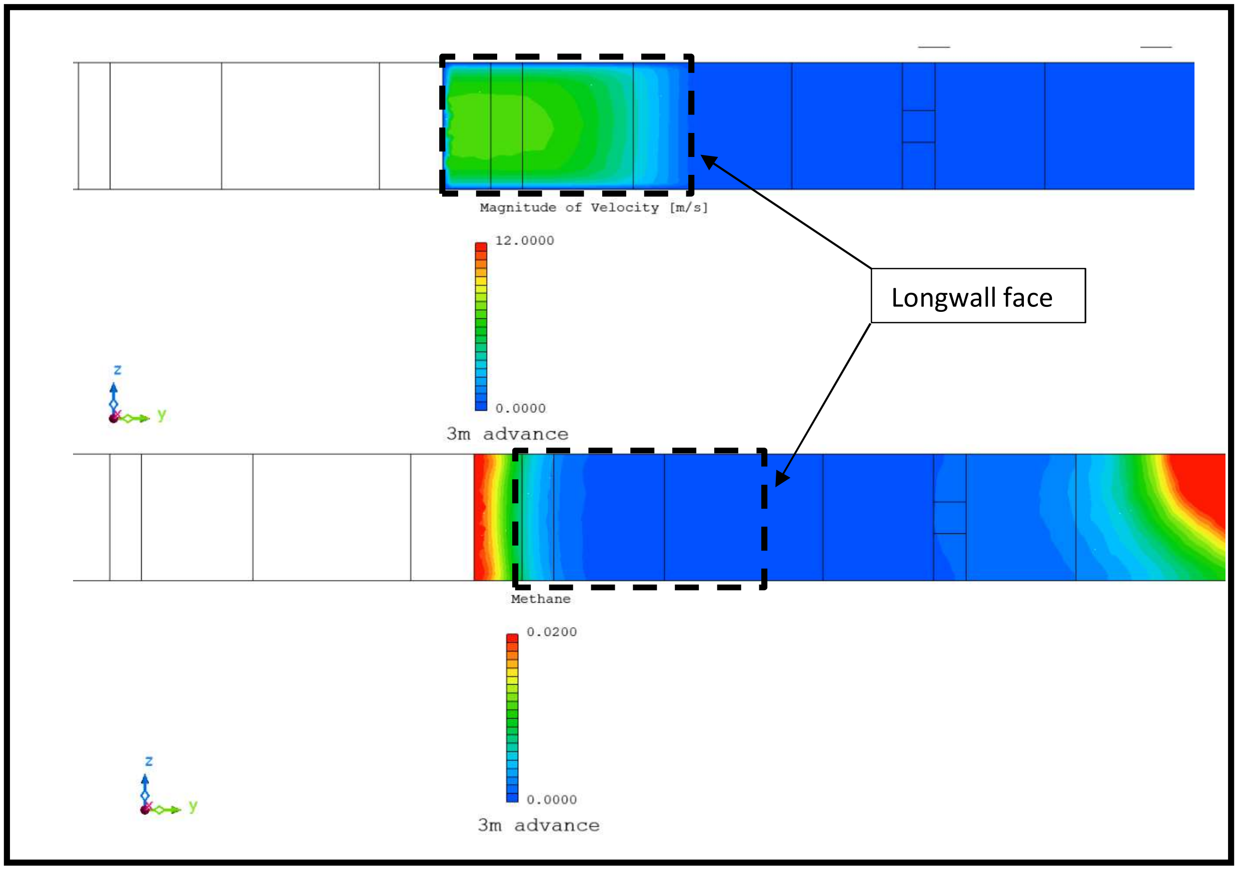

Figure 4-21 Velocity and methane concentration shown across the cross-sectional area of the face

Three major patterns can be seen from the 14 different scenarios tested and they come down to location of the face relative to the pillars in the tailgate. The first can be seen in the 11m advance case when the face airflow is lined up rather nicely with the cross cut in the pillars, even with the addition of a curtain in the cross cut it can be noted that almost all of the methane entering from the face travels outby towards the return, while a significant amount of air goes towards the bleeder. This mismatch of methane to air can cause unpredictably high concentrations in the return which renders the bleeder system ineffective.

Secondly the 3m advance case is when the airflow across the face lines up with the pillar and is mainly forced to the return. While a curtain, or more gob compaction then modeled can happen in the cross cut immediately behind the face in the tailgate corner, it still is presumable that a portion of air will be swept out towards the bleeder though the shields as seen above the circle in Figure 4-21. This can cause a dangerous area around the middle of the face where the air splits between the shields and the return airway; this is circled in the top left figure in Figure 4-20. Since the methane in the simulation was not properly diluted across face, some methane buildup can be seen in the tailgate corner around the pillars near the split. Even if the buildup is small, over time areas with little flow will accumulate methane. Each simulation did not consider time therefore any small build up can lead to larger problems very quickly.

Lastly the 7m advance scenario where the face airflow aligns with the pillar and starts to align with the forward crosscut. High velocities can be seen in the crosscut, much like the 11m advance the airflow splits clearly in 2 places; in the first and third entry of the tailgate. This correlates to high turbulence because airflow is being split into two paths both of which require a bend. Because of this the corresponding methane figure shows a more distributed pattern throughout all the entries instead of just one or two like the 3m and 11m advance.

Then when the face aligns with a cross cut the location of the airflow split moves from the third tailgate entry to the first tailgate entry as seen in the 7- and 11-meter advance case. However, this has little value as curtains may or may not be used my mine operators across the crosscut to force the airflow split in the first tailgate entry.

4.2.3 Improving Longwall Geometry

Results of the baseline simulation can be seen in Figures 4-22 through Figure 4-25. Velocity profiles across the face and tailgate corner can be seen in Figure 4-22 and 4-23 while Figure 4-24 and 4-25 show the methane concentrations along the face and tailgate corner. No comments will be made about the simulations at this time as these are simply run to provide a baseline to compare future simulations to.

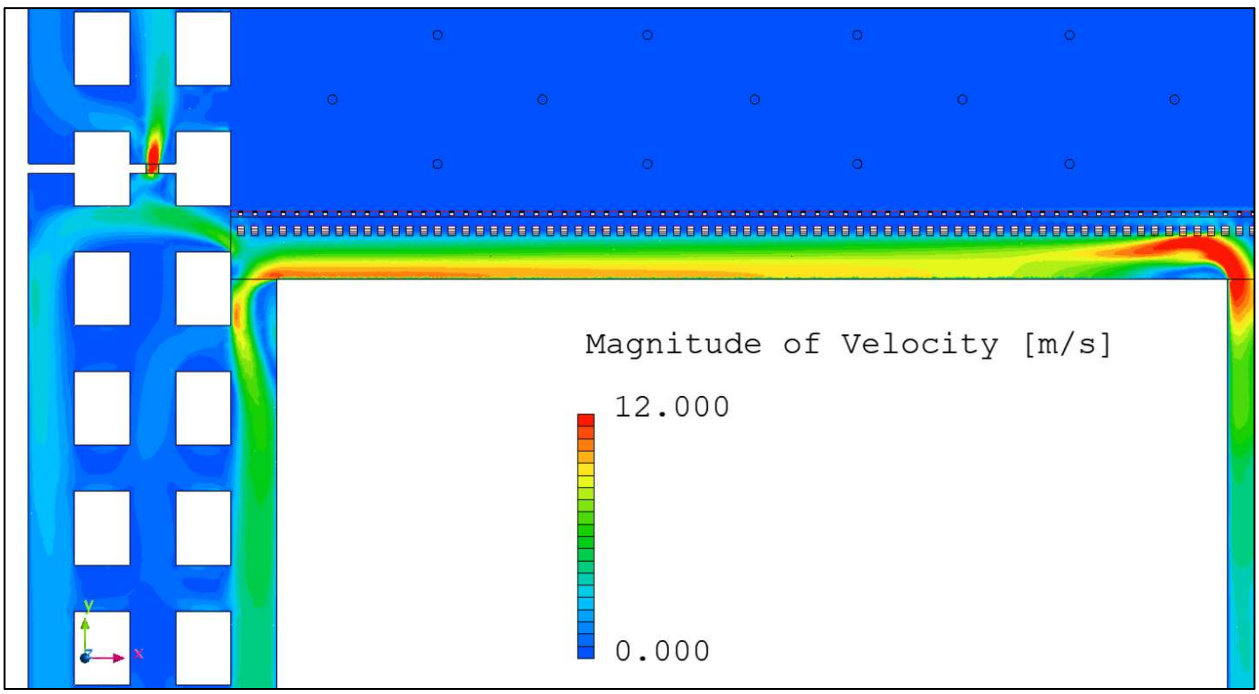

Figure 4-22 Baseline velocity across longwall face

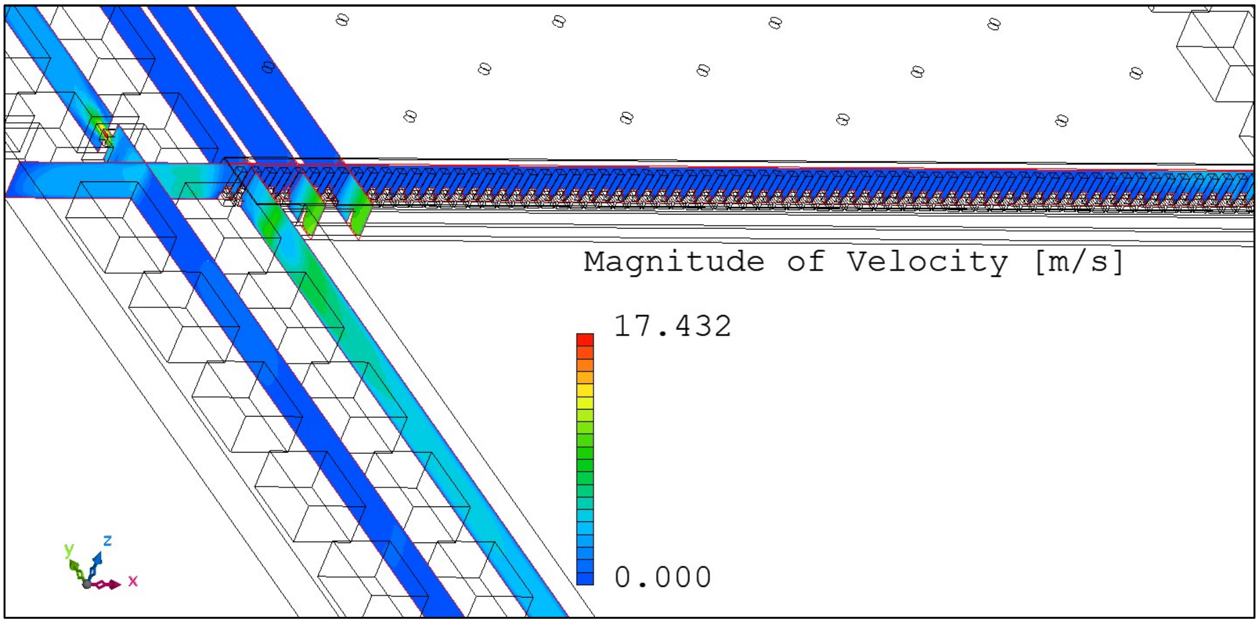

Figure 4-23 baseline velocity around tailgate corner

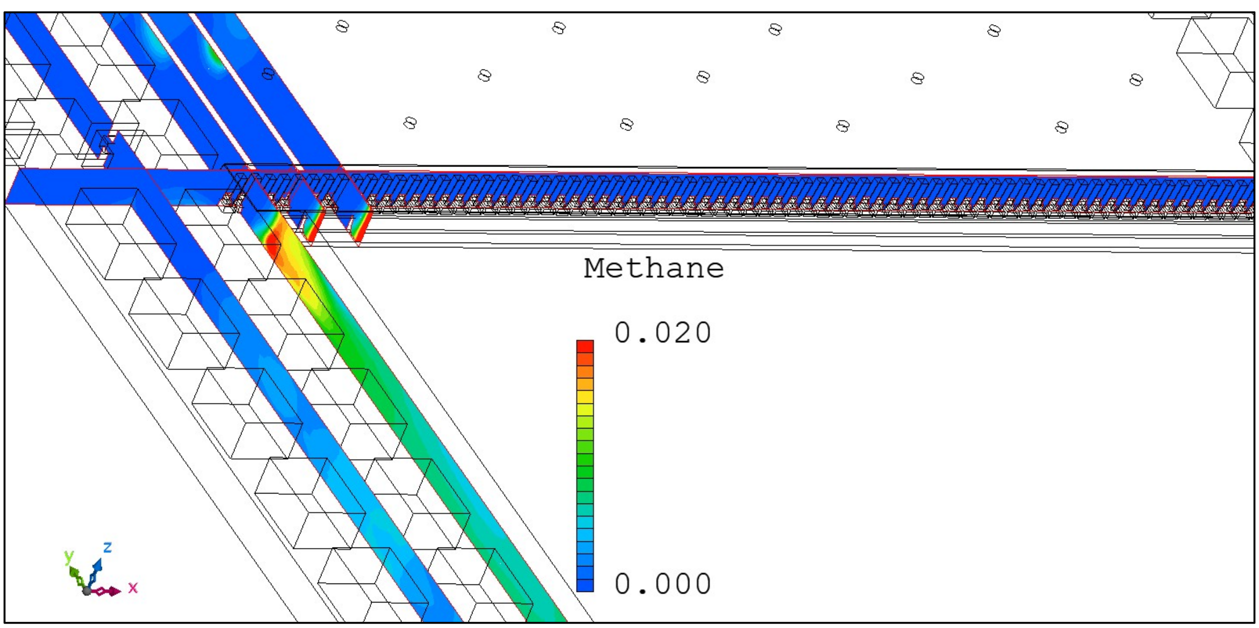

Figure 4-24 baseline methane concentration around tailgate corner

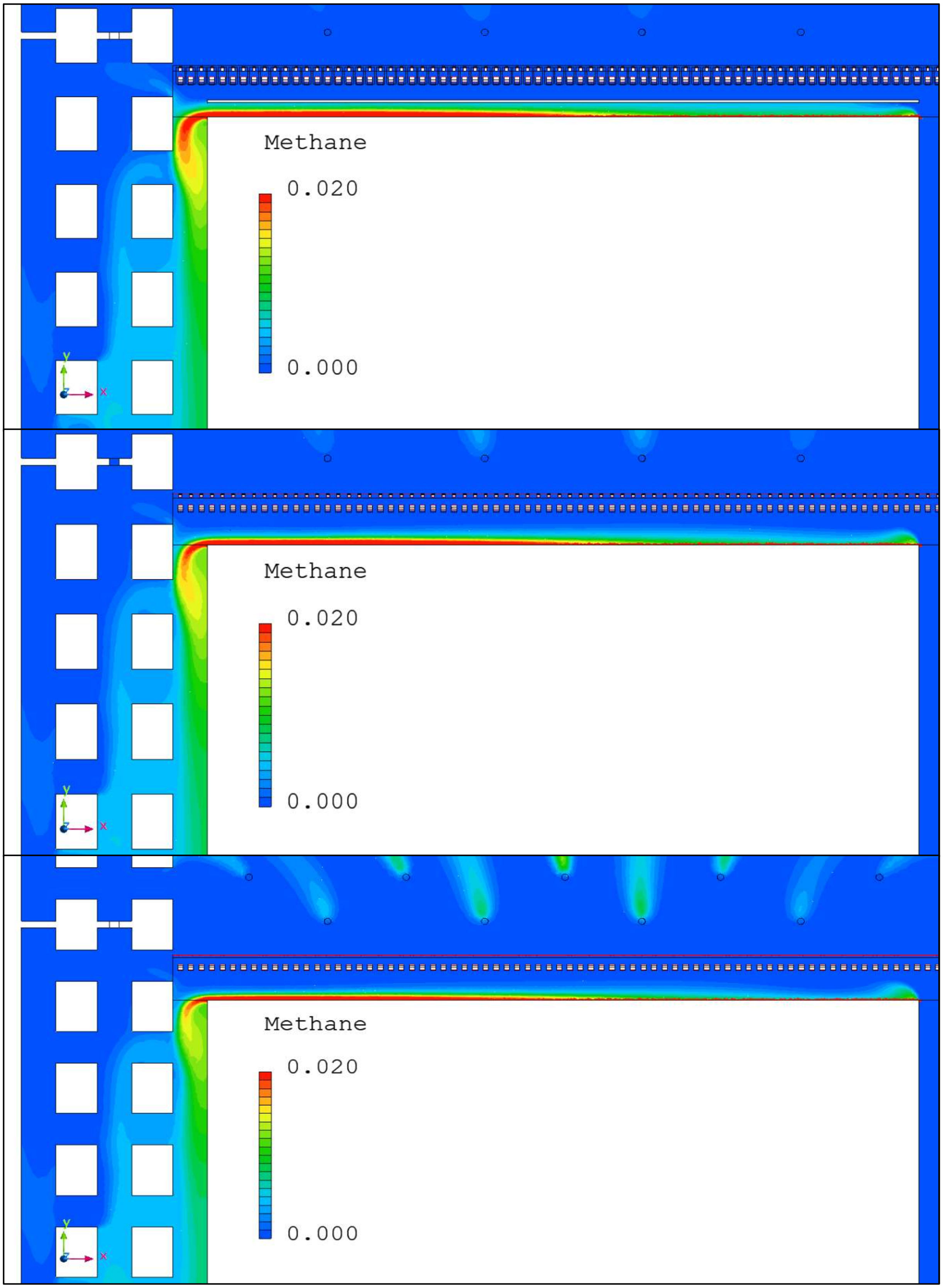

Figure 4-25 Baseline methane concentrations: top 25%, middle 50%, bottom 75% of mining height

4.2.4 Face Advancement Study

Velocity and Methane profiles for each of the three advanced face simulations can be seen in Figures 4-26 and 4-27. Looking at the velocity, as the face moves forward the velocity nearest to the face decreases. This may be the direct result of increased airflow behind the shields, however from Figure 4-28 there is very little airflow traversing around the shields area. The shields are acting as a pseudo wall and allow very little air to pass through them; this was also noted in the initial baseline results. Only the initial airflow around the headgate corner has the required pressure or airflow direction to pass through the shields seen in Figure 4-28; furthermore, when looking down the face the remaining airflow seems to be more evenly distributed.

This even distribution of air could either be the air behind the shields returning to the face area, or just a general more even distribution of air as the face advances. Looking at Figure 4-26 the velocity behind the shields for the 1cm advance case decreases as it flows across the face. This provides the context to conclude that initially the air will flow through the shields when flowing around the headgate corner, then will slowly leak either to the gob or back into the face. It is not until the last few shields where the airflow from the face begins to flow through the shields towards the gob. This is shown by the red arrow in the top figure of Figure 4-26, this increase in velocity can only be from air flowing back towards the gob. Similar patterns can be seen in the 2cm and 3cm advance case even if it is more difficult to see because the velocities behind the shields are higher.

Looking at the methane distribution in Figure 4-27, it was established that no or very little air passes through the shields towards the gob; therefore, the methane from the coal face follows this same pattern of not flowing back into the open area behind the shields. However, an interesting phenomenon occurs in the methane concentrations around the tailgate corner as the face advances. Even with a greater quantity of air going behind the shields and leaking back towards the gob as the face advances, the methane concentration around the tailgate corner decreases. Given that the methane influx was the same for all three cases it does not make sense for methane concentration to decrease because less air is flowing in this area. However, this higher volume of air in the 1cm case seems to be more effective in evenly distributing the methane in the tailgate itself. In Figure 4-27 it can be seen in the 1cm advance case the tailgate concentration ends a little under 1% (light blue) while the 3cm advance case keeps the concentration higher showing a little over 1% concentration (green). Therefore, it is reasonable to conclude that as the face advances different levels of mixing occurs solely from the face location relative to the gob and resisters.

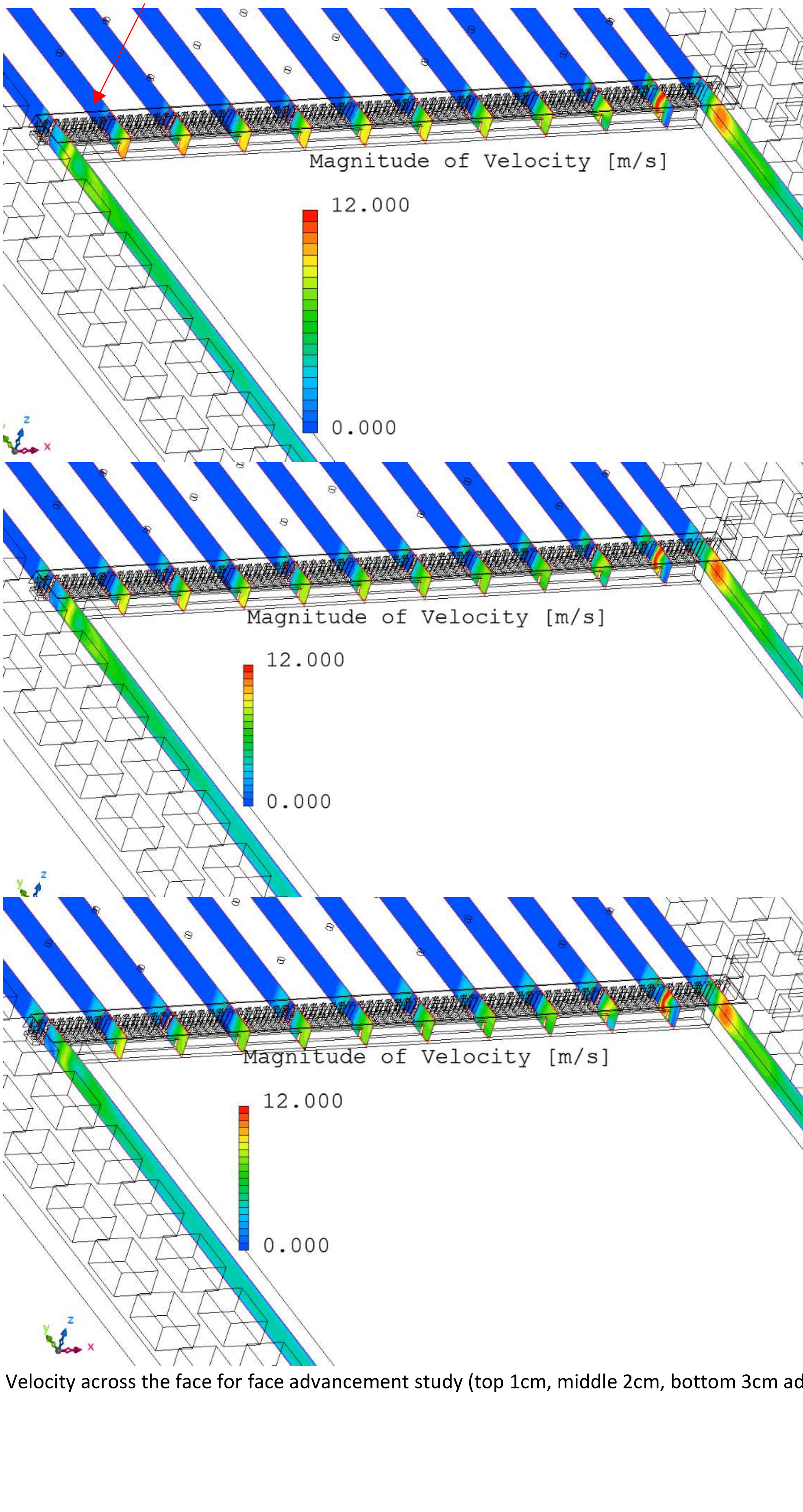

Figure 4-26 Velocity across the face for face advancement study (top 1cm, middle 2cm, bottom 3cm advance)

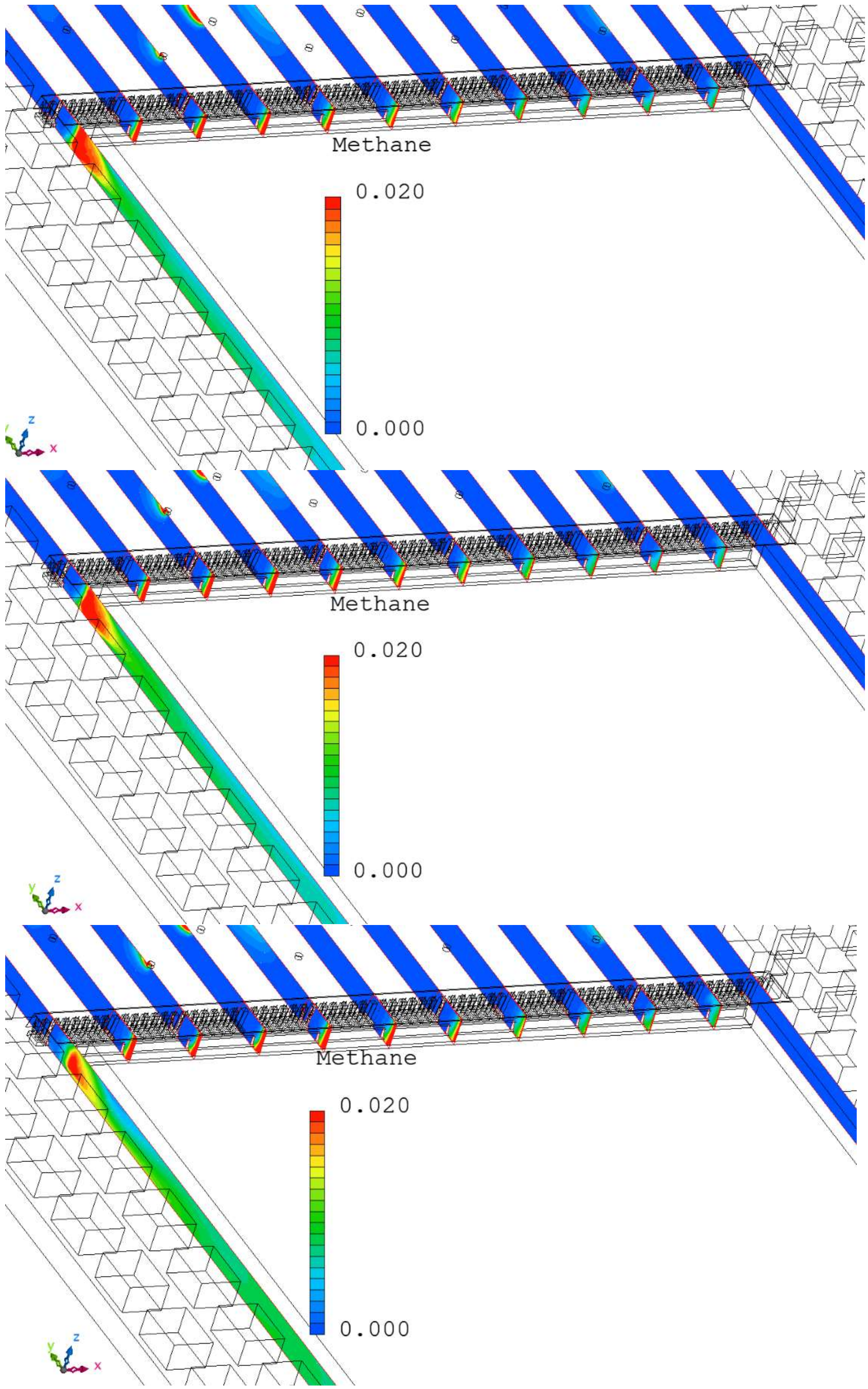

Figure 4-27 Methane across the face for face advancement study (top 1cm, middle 2cm, bottom 3cm advance)

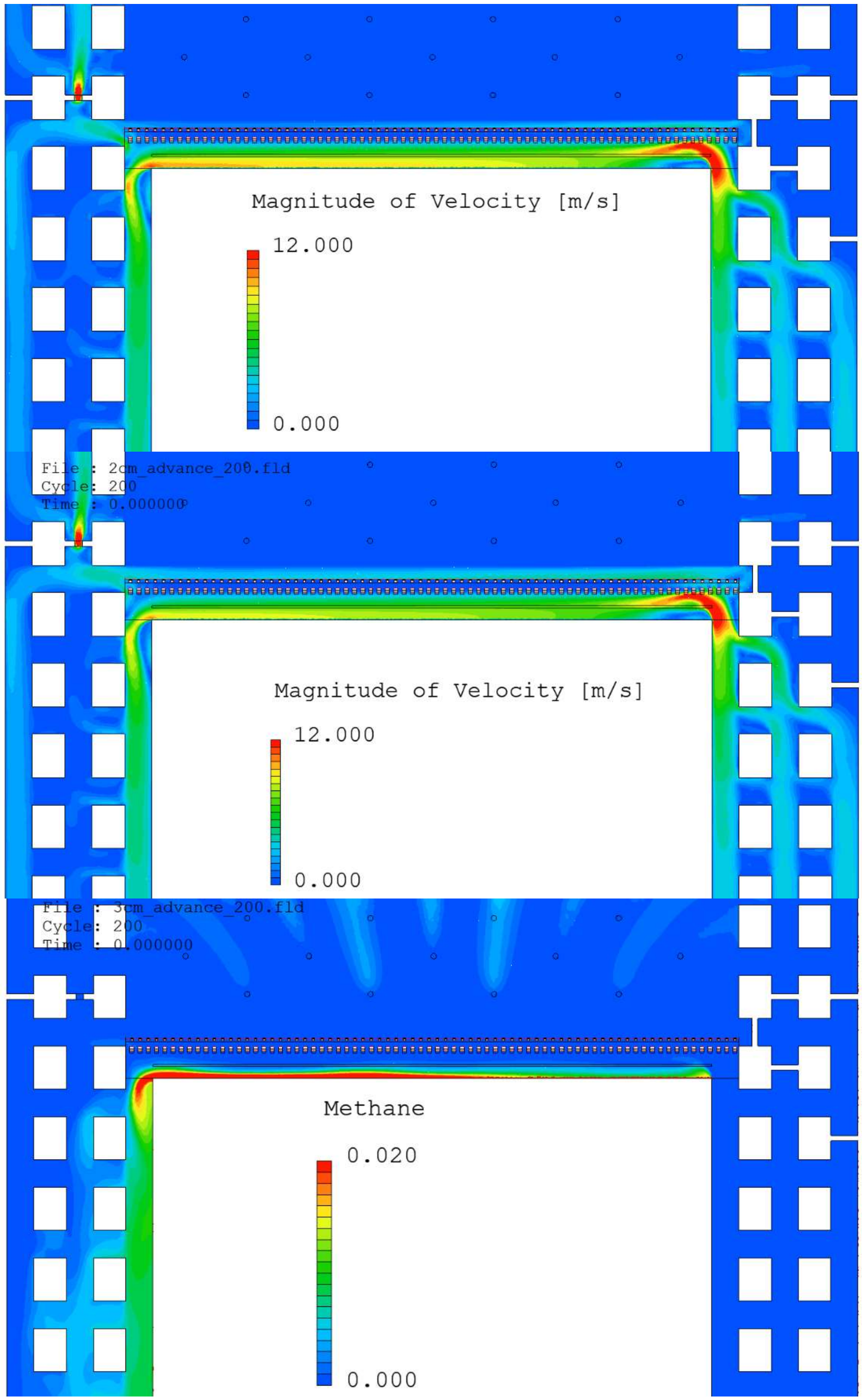

Figure 4-28 Methane across the face for face advancement study (top 1cm, middle 2cm, bottom 3cm advance)

4.2.5 Roof Fall Simulations

4.2.5.1 Without Face Improvements (standard)

Four roof fall scenarios were simulated in total with 3 unique locations and the fourth simulation being a combination of all 3 locations. Firstly, the baseline ventilation about the face and tailgate corner are shown in Figures 4-29 and 4-30 these are the same figures from the improvement to geometry section but are shown again here for convenience

Roof fall one which is shown in Figures 4-31 and 4-32 show a roof fall in the entry closest to the panel. Since in the baseline most of the airflow and methane traverse this entryway it would be expected to see substantial differences in airflow patterns. However, significant changes in airflow patterns are difficult to detect. Nevertheless, the methane concentration tells a different story; significant differences in methane concentrations can be seen mainly after the roof fall which indicated lower turbulence and/or velocity in the airflow. While the initial plume (before the roof fall) seems to be lower in concentration the concentration after and around the roof fall is much higher. Also, this entry clearly holds this higher methane concentration much longer then the baseline simulations did. Comparing Figures 4-30 and 3-32**,** Figure 3-32 does not dissipate the high methane concentration into the other entries leaving a high concentration for a significant length. It will eventually distribute amongst the other entries but at a much later time compared to the baseline; most likely due to the lower velocity due to the roof failure. Another concerning point is the recirculation happening in the middle entry. Two to three cross cuts outby the face a recirculation airflow pattern can be seen in Figure 4-32; a small amount of methane leaves the third entry with the roof fall and traveling up the middle entry towards the tailgate bleeder. Because very little airflow will initially go towards the other entries the negative pressure of the bleeder to obtain its air from further down the tailgate which holds a significant amount of methane. Over time this recirculation can cause a dangerous buildup of methane and could potentially be catastrophic considering the shearer will be on tailgate corner at some point.

The second roof fall scenario which is located two cross cuts outby the tailgate resister is shown in Figures 4-33 and 4-44; comparing Figure 4-30 and 4-34 it can easily be seen that the failure causes minimal interference with the methane concentration in the third entry. However, the roof failure at this position significantly effects the airflows ability to evenly distribute itself between the entries. This is shown by how streamlined the airflow is while it travels down the third entry with little mixing between entries in Figure 4-34. This is further shown in Figure 4-33 where no air velocity can be seen going down the middle entry (shown in dark blue). While this at first glance does not seem to be a big problem area that are this poorly ventilated around the face will accumulate methane and cause an explosive hazard.

Next the roof fall was moved to the first cross cut outby the tailgate resister. Surprisingly a roof fall in this location does little to hinder the flow of air through the tailgate regulator seen by comparing the velocity figures in Figures 4-29 and 4-35. Furthermore, the same trend of minimal airflow through the middle entry can be seen as in the other roof fall in the middle entry, but unlike the other case there is noticeable airflow in the middle entry. One other substantial insight is that there is some methane build up in the cross cut before the roof failure; this was expected however, looking at the bottom figure of Figure 4-36 the buildup in the cross cut doesn't provided a region above 2% methane but if time was factored in this surly would become hazardous. Given the severity of the roof failure and the location being such a critical junction between the face airflow and the tailgate bleeder this is surprising.

Finally, the results from the fourth case where all roof fall location were tested can be seen in Figures 4-37 and 4-38. Methane build up and recirculation can clearly be seen in the third entry and the cross cut by the face. Compared to the baseline significant amounts of area can be seen as over 2% methane which is not surprising given the vast amount of cross-sectional area taken up by the roof failures. Methane recirculation can also be seen in the top of the entryways in figure 4-38. This scenario is the worst-case scenario among all 4 tested and clearly shows lows velocities and high methane concentration throughout.

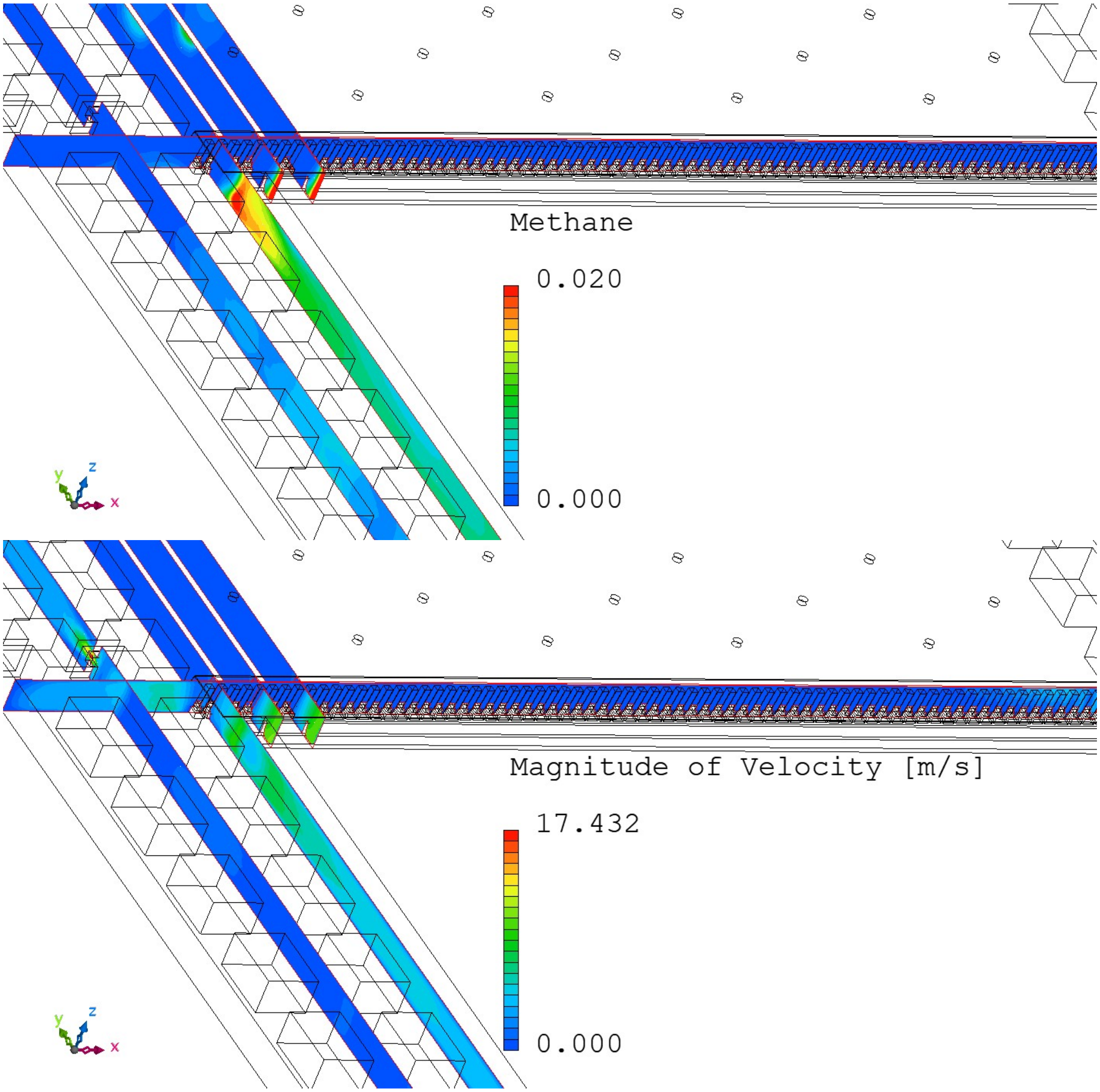

Figure 4-29 Baseline velocity and methane concentrations around tailgate corner

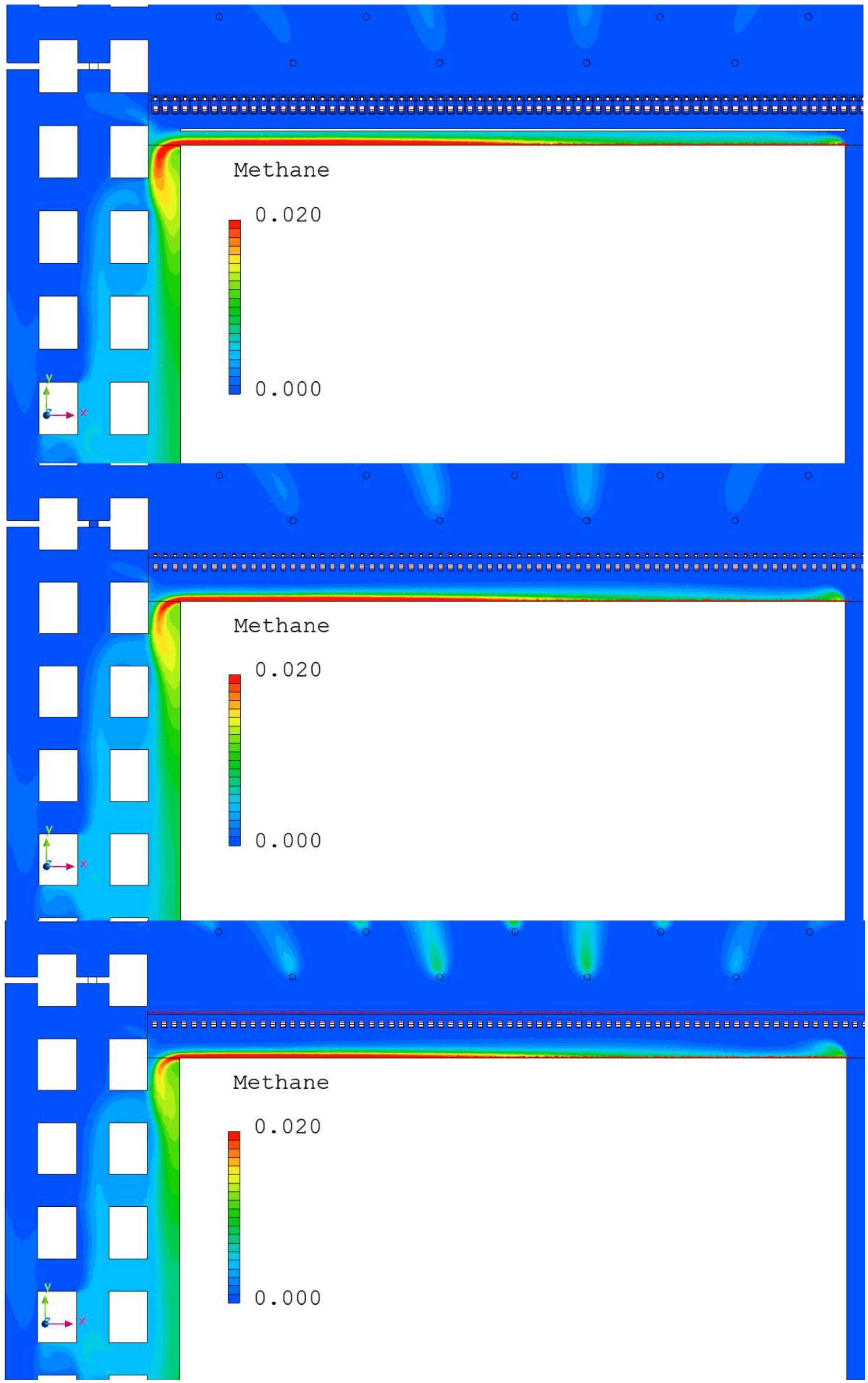

Figure 4-30 Baseline methane concentrations: top 25%, middle 50%, bottom 75% of mining height

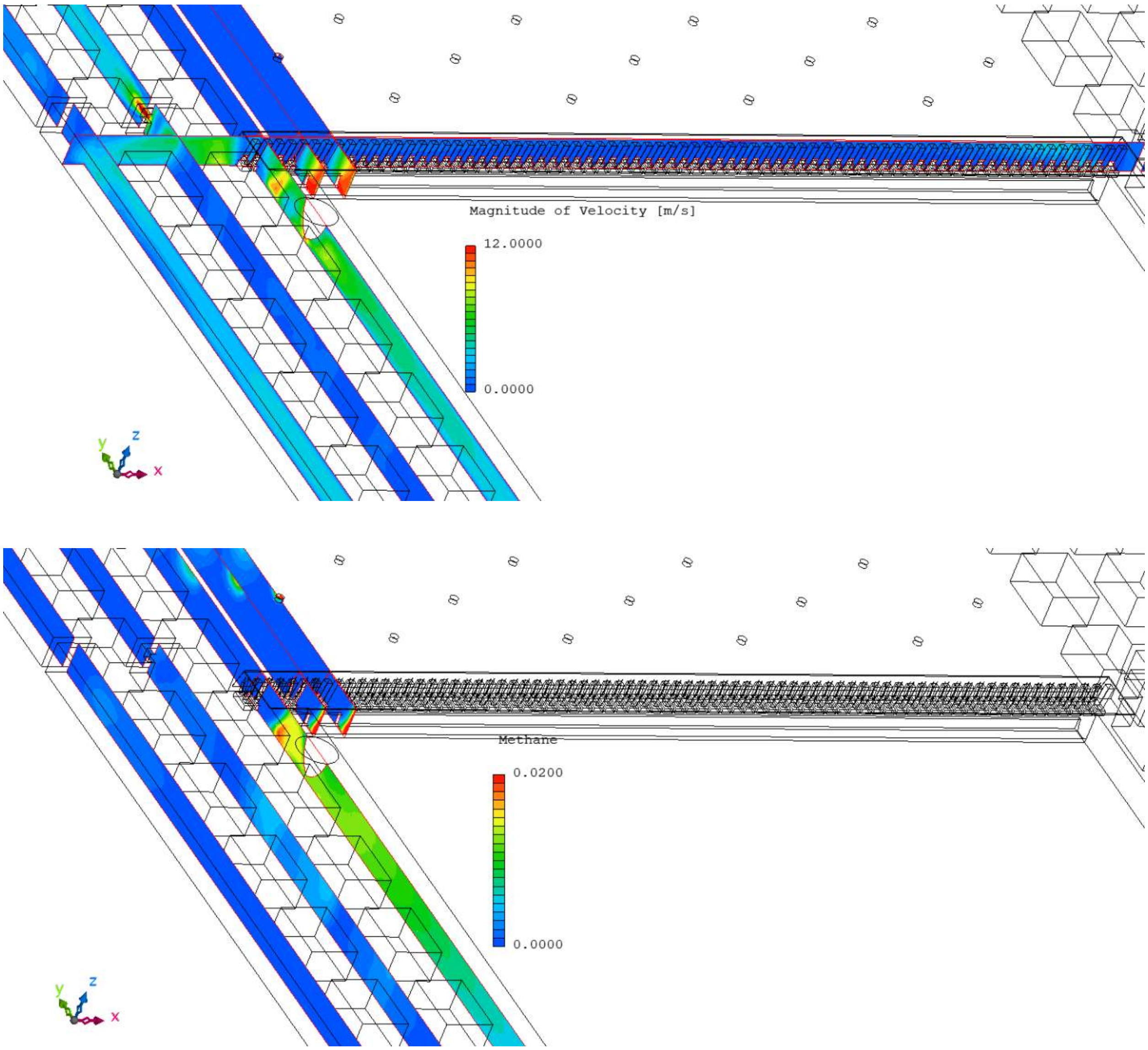

Figure 4-31 Velocity and methane concentrations around tailgate corner for RF1

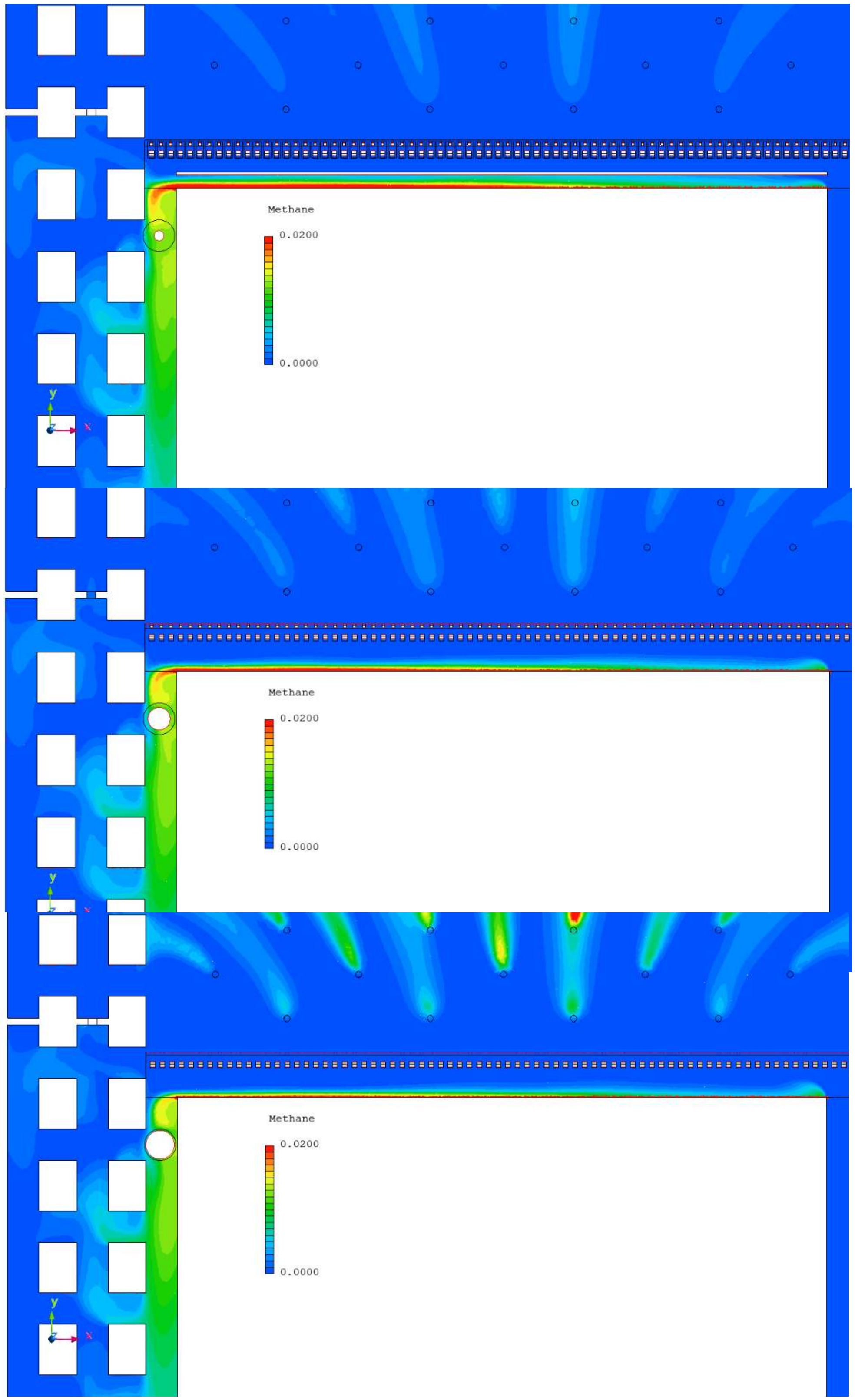

Figure 4-32 Methane concentrations: top 25%, middle 50%, bottom 75% of mining height for RF1

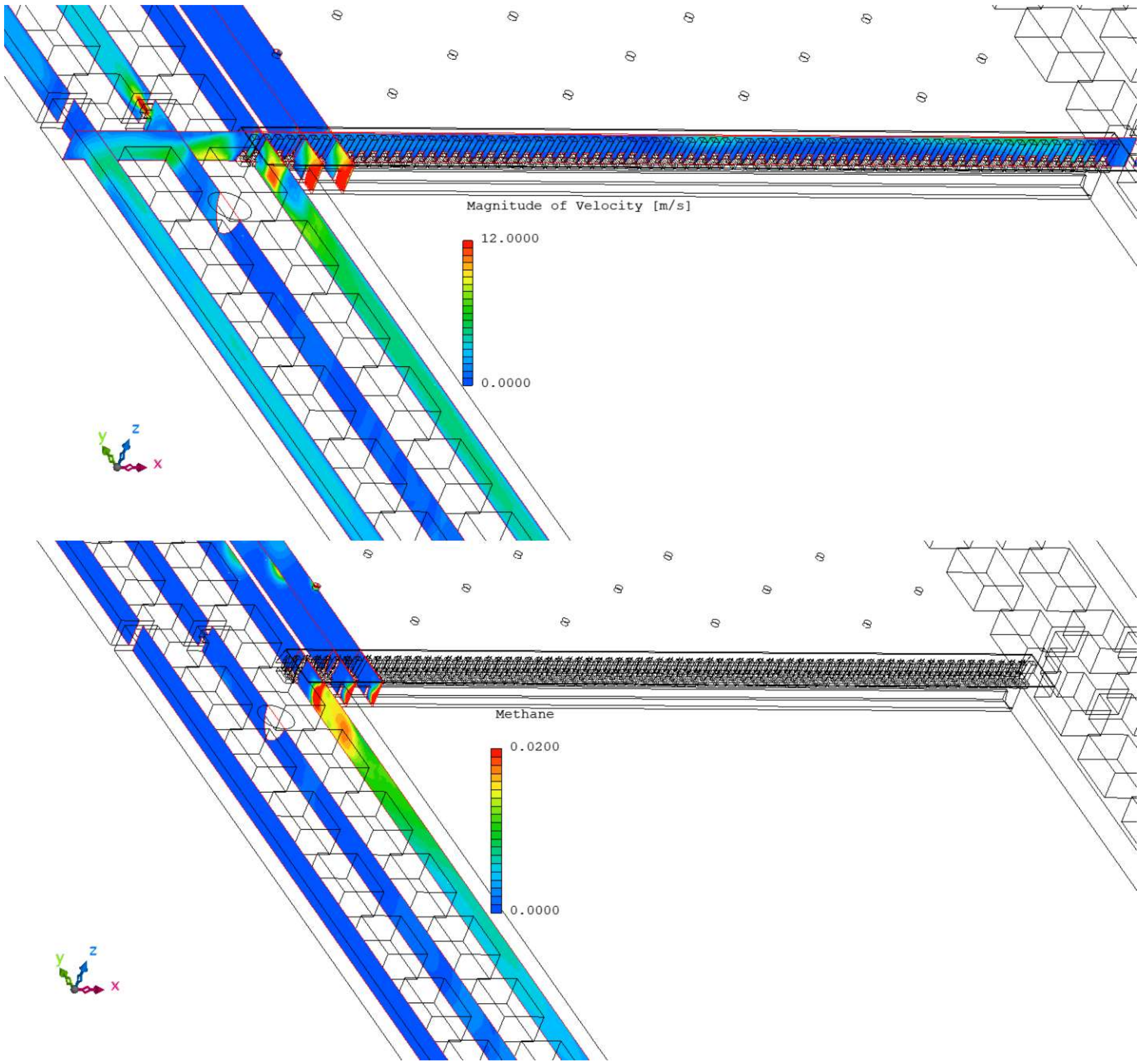

Figure 4-33 Velocity and methane concentrations around tailgate corner for RF2

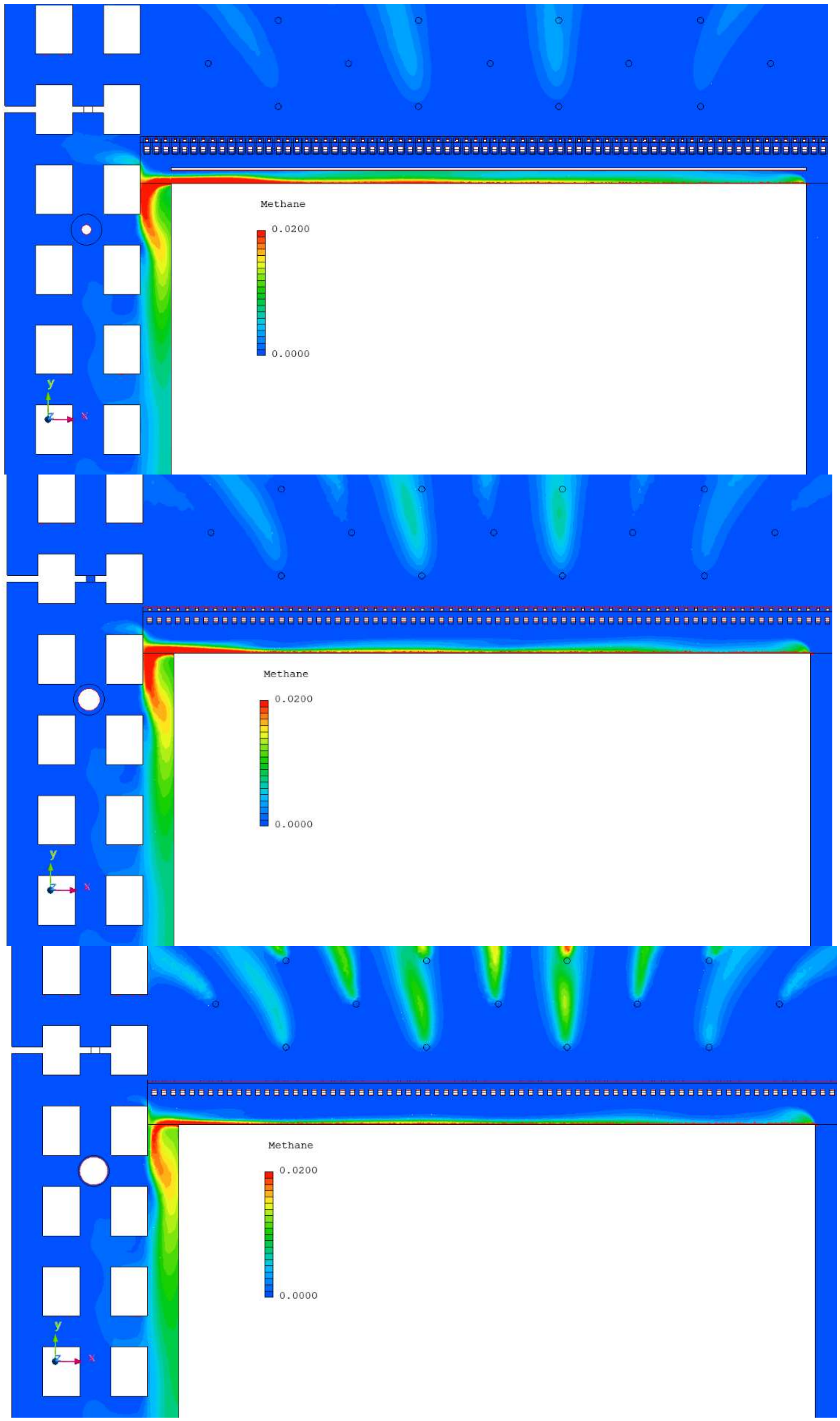

Figure 4-34 Methane concentrations: top 25%, middle 50%, bottom 75% of mining height for RF2

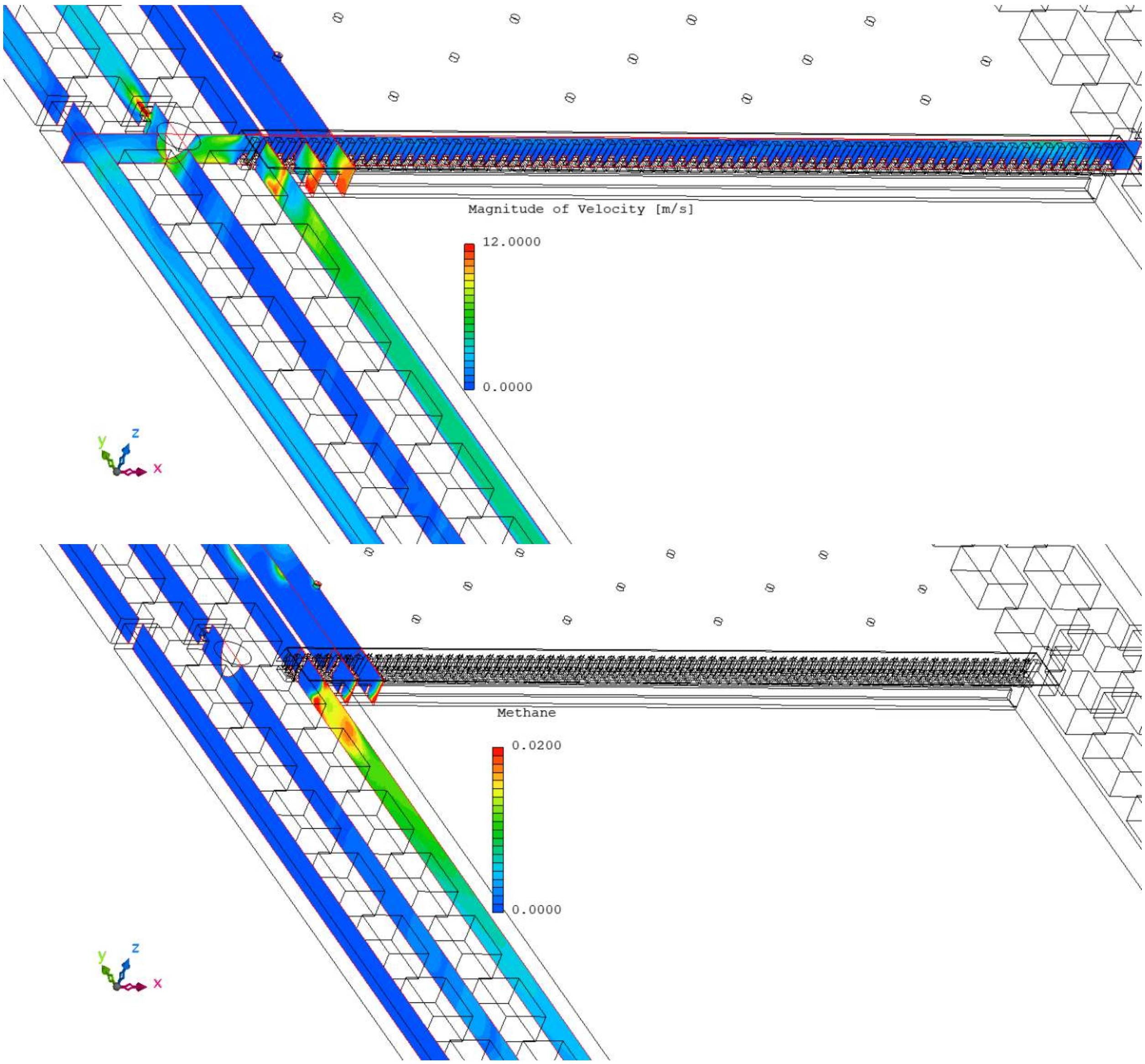

Figure 4-35 Velocity and methane concentrations around tailgate corner for RF3

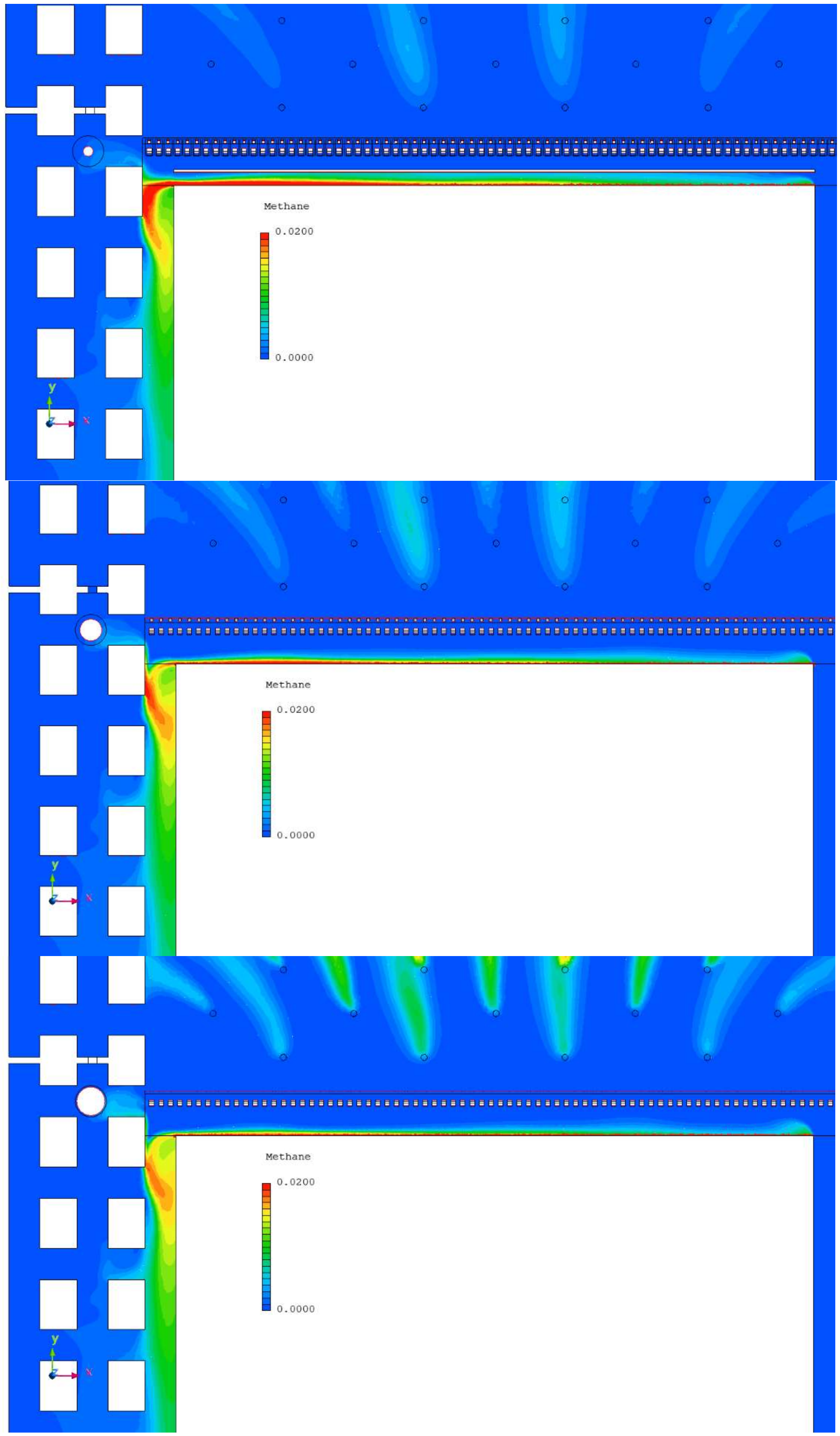

Figure 4-36 Methane concentrations: top 25%, middle 50%, bottom 75% of mining height for RF3

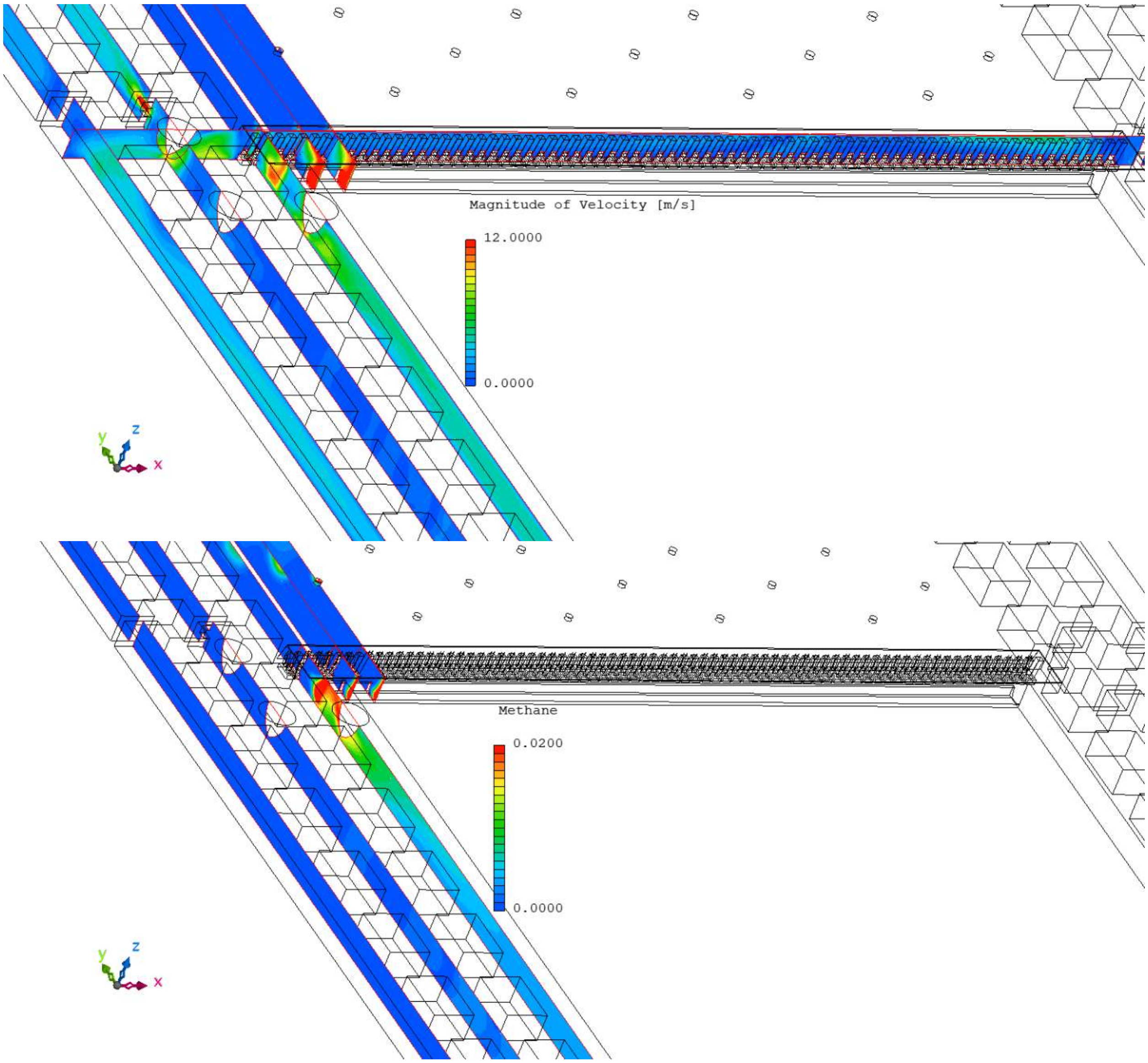

Figure 4-37 Velocity and methane concentrations around tailgate corner for all RF

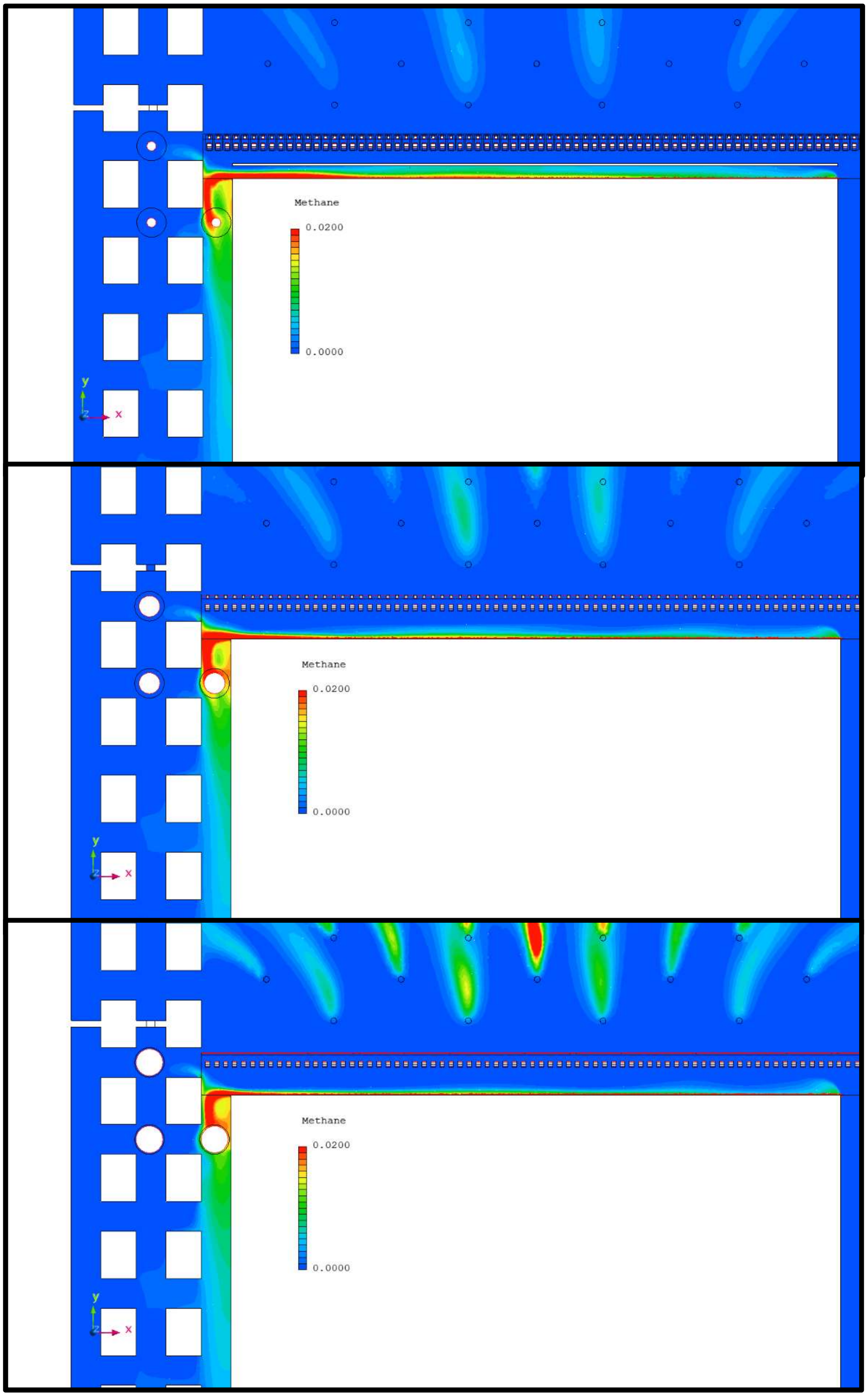

Figure 4-38 Methane concentrations: top 25%, middle 50%, bottom 75% of mining height for all RF

4.2.5.2 With face improvements (Curtains)

One Idea floating around the community is to make improvements to the longwall face which could be permanent or deploy when need to help increase turbulence across the face. This increased turbulence would help dilute methane concentrations by mixing the gasses and using the full airflow potential instead of only the air near the methane sources. The following section shows how the same roof fall scenarios would differ if two moderately sized 'mixing' curtains were placed along the face. Baseline figures with the two curtains placed in the walkway of the face are provided first for reference.

In Figure 4-39 airflow can be seen traveling around the curtain and shields at a much greater rate than when no curtains are present in Figure 4-29. The curtains are angled towards the face and increased methane mixing can be seen in Figure 4-40 when compared to Figure 4-30. Also, no methane recirculation or methane build up can be seen in Figure 4-40, which implies that there is air no recirculation around the curtains. There is what appears to be recirculation about three cross cuts outby the tailgate resister however this is just airflow distributing from the third entryway.

Once the first roof fall location was added to the model this recirculation pattern becomes very evident in Figure 4-42; but the concentration of methane is still well under 1%. What is most auspicious is the decrease of methane build up before and after the roof fall. In Figure 4-42 the third entry quickly changes from light green to light blue around the roof fall indicating that there is through mixing of the airflow in the entryway. Unlike the original roof fall simulation, which showed a light green color throughout the entryway indicating a methane concentration around 1%, the roof fall with curtains added to the face decreased methane concentrations in the third entryway to well under 1%. No other entryway indicated a significant increase in the methane concentration which leads to the conclusion that the methane is more evenly distributed within the third entryway itself.

Similarly, in the second roof fall location a significant decrease in methane concentrations around the tailgate corner can be seen in Figure 4-44 when compared to Figure 4-34. Given the same boundary conditions were used for both simulations adding the curtains clearly decreased the methane concentration in the 'main flow' of air traveling around the tailgate corner. This leads to significant decreases in methane concentration in the third entryway and leads to the methane quickly dispersing though the other two entryways.

With the roof fall moved to the first cross cut outby the tailgate resister a similar pattern of decreased methane concentration around the tailgate corner of the face can be seen in Figure 4-46. Airflow can clearly be seen moving freely from the third entry to the middle entry and even a small amount of methane has dispersed to the first entry. This amount of mixing along the tailgate is not prevalent at all in the roof fall simulation without the curtains as seen in Figure 4-36. In all three roof fall locations placing two curtains along the face increased air mixing along the face which allowed for a more even distribution of methane around the tailgate corner and entryways.

Finally, when all three roof fall location are simulated together the curtains clearly perform better than the simulations without them. Figure 4-48 shows the methane concentrations around the tailgate corner with minimal red which indicated a methane concentration over 2%. If the curtains are not in place like that of Figure 4-38 clear sections of red are present with recirculation patterns prevalent before the roof falls.

Throughout all eight of these roof fall simulations, four with and four without curtains it is clear that adding some amount of a ‘mixing curtain’ will be beneficial for the adequate mixing of methane gases that come off the mining face.

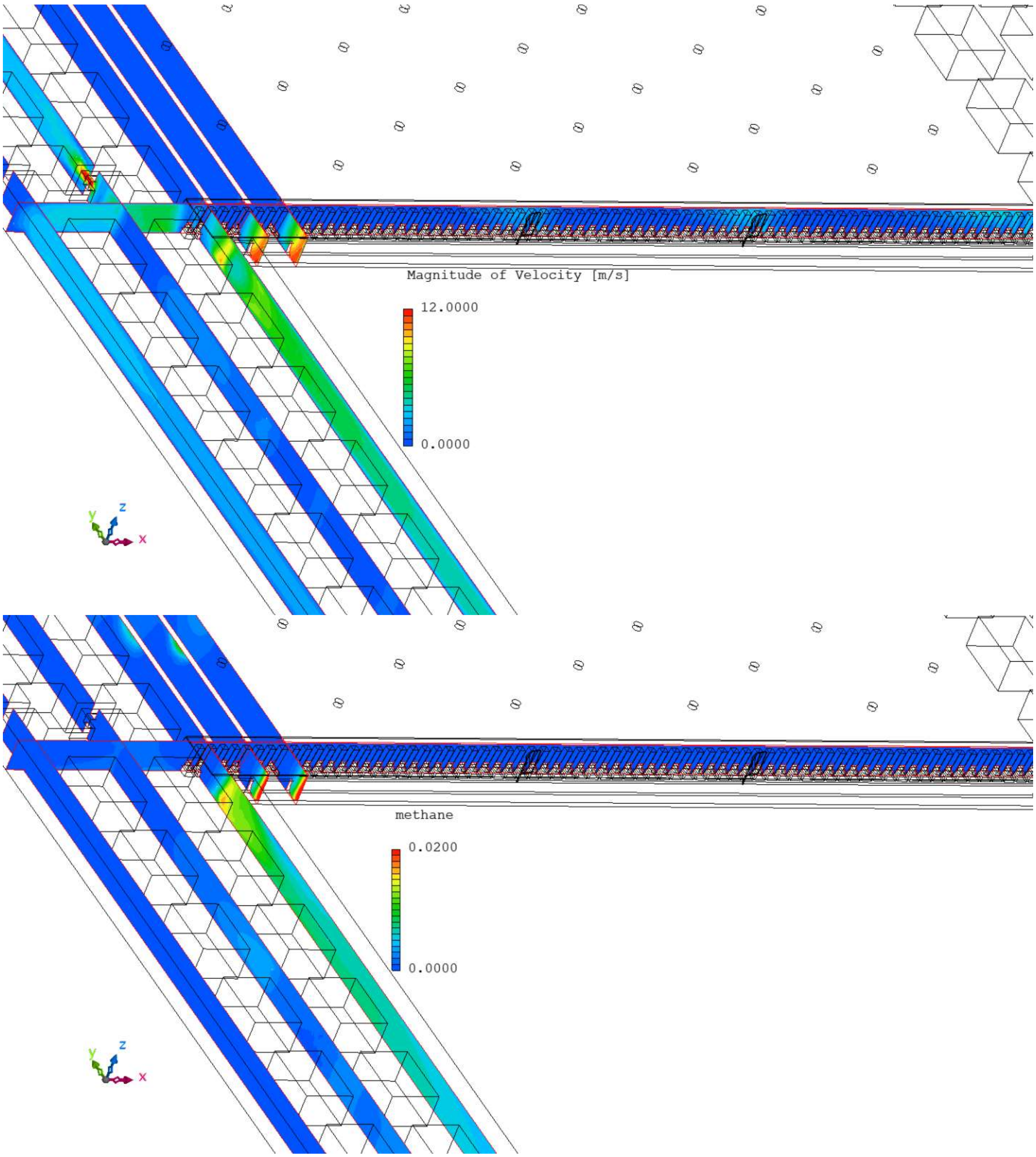

Figure 4-39 Baseline velocity and methane concentrations around tailgate corner with curtain

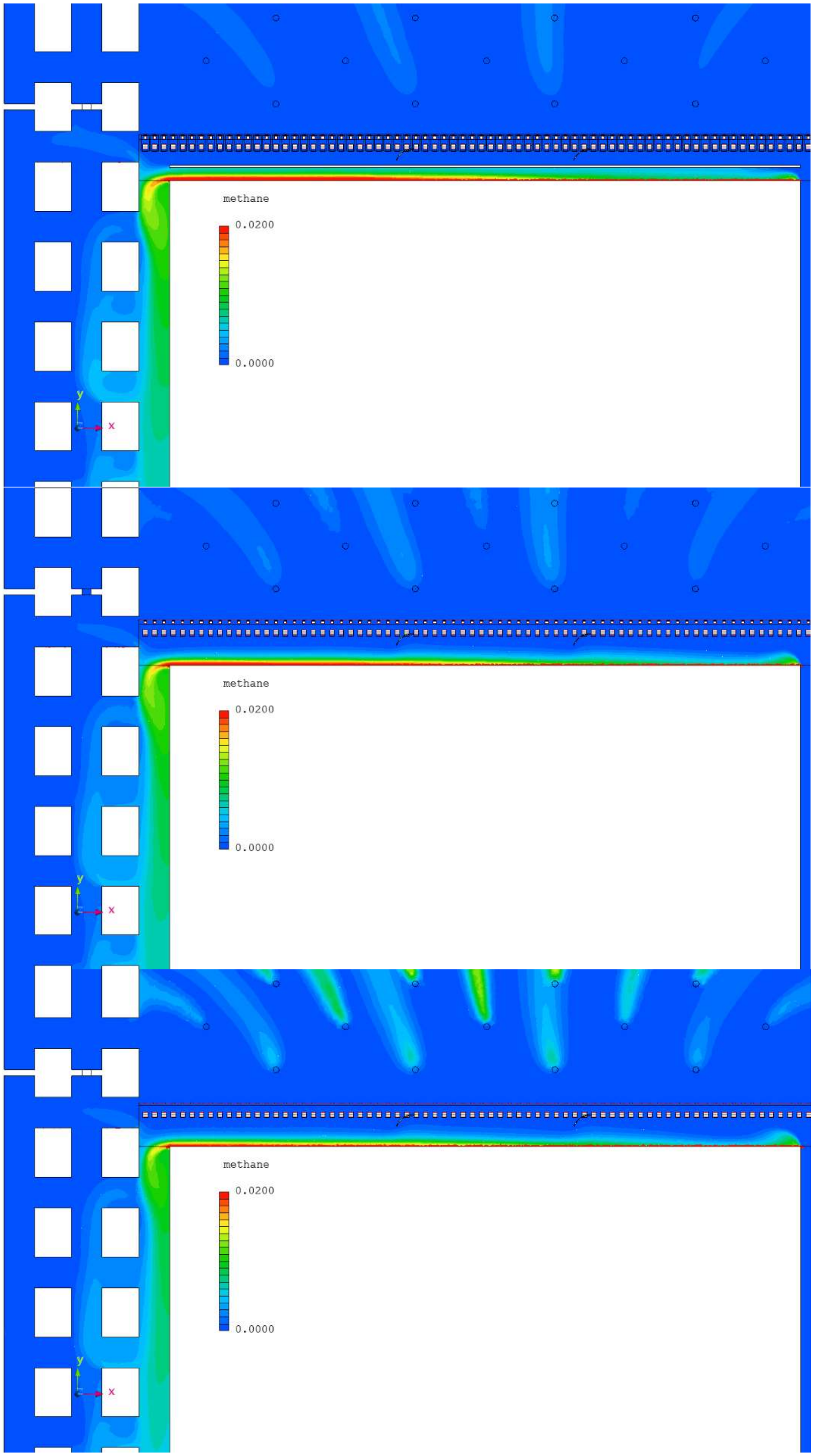

Figure 4-40 Baseline methane concentrations with curtain: top 25%, middle 50%, bottom 75% of mining height

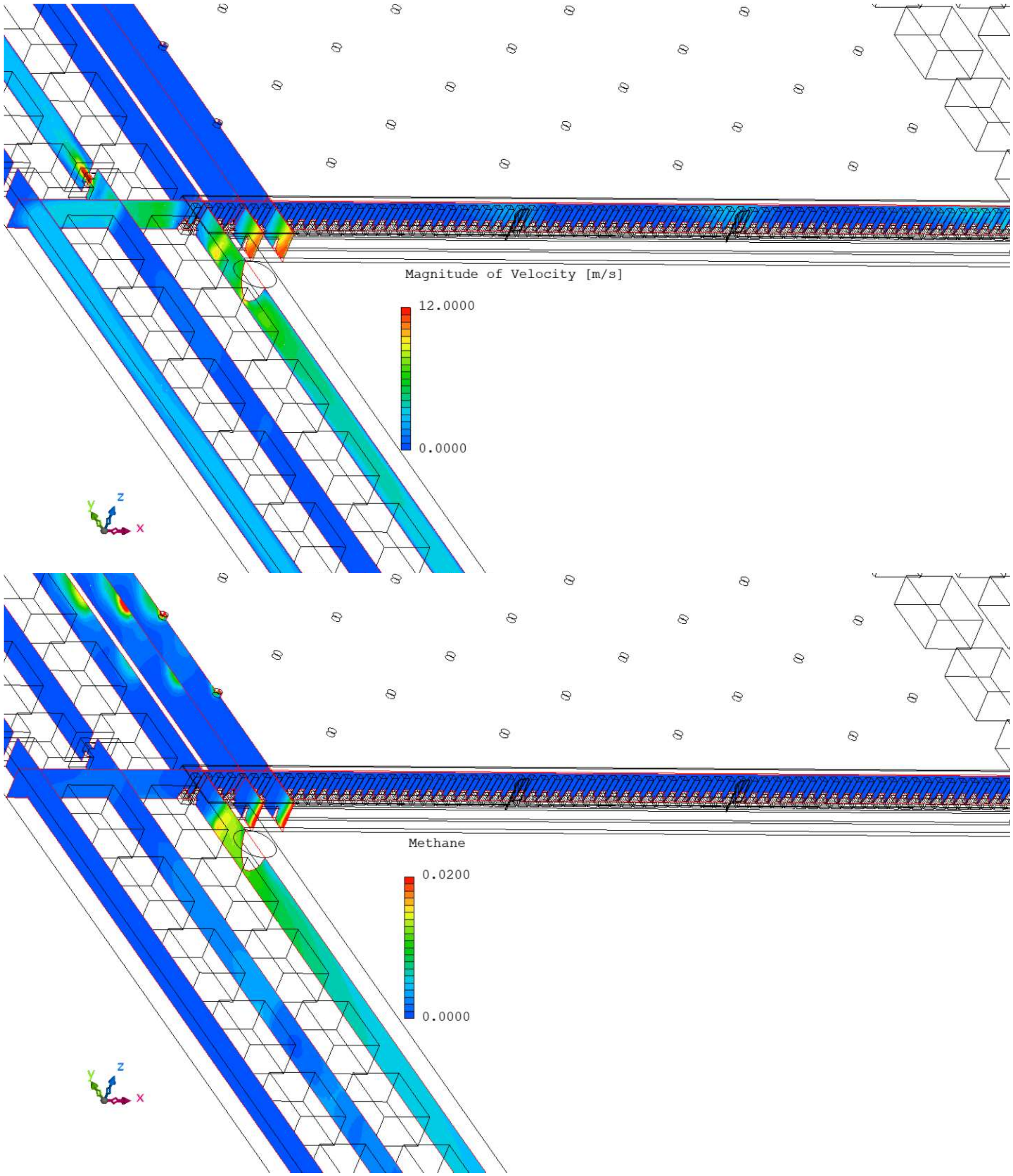

Figure 4-41 Velocity and methane concentrations around tailgate corner for RF1 with curtain

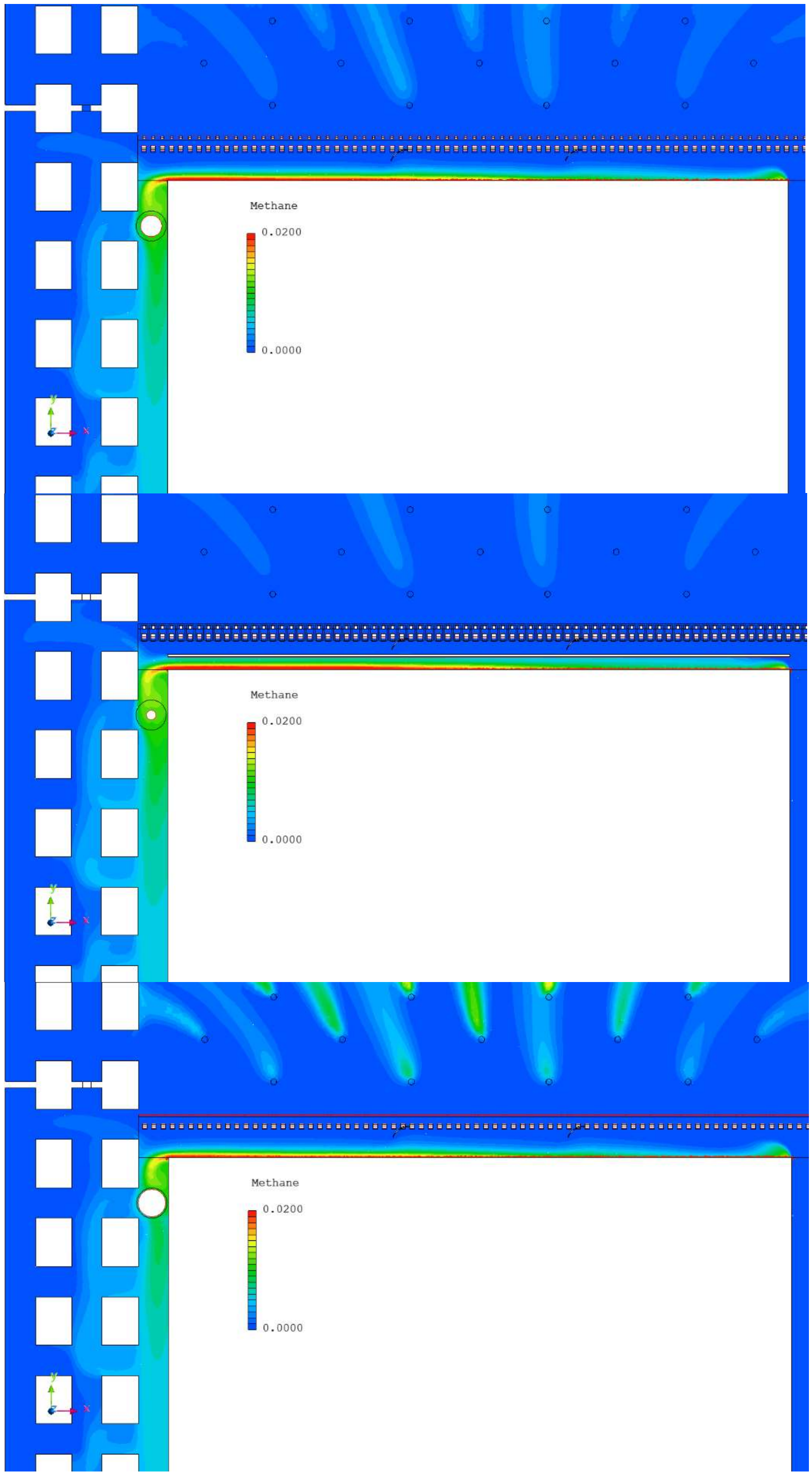

Figure 4-42 Methane concentrations: top 25%, middle 50%, bottom 75% of mining height for RF1 with curtain

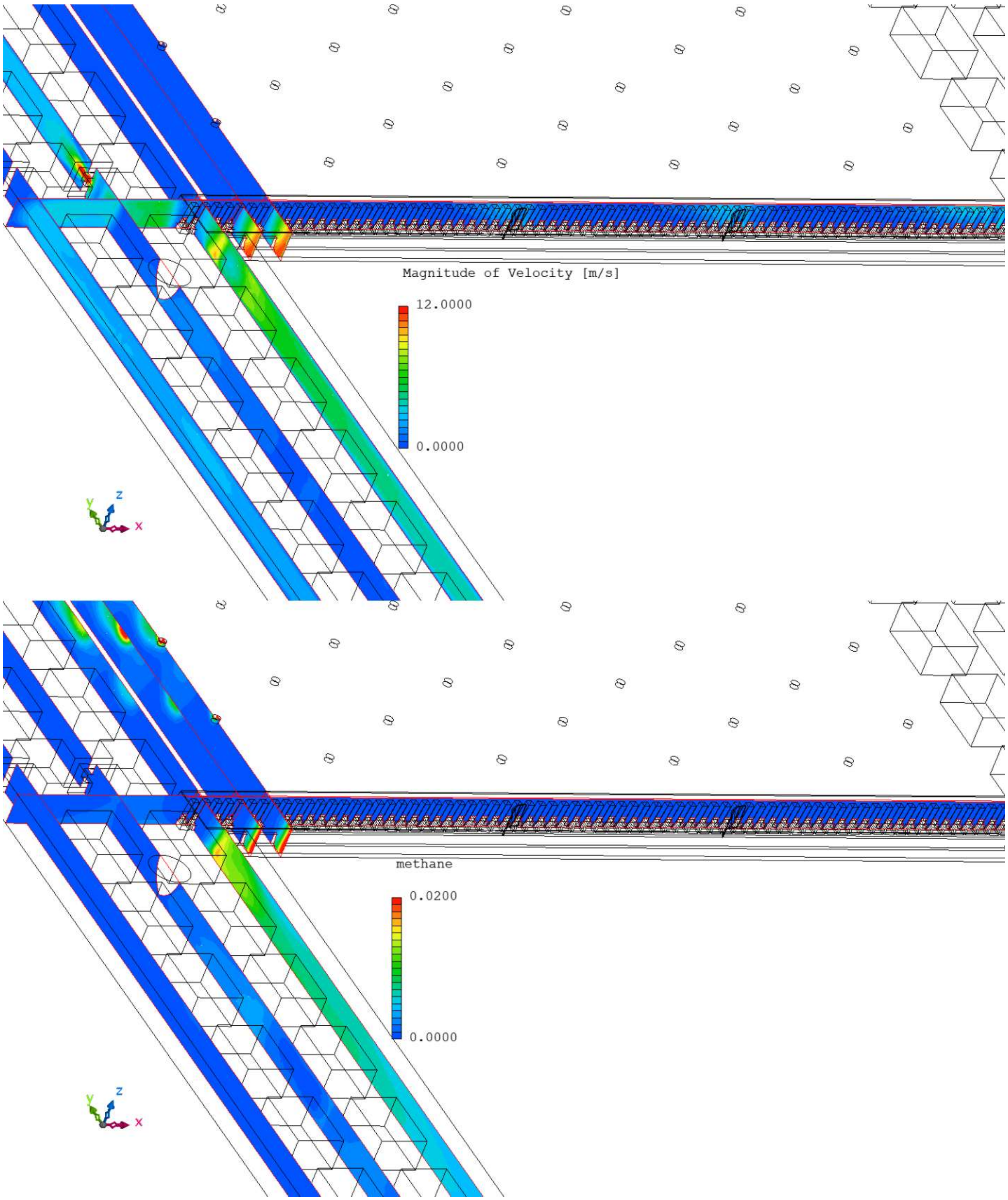

Figure 4-43 Velocity and methane concentrations around tailgate corner for RF2 with curtain

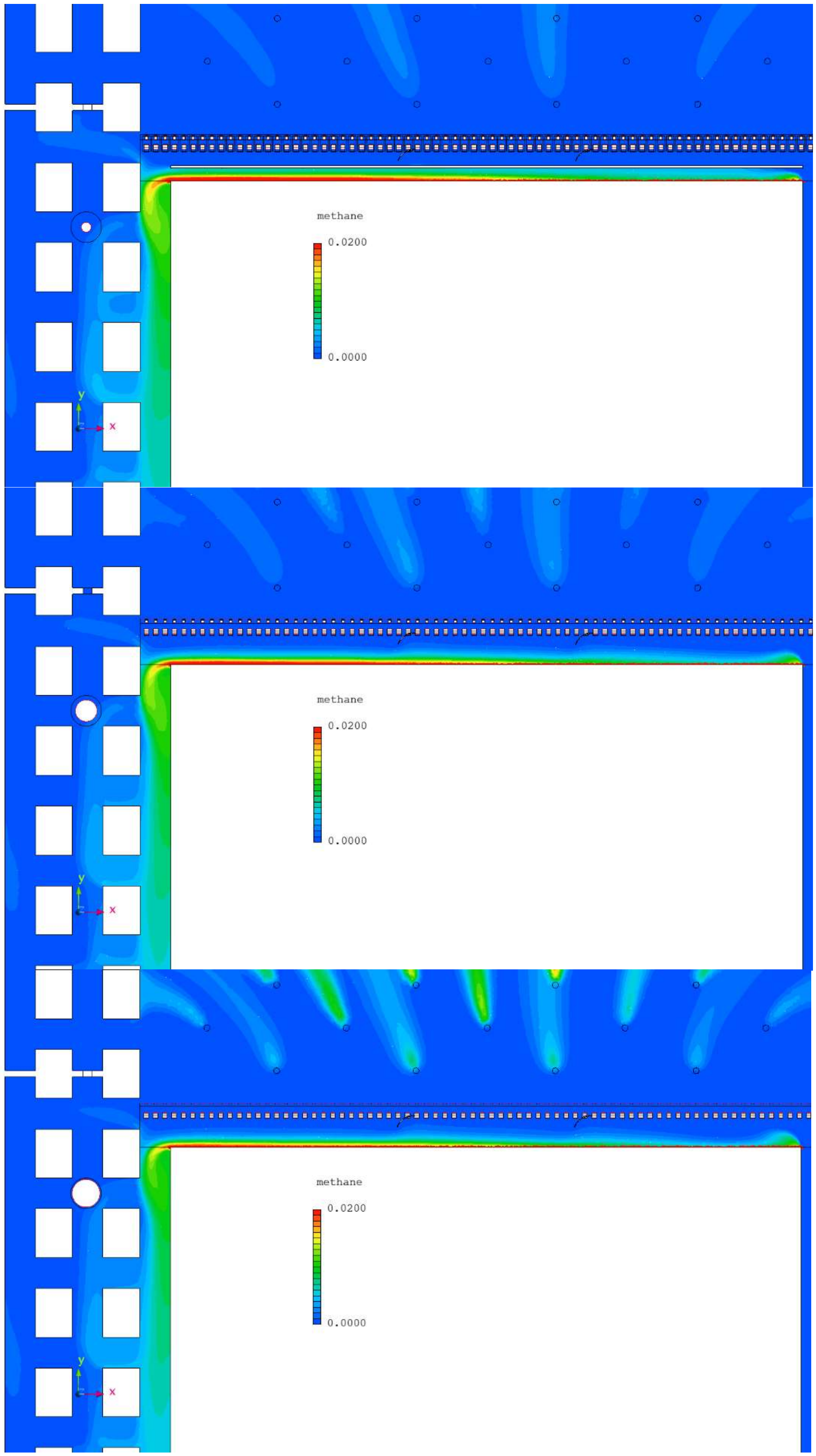

Figure 4-44 Methane concentrations: top 25%, middle 50%, bottom 75% of mining height for RF2 with curtain

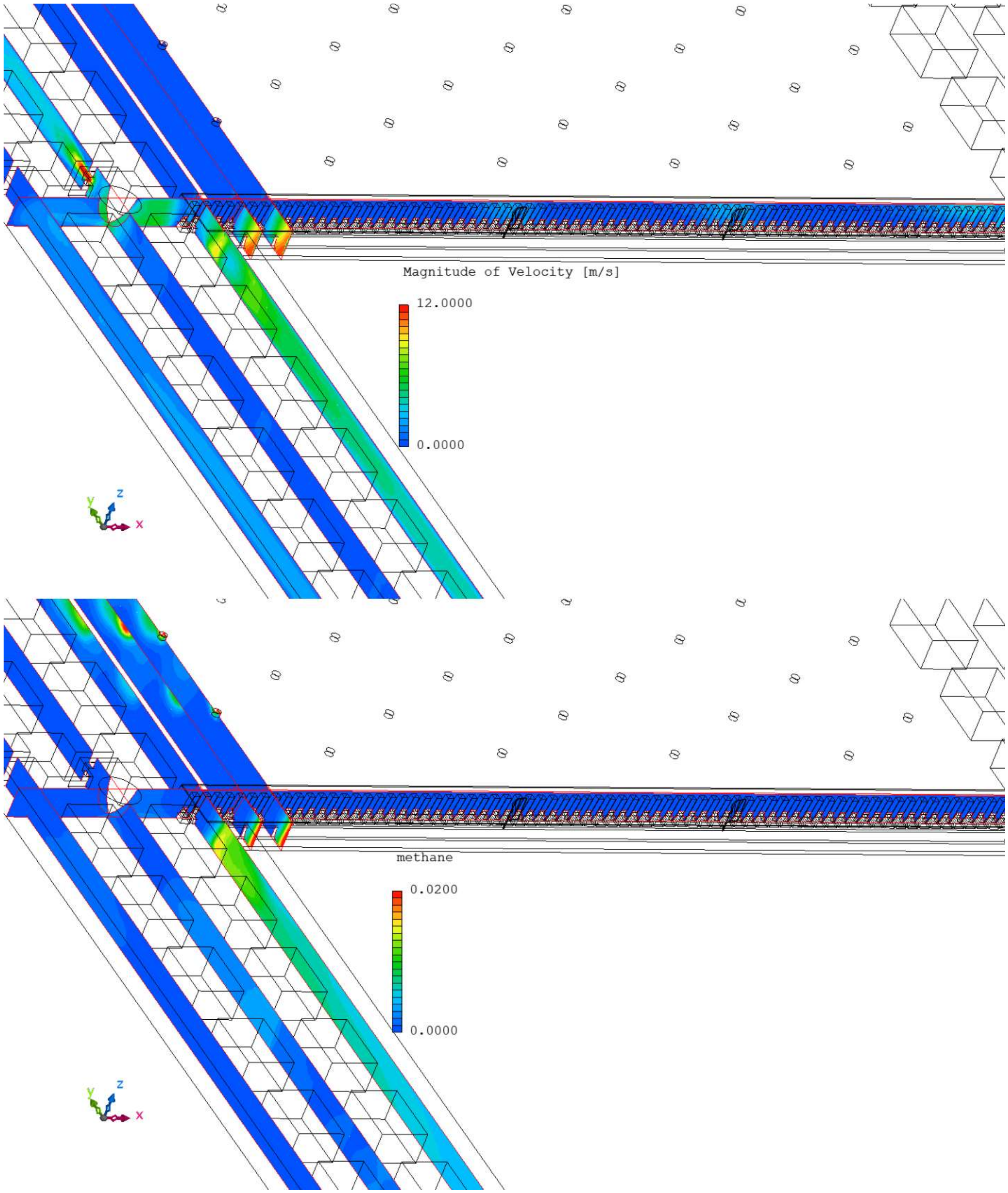

Figure 4-45 Velocity and methane concentrations around tailgate corner for RF3 with curtain

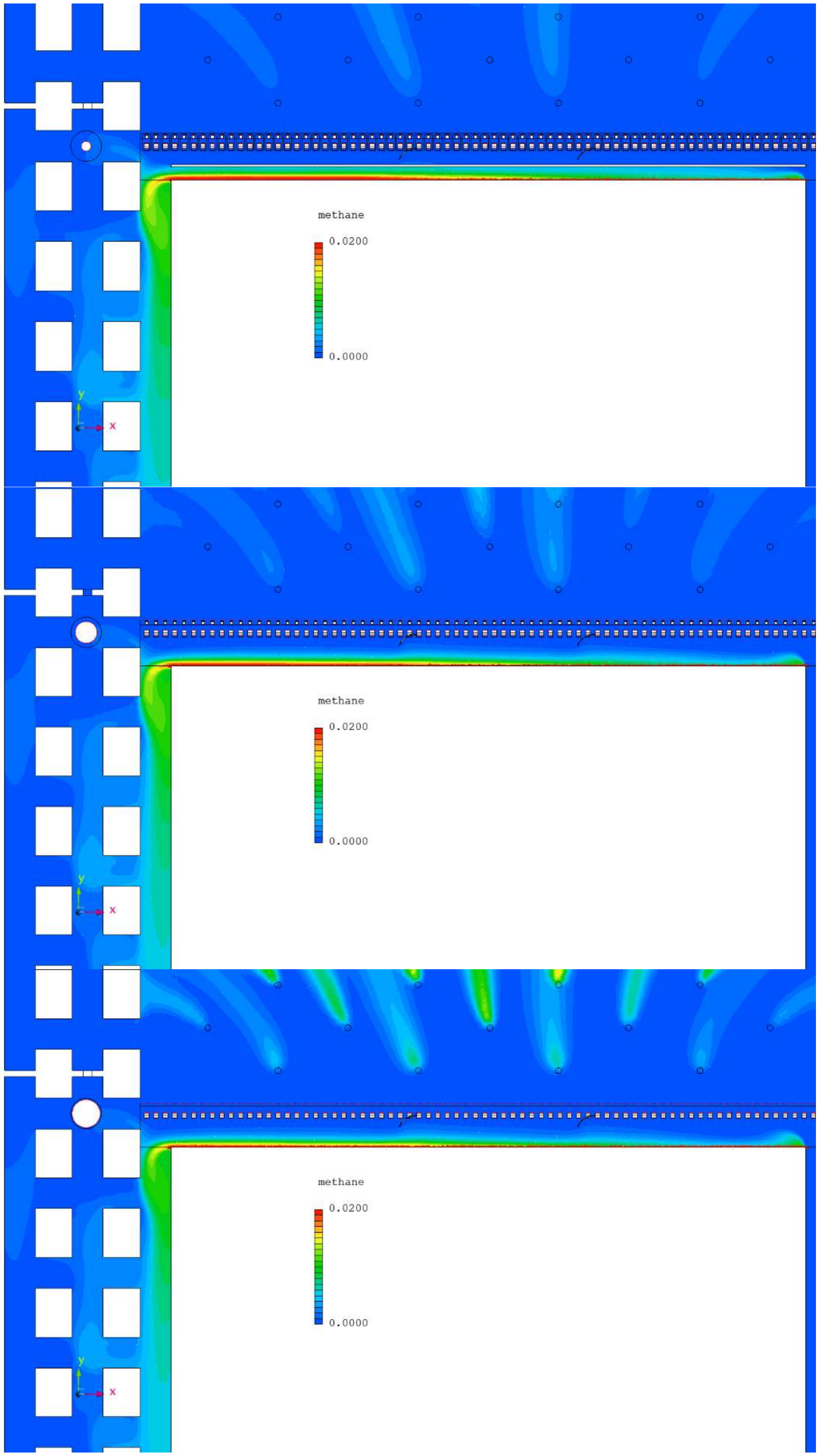

Figure 4-46 Methane concentrations: top 25%, middle 50%, bottom 75% of mining height for RF3 with curtain

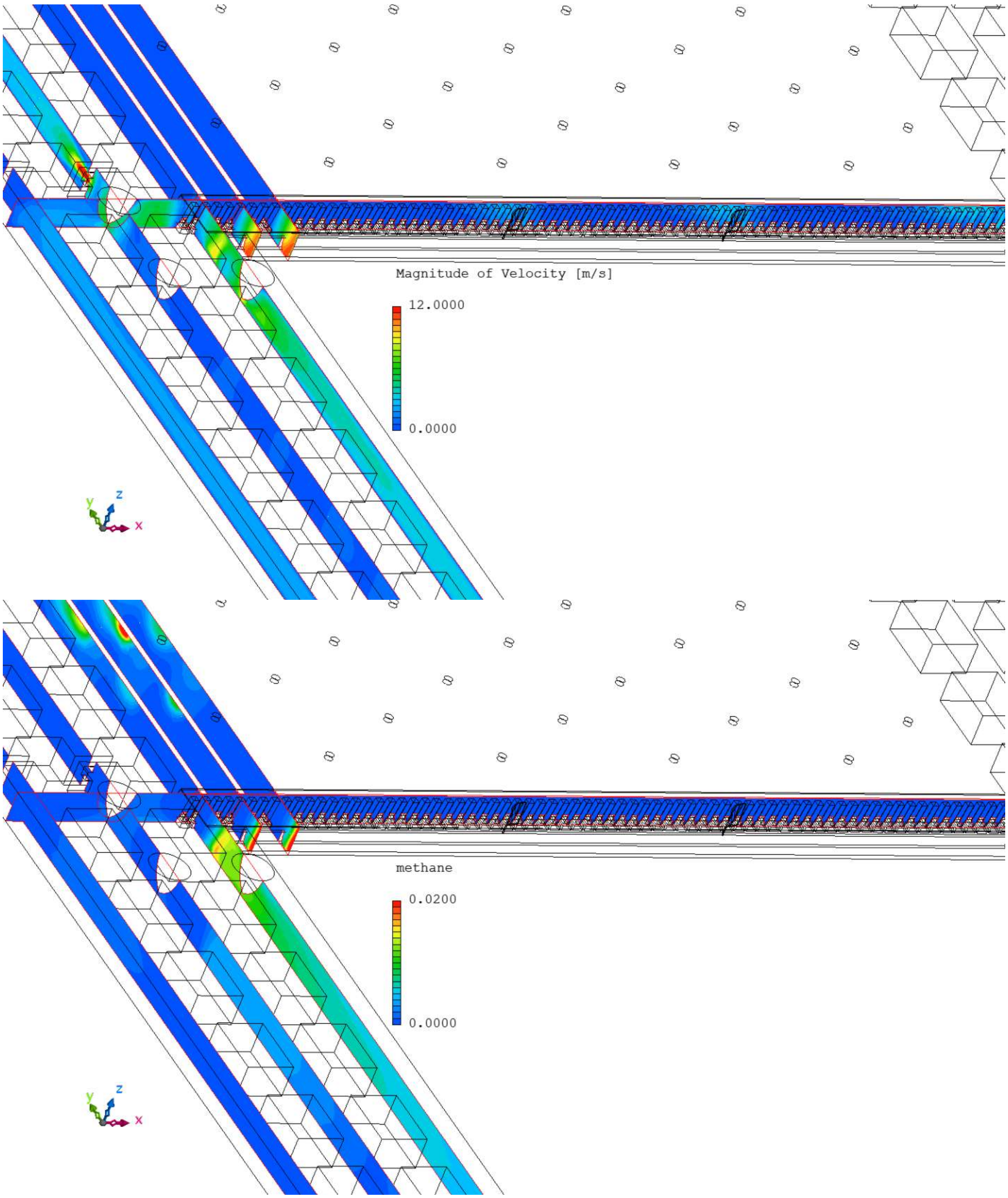

Figure 4-47 Velocity and methane concentrations around tailgate corner for all RF with curtain

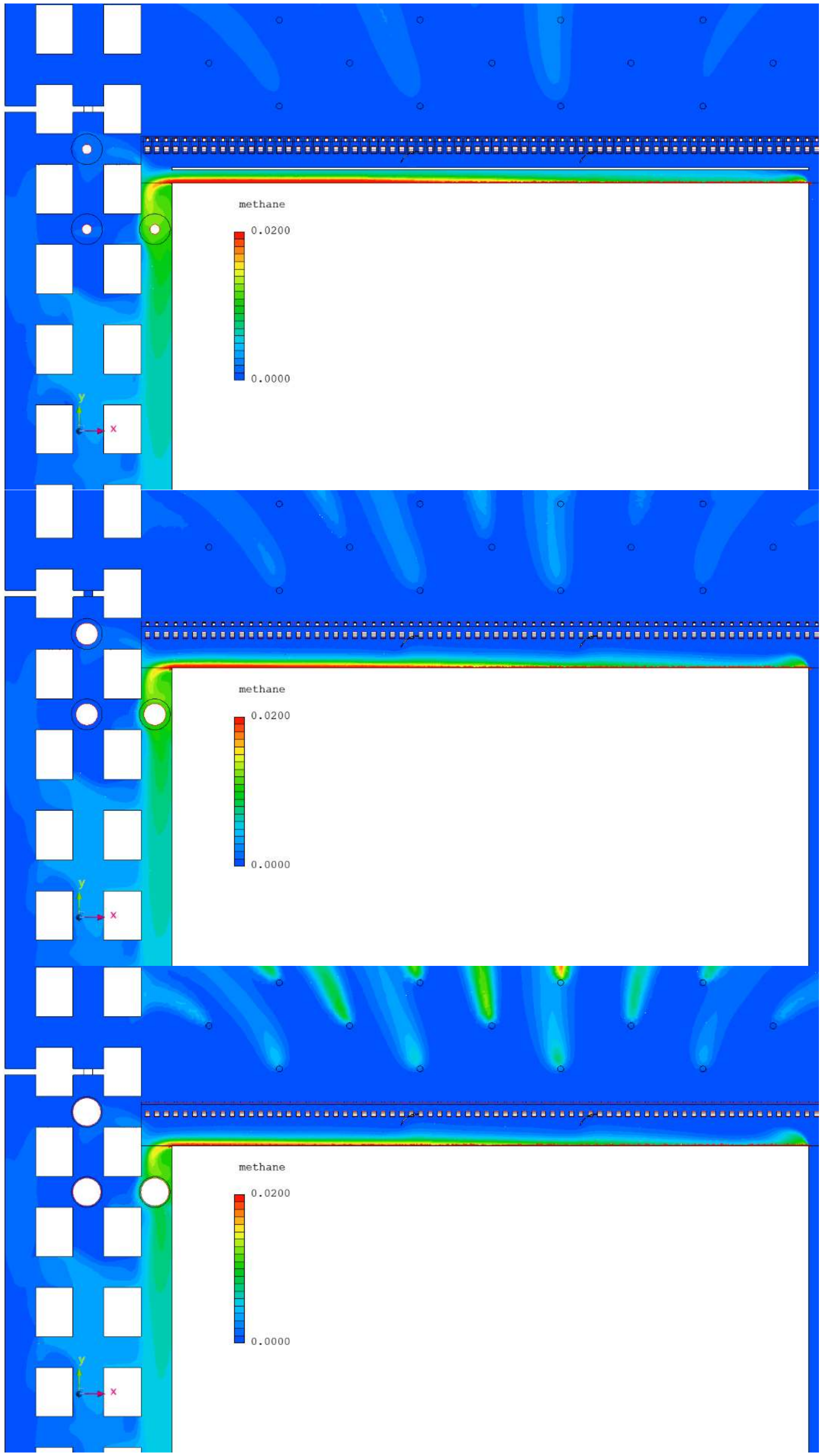

Figure 4-48 Methane concentrations: top 25%, middle 50%, bottom 75% of mining height for all RF with curtain

Chapter 5

Conclusion

Coal remains one of the most important energy resources in the US. It is unfortunate that methane gas hazards are still a top concern for a safe underground mine operation. Based on the statistics of the MSHA mine violation database, it was shown that over 550 methane related violations were reported after year of 2000. These repetitive methane related citations urge the coal mining community to improve the understanding of how methane gas is distributed in the ventilation and bleeder systems. The goal of this study was to define the gas emission behavior and its interaction with the active ventilation system. This was done through experimental and numerical CFD modeling of a scaled longwall system.

Once a CFD model was created and validated by the PSU physical scaled model, the first set of simulations using CFD was conducted to investigate the ventilation system while specifically looking at the ventilation effectiveness around the face. By varying ventilation parameters such headgate and tailgate resistances and bleeder fan pressure, 72 different ventilation schemes were created and subsequently investigated for their effectiveness. Then a series of face advancement simulations were conducted with the goal of determining how the face airflow interacts with the varying geometry of an advancing face. Lastly, a multitude of CFD simulations was conducted with roof falls around the tailgate entries. This provided a more comprehensive picture at how the ventilation system reacts to ventilation interruption incidents.

Based on this study, the following main conclusions can be made:

1) The PSU physical scaled model ventilation parameters (pressure and velocity) was fully developed and the longwall ventilation system includes a bleeder system.
2) A CFD model was created and verified to predict the airflows measured around the PSU physical scaled model. The CFD modeled results well agreed with the experimental

measured data and it is demonstrated it can be used to improve our understanding of interactions of the ventilation and bleeder system.

3) Ventilation controls, such as bleeder fan pressure and headgate and tailgate resistance, predictably affect the airflow distribution and ventilation effectiveness.

4) As the face advances, the ventilation effectiveness remains relativity unchanged while the effective use of this ventilation air decreases. This was shown by the increased methane concentrations in the tailgate.

5) Resistance increase due to roof incidents around the tailgate significantly alters the ventilation effectiveness and may induce hazardous condition. However, with the addition of mixing curtains placed along the face, the ventilation airflow can achieve a better methane dilution because fully developed turbulent flow.

These results were demonstrated in the CFD simulations based on the geometry of PSU physical scaled mine model. It should be noticed that the CFD model cannot be directly applied to real mine condition, but they can be scaled according to the scaling relationships to field conditions.

References

AZIZ, N., BALUSU, B., & BAAFI, E. (1993). Application of Computational Fluid Dynamics Codes to Develop Effective Gas/Dust Control Measures in Underground Coal Mines. *The Australian Coal Journal*, (42), 19–27.

Bakke, P., & Leach, S. (1962). Principles of formation and dispersion of methane roof layers and some remedial measures. *The Mine Engineering*, *121*(22), 645–658.

Brnich, M. J., & Kowalski-Trakofker, K. M. (2010). Underground Coal Mine Disasters 1900 - 2010: Events, Responses, and a Look to the Future. *Extracting the Science: A Century of Mining Research*, 363–372. Retrieved from http://cdc.gov/niosh/mining/pubs/pdfs/ucmdn.pdf

Brune, B. J. F., & Goertz, B. (2013). Lessons Learned from Mine Disasters : New Technologies and Guidelines to Prevent Mine Disasters and Improve Safety, (1), 1–101.

Brune, J., Amen, J., & Kotch, M. (1999). Developments in Longwall Ventilation. In *8TH US MINE VENTILATION SYMPOSIUM* (pp. 7–11).

C.M. Boyer, J.R. Kelafant, V.A. Kuuskraa, K. C. M. (1990). *Methane Emissions From Coal Mining*. ICF Resources Incorporated.

Cai, P., Nie, W., Hua, Y., Wei, W., & Jin, H. (2018). Diffusion and pollution of multi-source dusts in a fully mechanized coal face. *Process Safety and Environmental Protection*, *118*, 93–105. https://doi.org/10.1016/j.psep.2018.06.011

Chang, P., Xu, G., Zhou, F., Mullins, B., Abishek, S., & Chalmers, D. (2019). Minimizing DPM pollution in an underground mine by optimizing auxiliary ventilation systems using CFD. *Tunnelling and Underground Space Technology*, *87*(January), 112–121. https://doi.org/10.1016/j.tust.2019.02.014

Chen, Q. (1995). Comparison of different k-ε models for indoor air flow computations. *Numerical Heat Transfer, Part B: Fundamentals*, *28*(3), 353–369. https://doi.org/10.1080/10407799508928838

Coal Mining Disasters: 1939 to Present. (n.d.). Retrieved November 10, 2018, from https://www.cdc.gov/niosh/mining/statistics/content/coaldisasters.html

Code of Federal Regulations. (2014). Mineral Resources, 467. Retrieved from https://www.gpo.gov/fdsys/pkg/CFR-2014-title30-vol1/pdf/CFR-2014-title30-vol1.pdf

Esterhuizen, G. S. (2017). a Methodology for Determining Gob Permeability Distributions and Its a Methodology for Determining Gob Permeability Distributions and Its Application To Reservoir. In *2007 SME Annual Meeting and Exhibit*.

Karacan, C. Ö., Ruiz, F. A., Cotè, M., & Phipps, S. (2011). Coal mine methane: A review of capture and utilization practices with benefits to mining safety and to greenhouse gas reduction. *International Journal of Coal Geology*, *86*(2–3), 121–156. https://doi.org/10.1016/j.coal.2011.02.009

Kurnia, J. C., Sasmito, A. P., & Mujumdar, A. S. (2014). CFD simulation of methane dispersion and innovative methane management in underground mining faces. *Applied Mathematical Modelling*, *38*(14), 3467–3484. https://doi.org/10.1016/j.apm.2013.11.067

Launder, B. E., & Spalding, D. B. (1974). THE NUMERICAL COMPUTATION OF TURBULENT FLOWS. *Computer Methods in Applied Mechanics and Engineering*, *3*, 269–289. https://doi.org/10.1016/0045-7825(74)90029-2

McAteer, J. Davitt. Beall, K., & Beck, James A. McGinley, Patrick C. Monforton, Celeste. Roberts, Deborah. Spence, Beth Weise, S. (2011). Report to the Governor Governor's Independent Investigation Panel. *Office*.

Mishra, D. P., Kumar, P., & Panigrahi, D. C. (2016). Dispersion of methane in tailgate of a

retreating longwall mine: a computational fluid dynamics study. *Environmental Earth Sciences*, *75*(6). https://doi.org/10.1007/s12665-016-5319-9
Ren, T., & Balusu, R. (2005). CFD Modelling of Goaf Gas Migration to Improve the Control of Spontaneous Combustion in Longwalls CFD Modelling of Goaf Gas Migration to Improve the Control of Spontaneous Combustion in Longwalls, 259–264.
Sasmito, A. P., Birgersson, E., Ly, H. C., & Mujumdar, A. S. (2013). Some approaches to improve ventilation system in underground coal mines environment - A computational fluid dynamic study. *Tunnelling and Underground Space Technology*, *34*, 82–95. https://doi.org/10.1016/j.tust.2012.09.006
Schatzel, S. J., Krog, R. B., & Dougherty, H. (2011). a Field Study of Us Longwall Coal Mine Ventilation and Bleeder Performance. *Safety And Health*, 1–6.
Tanguturi, K., & Balusu, R. (2014). CFD Modeling of Methane Gas Distribution and Control Strategies in a Gassy Coal Mine. *The Journal of Computational Multiphase Flows*, *6*(1), 65–77. https://doi.org/10.1260/1757-482x.6.1.65
Tanguturi, K., Balusu, R., & Bongani, D. (2017). GOAF GAS FLOW MODELLING IN 6KM LONG LONGWALL PANEL, *31*, 1–15.
Toraño, J., Torno, S., Menendez, M., Gent, M., & Velasco, J. (2009). Models of methane behaviour in auxiliary ventilation of underground coal mining. *International Journal of Coal Geology*, *80*(1), 35–43. https://doi.org/10.1016/j.coal.2009.07.008
Wala, a. M., Vytla, S., Taylor, C. D., & Huang, G. (2007). Mine Face Ventilation: A Comparison of CFD Results against Benchmark Experiments for the CFD Code Validation. *Mining Engineering*, *59*(10), 49–55.
Wang, Z., Ren, T., & Cheng, Y. (2017a). Numerical investigations of methane flow characteristics on a longwall face Part I: Methane emission and base model results. *Journal of Natural Gas Science and Engineering*, *43*, 242–253. https://doi.org/10.1016/j.jngse.2017.03.029
Wang, Z., Ren, T., & Cheng, Y. (2017b). Numerical investigations of methane flow characteristics on a longwall face Part II: Parametric studies. *Journal of Natural Gas Science and Engineering*, *43*, 254–267. https://doi.org/10.1016/j.jngse.2017.03.038
Wang, Z., Ren, T., Ma, L., & Zhang, J. (2018). Investigations of ventilation airflow characteristics on a longwall face—a computational approach. *Energies*, *11*(6), 1–25. https://doi.org/10.3390/en11061564
Xu, G., Jong, E. C., Luxbacher, K. D., Ragab, S. A., & Karmis, M. E. (2015). Remote characterization of ventilation systems using tracer gas and CFD in an underground mine. *Safety Science*, *74*, 140–149. https://doi.org/10.1016/j.ssci.2015.01.004
Yuan, L., Smith, A., & Brune, J. (2006). Computational fluid dynamics study on the ventilation flow paths inlongwall gobs. *11th US/North American Mine Ventilation Symposium 2006*, 591–598. https://doi.org/10.1201/9781439833391.ch83
Yuan, L., & Smith, A. C. (2008). Numerical study on effects of coal properties on spontaneous heating in longwall gob areas. *Fuel*, *87*(15–16), 3409–3419. https://doi.org/10.1016/j.fuel.2008.05.015
Yueze, L., Akhtar, S., Sasmito, A. P., & Kurnia, J. C. (2017). Prediction of air flow, methane, and coal dust dispersion in a room and pillar mining face. *International Journal of Mining Science and Technology*, *27*(4), 657–662. https://doi.org/10.1016/j.ijmst.2017.05.019
Zhai, Z. J., Zhang, W., Zhang, Z., & Chen, Q. Y. (2007). Evaluation of various turbulence models in predicting airflow and turbulence in enclosed environments by CFD: part 1 - Summary of prevalent turbulence models. *Hvac&R Research*, *13*(6), 853–870. https://doi.org/10.1080/10789669.2007.10391459
Zhang, Q., Zhou, G., Qian, X., Yuan, M., Sun, Y., & Wang, D. (2018). Diffuse pollution

characteristics of respirable dust in fully-mechanized mining face under various velocities based on CFD investigation. *Journal of Cleaner Production*, *184*, 239–250. https://doi.org/10.1016/j.jclepro.2018.02.230

Zheng, Y., Li, Y., Thiruvengadam, M., Lan, H., & Tien, J. C. (2017). DPM dispersion inside a single straight entry using dynamic mesh model. *International Journal of Coal Science and Technology*, *4*(3), 234–244. https://doi.org/10.1007/s40789-017-0179-9

Zheng, Y., Thiruvengadam, M., Lan, H., & Tien C., J. (2015). Simulation of DPM distribution in a long single entry with buoyancy effect. *International Journal of Mining Science and Technology*, *25*(1), 47–52. https://doi.org/10.1016/j.ijmst.2014.11.004

Appendix

CFD Equations and RNG k-ε equations

CFD Equations

$$\frac{\partial \rho}{\partial t} + \frac{\partial}{\partial x_i}\rho u_i = 0$$

Equation 1: Mass Conservation equation for Compressible Fluids

$$\frac{\partial \rho u_i}{\partial t} + \frac{\partial u_j \rho u_i}{\partial x_j} = \frac{\partial \sigma_{ij}}{\partial x_j} + \rho g_i \quad \text{(i=1-3)}$$

Equation 2: Momentum Conservation equation for Compressible Fluids

$$\frac{\partial \rho H}{\partial t} + \frac{\partial u_j \rho H}{\partial x_j} = \frac{\partial p}{\partial t} + \frac{\partial u_j p}{\partial x_j} + \sigma_{ij}\frac{\partial u_i}{\partial x_j} + \frac{\partial}{\partial x_j} K \frac{\partial T}{\partial x_j} + \dot{q}$$

Equation 3: Energy Conservation equation for Compressible Fluids

$$\frac{\partial \rho C}{\partial t} + \frac{\partial u_j \rho C}{\partial x_j} = \frac{\partial}{\partial x_j}\rho D_m \frac{\partial C}{\partial x_j} + \rho d$$

Equation 4: Diffusive Species concentration equation for compressible fluids

$$p = \rho R T$$

Equation 5: Gas State equation for compressible fluids

$$\sigma_{ij} = \mu\left(\frac{\partial u_i}{\partial x_j} + \frac{\partial u_j}{\partial x_i}\right) - \left(p + \frac{2}{3}\mu\frac{\partial u_k}{\partial x_k}\right)\delta_{ij}$$

Equation 6: Stress Tensor

Variable	Description	Variable	Description
x_i	Coordinates (m)	T_0	Reference Temperature of Fluid (K)
u_i	Velocity of flow in x_i direction (m/s)	C_p	Specific heat at constant pressure ($\frac{j}{kg*K}$)
t	Time (s)	K	Thermal conductivity ($\frac{W}{m*K}$)
ρ	Density of Fluid ($\frac{kg}{m^3}$)	$\dot{q}$	Heat Source ($\frac{\mathrm{W}}{m^3}$)
p	Pressure of Fluid (Pa)	k	Turbulent energy ($\frac{m^2}{s^2}$)
μ	Viscosity (Pa*s) (molecular + eddy)	ε	Turbulent dissipation rate ($\frac{m^2}{s^3}$)
H	Specific enthalpy ($\frac{j}{kg}$)	C	Concentration of diffusive Species (-)
g_i	Gravity ($\frac{m}{s^2}$)	D_m	Diffusion Coefficient ($\frac{m^2}{s}$)
β	Coefficient of volume expansion (K^{-1})	$\dot{d}$	Source terms of diffusive species (s^{-1})
T	Temperature of Fluid (K)	R	Gas constant ($\frac{j}{kg*K}$)

RNG k-ε equations

$$\frac{\partial \rho k}{\partial t}+\frac{\partial u_i \rho k}{\partial x_i}=\frac{\partial}{\partial x_i}\left(\frac{\mu_t}{\sigma_k}\frac{\partial k}{\partial x_i}\right)+\rho(G_s+G_{s1}+G_{s2}+G_{s3}-\varepsilon)$$

Equation 7: Turbulent Energy equation for Compressible Fluids (k- ε)

$$\frac{\partial \rho \varepsilon}{\partial t}+\frac{\partial u_i \partial \varepsilon}{\partial x_i}=\frac{\partial}{\partial x_i}\left(\frac{\mu_t}{\sigma_\varepsilon}\frac{\partial \varepsilon}{\partial x_i}\right)+C_1\frac{\varepsilon}{k}(G_s+G_{s1}+G_{s2}+G_{s3}-\varepsilon)-C_2\frac{\rho \varepsilon^2}{k}$$

Equation 8: Turbulent Dissipation rate equation for Compressible Fluids (k- ε)

Where

$$G_S=\mu_t\left(\frac{\partial u_i}{\partial x_j}+\frac{\partial u_j}{\partial x_i}\right)\frac{\partial u_i}{\partial x_j}$$

$$G_{S1}=\frac{2}{3}\rho k D$$

$$G_{S2}=\frac{2}{3}\rho \mu_t D^2$$

$$G_{S3}=\frac{\mu_t}{\sigma_t \rho^2}\frac{\partial \rho}{\partial x_i}\frac{\partial p}{\partial x_i}$$

$$D=\frac{\partial u_i}{\partial x_i}$$

$$\mu_t=C_\mu \rho \frac{k^2}{\varepsilon}$$

Equation 9: eddy Viscosity μ_t

Constants:

σ_k	σ_ε	C_1	C_2	C_μ
0.719	0.719	C_1	1.68	0.085

Table 1: Constants for RNG k- ε equations

Where

$$C_1 = 1.42\ \frac{\eta\left(\frac{1-\eta}{4.38}\right)}{1+0.012\eta^3}$$

$$\eta = \frac{k}{\varepsilon}\left\{\frac{1}{2}\left(\frac{\partial u_i}{\partial x_j} + \frac{\partial u_j}{\partial x_i}\right)\left(\frac{\partial u_i}{\partial x_j} + \frac{\partial u_j}{\partial x_i}\right)\right\}^{\frac{1}{2}}$$

For the turbulence equations: the following variables: u_i, T, p, ρ are all time averaged but the ($\bar{}$) symbol has been omitted.